# Flow fields around falling conical graupel and the efficiencies with which these graupel collide with cloud droplets

Alex Kubicek *

*Department of Atmospheric and Oceanic Sciences, University of Wisconsin-Madison, Madison, WI, USA*

* *Corresponding author address:* Alex Kubicek, UW-Madison Dept. of Atmospheric and Oceanic Sciences, 1225 W. Dayton St., Madison, WI 53706.

E-mail: akubicek@wisc.edu

ABSTRACT

The growth of graupel impacts many cloud microphysical and thermal dynamics processes in deeper convective clouds. It is especially important in the development of thunderstorms and their electrification. When hydrometeors are simulated in mesoscale models, graupel is generalized to have the same parameters as hail while they have different structures. The reason why graupel is treated as small hail is due to the small amount that it has been researched theoretically, especially the flow fields around falling graupel and their riming growth. The purpose of this study is to examine the characteristics of flow fields around falling graupel and to use these flow fields to determine the collision efficiencies with which graupel collide with supercooled droplets. The flow fields are obtained by solving the relevant unsteady Navier-Stokes equations for flow past graupel using ANSYS Fluent. Detailed flow characteristics are presented using the velocity, pressure and vorticity distributions. The collision efficiencies are determined by solving the equation of motion of supercooled droplets in the flow fields of the falling graupel and compute the grazing collision trajectories.

# 1. Introduction and Background

The fall attitude of hydrometeors in clouds has significant impact on cloud microphysics. When a hydrometeor is falling in air, it generates a flow field around it. This flow field then impacts on various processes and one notable example is the collision growth rate of hydrometeors. The collision growth rate depends on how other particles (e.g., small cloud droplets, ice particles or aerosol particles) move around the collector hydrometeor that generates a flow field when it falls in air. The flow field can be very complicated if the hydrometeor is nonspherical and fairly large such as raindrops, graupel and hail (Pruppacher and Klett 1997).

The flow field also influences the diffusion growth or evaporation rate of the falling hydrometeor as the flow causes the so-called ventilation effect that changes the vapor density distribution around the hydrometeor from the stationary case and enhances the vapor flux towards or away from the hydrometeor surface (Ji and Wang 1998).

This thesis is about the flow fields generated by falling graupel particles and we are specifically concerned with the conical graupel. Conical shape is one of the three observed graupel types, the other two being hexagonal and lumped, but those serving as the embryos to form hail are essentially of conical shape (Knight and Knight 1973). Some of the lumped graupel also appear to be conical except that their apices are truncated. Among conical graupel, the apex of the cone can vary from acute to blunt and such a difference may result in different flow characteristics. Another factor that may impact the flow characteristics is the fall orientation which may or may not be vertical but can have various inclination angles due to their oscillatory, tumbling and sailing motions (e.g. Pflaum et al. (1978)). Different orientations result in different flow fields and hence possibly different diffusion and collision growth rates.

Previous studies on the motion of conical graupel are largely confined to experimental observations (e.g., Jayaweera and Mason (1965); List and Schemenauer (1971); Pflaum et al. (1978); Blohn et al. (2009)) but essentially no theoretical work at all. But theoretical works

are necessary to fully understand the details of the motion of this type of particles so as to make meaningful assessment of their impact on cloud microphysical processes. The lack of theoretical work was apparently due to the difficulty in treating the unsteady motion of such a nonspherical particle moving at relative high Reynolds number range (several hundreds and above) when the computing technology was still of limited capability at the time. With the advance of computer technology, it is now possible to perform some computations of the flow past conical particle that are closer to reality. The present paper reports some preliminary computational results of the flow fields past a typical conical graupel falling at different inclination angles.

Graupel has been studied a small amount in an experimental and theoretical manner (Blohn et al. 2009). This study focuses on the theoretical simulation of flow fields around a falling conical graupel and their impacts on the collision growth of the graupel colliding with super cooled cloud droplets. We chose the conical graupel, where the other types are hexagonal and lumped, because they are the most frequently observed and the type most likely to become hail (Knight and Knight 1973). The conical feature of the graupel causes a flow field different than a sphere of it size would and an oscillatory fall pattern, warranting the study of its flow fields at different inclinations to understand how a change of that form would alter collision growth.

Using a combination of a commercial computational fluid dynamics simulation tool and a new collision detection program written exclusively for the collisions of supercooled droplets and conical graupel, we can perform computations that allow us to see how these flow fields behave and an accurate view of how they impact the conical graupel collision growth.

This study uses the graupel equation from Wang (1982) that describes the size and shape of the graupel.

$$x = \pm a\sqrt{1 - \frac{z^2}{c^2}}\cos^{-1}\left(\frac{z}{\lambda c}\right) \tag{1}$$

Where y is the horizontal coordinate, z is the vertical coordinate, a is the horizontal

semi-axis length, and c is the vertical axis length. The $\lambda$ variable determines the sharpness of the apex of the conical graupel and can be varied from 1 to $\infty$, with 1 being the sharpest. The actual horizontal axis length or diameter, D, is not defined, so we used the following ratio of D and the height, 2c, to keep our changing graupel diameters the same shape.

$$\frac{2c}{D} =\sim \frac{11}{12} \tag{2}$$

Figure 1 shows an example of a conical graupel with the parameters a= 1 mm, c=1.5 mm, and $\lambda$=1. Its ratio of a to c was not held constant, so its D is 3.67 mm. Table 1 shows the different groups of conical graupel used in this study and their parameters according to this equation.

The goal of this study is to obtain the numerical solutions of the flow fields for each of these graupel, where the smaller sizes were chosen to exhibit steady flow fields and the larger sizes were chosen to show unsteady flow fields with eddy shedding. We insert super cooled droplets into these flow fields far enough from the graupel and solve the equation of motion for the droplets so as to determine their grazing collision trajectories. From such grazing trajectories we can determine the collision efficiencies for the different droplet sizes and the graupel.

# 2. Methods

The experiments are carried out by modifying an input file for the streamer FORTRAN suite and python is used to parse the results and present them in a readable format.

### *a. FLUENT*

ANSYS FLUENT software was used to numerically solve the unsteady Navier-Stokes equations for flow past conical graupel.

$$\frac{\delta \vec{u}}{\delta t} + (u \cdot \vec{\bigtriangledown})\vec{u} = -\frac{\bigtriangledown p}{\rho_a} + v \bigtriangledown^2 \vec{u} + \vec{g} \tag{3}$$

$$\bigtriangledown g\vec{u} = 0 \tag{4}$$

The solver uses a mesh based on a finite volume method and finds the mass conservation through the faces of the mesh with a pressure solution algorithm. It is considered segregated, where the governing equations (continuity and momentum) are solved in order and because of that, it is iteratively solved. Figure 2 shows the process of the solver. We utilize two versions of the solver, transient and steady. The steady solution never truly converges fully because of the unsteady nature of our simulations, but the flow field solution is considered steady when it shows periodic flow. This solution is achieved before allowing the solver to advance in time, reducing computation time and creating better results.

There are different diameters and different shapes (determined by $\lambda$) for the graupel we are studying and are assumed to be falling at terminal velocity. The velocity of each graupel is can be found with

$$V_\infty = \frac{v\mathrm{Re}}{D} \tag{5}$$

We use terminal velocities similar to Locatelli and Hobbs (1974) of conical graupel. Three numerical simulations were carried out in this study. The first simulation looks at different diameters of graupel ranging from .5 mm to 5 mm and the width to height ratio is (find this). The second simulation looks at one size of graupel (a=1 mm; c=1.5 mm; $\lambda$ = 1) and the different angles of inclination ranging from 0 to 60 degrees. The last simulation examines a similar graupel from the second experiment, but with a different shape ($\lambda$=5). It also looks at the inclination from 0 to 45 degrees. Table 1 lists the various parameters of each experiment group.

Before we can begin our simulation, we need to design a computational domain for the flow fields around the graupel to be solved in. Instead of simulating the graupel falling in air,

we treat the equivalent problem of air passing the graupel at the graupels terminal velocity. For graupel sizes 2 mm and larger we created a cylinder with a 2 cm radius and a 5 cm length to act as the outer boundary. The smaller graupel particles used a 1 cm radius and 3 cm length outer boundary. In each case, the graupel particle was placed 1 cm into the outer boundary, allowing room for a uniform flow field at the beginning of the outer boundary (Figure 3).

The ANSYS meshing program took the outer boundary, without the volume of the graupel, and gave it a fine tetrahedral mesh. The maximum face size was set to be the size of the graupel and the minimum was set to be one-tenth the size of the graupel. The resulting mesh is finer towards the graupel particle and becomes coarser as you move away from the graupel (see Figure 4).

The mesh is imported into FLUENT and it is given the property of air, where the viscosity, $\nu$, is $1.7 \times 10^{-5}\,\mathrm{kg/ms}$, the pressure, p, is 800 hPA, and the temperature, T, is $-8\,^{\circ}\mathrm{C}$. The graupel particle itself is rigid and does not need a property. The bottom face of the outer boundary is an inlet producing a flow field of the graupels terminal velocity and the top face of the outer boundary is considered as a pressure outlet.

FLUENT needs reference values in order to compute the drag coefficient of the graupel inside the outer boundary. The area is taken from the projected area on the bottom of the graupel and the length is the diameter of the graupel. The drag coefficient is computed from the face of the graupel in the z-direction (the length of the outer boundary).

FLUENT has a wide variety of solution methods, but we have chosen certain solvers for this simulation. The velocity is found with the Pressure-Implicit with Splitting Operators (PISO) pressure-velocity coupling scheme. It satisfies the momentum balance after the pressure-correction of the solver is finished and couples with its neighbors to correct the mass flux. PISO is ideal for high gradients of velocity because of this behavior and can handle rapidly changing mesh face sizes.

The gradients (the value of a scalar at the cell face) are determined by the least squares

cell based method. It has a high accuracy for determining the gradient of skewed and distorted meshes like the one used in this experiment.

The PREssure Staggering Option (PRESTO!) pressure solver uses continuity balance to find the pressure of each mesh face. PRESTO! handles high pressure gradients very well and can determine high-speed rotating flows. For the momentum, we use the second order upwind method. The second order upwind was chosen because the first order upwind would have difficulty working with the tetrahedral grids as the flow is rarely inline with the grid.

Since flow fields we are using in this simulation are unsteady, so it is important for us to begin the simulation by placing a velocity perturbation. A y-velocity perturbation 30% of the inlets velocity is placed above the graupel and only on one side of the outer boundary. This initialization causes the flow to become unsteady in appropriate Reynolds number range. When Re is small, the flow returns to steady. But when Re is large enough, the flow continues to develop into a quasi-periodic unsteady flow with eddy shedding (Figure 5).

We make our steady solution at this point until the solution achieves a periodic flow. Once the solution has a periodic flow, we can advance the time of the solution with the transient solution. The time step for every experiment in this study is $1 \times 10^{-3}$ seconds. Where we can see at least 40 time steps for every period of the unsteady flow. The solution is exported to be used in the collision efficiency program every two time steps, which gives the data sets a time step of $2 \times 10^{-3}$ seconds.

*b. Collision Efficiency*

To determine the collision efficiency we used a FORTRAN program to calculate particle grazing collision trajectory (see Pruppacher and Klett (1997)) of the supercooled droplets at various sizes and distances from the conical graupel center to determine the collision efficiency of the graupel particle. It loads the FLUENT files and processes them with a self-generated conical graupel particle. It then builds a list of droplet sizes that it runs through the program. Each droplet size is testing for the optimal time step that the droplet path

can be calculated at. After determining the terminal velocity of the supercooled droplet, it inserts the droplet into the outer boundary and advects it forward with the flow field. The droplet is subject to drag and gravity forces until it either collides with the conical graupel or leaves the outer boundary. This process is repeated until the program finds the critical angle of the droplet and calculates that droplets collision efficiency. The program starts iterating the next particle until the list is exhausted. Figure 6 is a flow chart of this entire process.

After the flow fields have been computed by FLUENT, full flow fields of the outer boundary are exported every two time steps of the simulation. One unsteady flow field oscillation is loaded into the collision efficiency program and it runs them on a loop to conserve memory. In figure 7, there is an example of the lift coefficient for the 3 mm diameter case. We chose from 0.1282 to 0.1468 seconds to use as the flow field oscillation.

After one unsteady flow oscillation is loaded, the program draws a 3-D shell of the conical graupel particle using the equation stated in the background section. The coordinates of the shell and inside the shell are set to have zero velocity. The shell is also used to determine when the supercooled droplets have collided with the graupel using the point in plane algorithm (to be discussed later). The velocity values from the FLUENT simulation file and the points from the rendered conical shell are initialized together as the flow field that the program uses. Since the FLUENT simulation defines its grid in a mesh plane, we take the center of each plane and assign it a velocity in the x, y, and z direction. Since these node centers are not equally spaced, we use Shephard's method to average the flow correctly. Shephard's method is used for averaging any given point with a non-uniform grid, we use it for finding the flow velocity and when calculating the grazing collision trajectories.

The flow field velocity coordinates are not ordered in any way, so the program needs to determine where the current coordinate is in relation to the flow field coordinates. It scans a cloud of coordinates no more than 2 mm away from the current coordinate and determines the four nearest neighbors to the current coordinate. The program did not initially weigh the average of the nearest neighbors and it created a smoothing effect on the flow field

data. In order to reduce the smoothing, we used the Shephard's method for inverse distance weighting. Shephard's method uses the distance from the current coordinate to the nearest neighbors and finds the total weight, $w_{net}$ of the neighbors.

$$w_{net} = \sum_{i=0}^{n} \left( \frac{\mathrm{R} - d_i}{\mathrm{R} d_i} \right)^2 \tag{6}$$

with

$$d_i = \sqrt{(x - x_i)^2 + (y - y_i)^2 + (z - z_i)^2} \tag{7}$$

Then, it calculates a value $w_i$, which determines the weight given to each neighbor.

$$w_i = \frac{\left( \frac{\mathrm{R} - d_i}{\mathrm{R} d_i} \right)^2}{w_{net}} \tag{8}$$

The sum of the four nearest neighbors multiplied by their weight creates the velocity found at the current coordinate. This creates a great approximation of the FLUENT flow field and allows us to see the initial velocity planes that fluent used in its Navier-Stokes calculations, figure 8 shows the difference between the straight averaging method and shepherds method.

Notice the velocity cells with the Shephard's method interpretation of the flow field. Straight averaging causes numerical errors and unintentionally smooths the flow field.

In order to keep the velocity zero inside the conical graupel shell, we use the point in polygon method to see if the data point is inside the shell. Finding if a point is inside 3-D coordinates can be difficult, so the conical graupel shell is divided into 2-D planes. The program decides where the current coordinate lies relative to the shell and creates the two nearest planes from the conical graupel equation. Then it creates a plane using linear splines that are on the same z-coordinate plane as the current coordinate; figure 9 is a diagram of this process. The winding number of the current coordinate is found by determining the angles subtended by each side of the polygon. If the sum of the angles reaches $2\pi$, then the current coordinate is considered to be inside the polygon. All coordinates inside the polygon

are set to a zero velocity. This point in polygon method is also used to determine hits during the collision detection process.

After the data is loaded and assimilated with the 3-D conical graupel shell, the program generates a list of droplet sizes to run the collision efficiency tests against. It begins the tests at 0.1 µm and continues to 0.2 µm, 0.3 µm, and so on until it reaches the next decade and begins a new sequence of 10 droplets per decade. When the program looks at 10 µm and above it expands the amount of droplets to 100 per decade, so that the collision efficiency can be clearly defined. The droplet size determines the tolerance that the critical angle may be defined at by four orders of magnitude. For example, a 0.1 µm droplet needs to have its critical radius defined within $1 \times 10^{-5}$ µm.

For the program to have faster runtimes and a realistic simulation, it determines the time step for each droplet size. It creates a base time step of $2 \times 10^{-4}$ seconds and a data change of once per time step, which is the time step of the data that was loaded into the program. The maximum time step allowed is based on the minimum amount of time steps to create a hit on the graupel particle at the maximum velocity inside the outer boundary. In order to reduce large changes in momentum, the minimum amount of time steps to reach the graupel is set to three hundred. Then it tests the droplet by looking at what the velocity would be for that size and in the base of the outer boundary. If the time step is too large and the velocity of the particle is unstable, where it would be extremely large or negative, the program drops the time step by an order of magnitude. This also adjusts the rate of change for the flow field. As the time step reduces, the rate for the flow field data to change becomes lower.

For the larger particles in a outer boundary of a small velocity, a base time step of $2 \times 10^{-4}$ seconds may be too small. So the program determines if a time step is too slow and increases it by an order of magnitude. This speeds up the simulation considerably. It also changes the rate of flow field data changing by skipping flow field time steps. This does not cause any jagged paths as each time step only uses one set of flow field data. After the time

step finder is finished, it uses that information for all the droplet paths of a certain size.

The marching function that calculates the droplet sizes first determines where the particles will be inserted into the outer boundary. The droplet is placed ten of its radii away from the droplet in the z-direction and at the conical graupels radius in the y-direction. In the unlikelihood of droplet hitting the graupel from this starting point, it would have a collision efficiency of one. Now that the starting point is determined, the marching function can begin simulating the droplet paths.

For the first step of the marching function, the program determines the terminal velocity of the droplet. If the terminal velocity is faster than the velocity of the outer boundary, the droplet falls through the outer boundary and receives a collision efficiency of zero. The program calculates terminal velocity for droplets in three regimes defined by Beard (1976). Their equivalent radius, $a_0$, separates these regimes. The first is small cloud droplets, 0.25 µm $< a_0 <$ 9.5 µm, the second is large cloud droplets, 9.5 µm $< a_0 <$ 535 µm, and the third is raindrops, 535 µm $< a_0 <$ 3500 µm.

The first regime deals with primarily steady flow around the droplets and the terminal velocity can be calculated with Stokes drag. Beard (1976) shows that Stokes terminal velocity, $V_\infty$, can be multiplied by the slip correction factor, $C_{sc}$, to get the correct terminal velocity.

$$V_\infty = \frac{(\rho_w - \rho_a) g C_{sc} 2 r_d}{18 n_a} \tag{9}$$

where

$$C_{sc} = l + 2.51 \frac{1}{2 r_d} \tag{10}$$

with

$$l = l_0 \left( \frac{n_a}{n_0} \right) \left( \frac{P_0}{P} \right) \left( \frac{T}{T_0} \right)^{\frac{1}{2}} \tag{11}$$

$$l_0 = 6.82 \times 10^{-10}\,\mathrm{m/s^2} \qquad P_0 = 101\,300\,\mathrm{Pa} \tag{12}$$

$$n_0 = 1.818 \times 10^{-5}\,\mathrm{kg/ms\ \ at\ 20\ ^\circ C} \qquad T_0 = 293.15\,\mathrm{K} \tag{13}$$

Calculated with the mean free path, $l$, the pressure dependence of the mean free path, p, the dynamic viscosity, $n$, and the temperature, T.

For the second regime, $9.5\,\mu\mathrm{m} < a_0 < 535\,\mu\mathrm{m}$, the droplets behave as a rigid sphere and can be related to the terminal velocity with a function of the Reynolds number, $\mathrm{N_{Re}}$, and the drag coefficient, $C_d$ (Davies 1945). Beard (1976) showed that $C_d\mathrm{N_{Re}^2}$ can be related to the Reynolds number by the following equations.

$$C_d\mathrm{N_{Re}^2} = \frac{32 r_d^3 (\rho_w - \rho_a)\rho_a g}{3 n_a^2} \tag{14}$$

with

$$X = \log\left(C_d\mathrm{N_{Re}^2}\right) \tag{15}$$

and

$$Y = B0 + B1X + ... + B6X^6 \tag{16}$$

where

B0 = -3.18657 $\quad$ $\mathrm{B1} = 9.936\,96 \times 10^{-1}$ $\quad$ $\mathrm{B2} = -1.53193 \times 10^{-3}$

$\mathrm{B3} = -9.870\,59 \times 10^{-4}$ $\quad$ $\mathrm{B4} = -5.788\,78 \times 10^{-4}$ $\quad$ $\mathrm{B5} = 8.55176 \times 10^{-5}$

$\mathrm{B6} = -3.278\,15 \times 10^{-6}$

and taking the exponential of Y gives us $\mathrm{N_{Re}}$,

$$\mathrm{N_{Re}} = \exp\left(Y\right) \tag{17}$$

Finally, the terminal velocity can be found

$$V_\infty = \frac{n_a \mathrm{N_{Re}}}{2\rho_a r_d} \tag{18}$$

Wang and Pruppacher (1977) experimentally verified these equations with a drop-acceleration experiment inside the UCLA Rain-Shaft.

The third regime, $535\,\mu\mathrm{m} < a_0 < 3500\,\mu\mathrm{m}$ , has rain drops that create an unsteady wake when they fall. This requires the addition of the physical property number, $\mathrm{N_p}$, and the Bond number, $\mathrm{N_{Bo}}$. These dimensionless group relations were found experimentally (Garner and Lihou 1965). Starting with the relation Beard (1976) showed between the Reynolds number and the physical property number.

$$\mathrm{N_{Re}} = \mathrm{N_p^{\frac{1}{6}}} \exp\left(Y\right) \tag{19}$$

where

$$Y = B0 + B1X + ... + B5X^5 \tag{20}$$

with

$$\begin{array}{lll} B0 = -5.00015 & B1 = 5.23778 & B2 = -2.04914 \\ B3 = 4.75294 \times 10^{-1} & B4 = -5.42819 \times 10^{-2} & B5 = 2.38449 \times 10^{-3} \end{array}$$

and with

$$\mathrm{N_p} = \frac{\sigma_{w/a}^3 \rho_a^2}{n_a^4 g(\rho_w - \rho_a)} \tag{21}$$

$$\mathrm{N_{Bo}} = \frac{4(\rho_w - \rho_a)g}{3\sigma_{w/a}} 2r_d^2 \tag{22}$$

$$X = \log\left(\mathrm{N_{Bo}}\mathrm{N_p}^{\frac{1}{6}}\right) \tag{23}$$

The large size of the droplets causes the droplet to warp and the surface tension of the droplet has an effect on the terminal velocity. We can find the surface tension as it relates to temperature from

$$\sigma_{w/a} = \sum_{i=0}^{6} a_n T^6 \tag{24}$$

In order to find the coefficients $a_0$ through $a_6$, we must take a curved fit from the experimentally determined surface tensions. Dorsch and Hacker (1951) looked at the variations of surface tension from -20 to 40 °C and Gittens (1969) determined the variations from -45 to $-20$ °C. From this information, we determine the fit curve in Figure 10 and the coefficients for -45 to 40 °C. Pruppacher and Klett (1997) used a similar method was used to find the surface tension.

$$\begin{aligned} a_0 &= 7.56672 \times 10^{1} & a_1 &= -1.74973 \times 10^{-1} & a_2 &= 1.28253 \times 10^{-3} \\ a_3 &= 7.90607e \times 10^{-5} & a_4 &= -2.14647 \times 10^{-6} & a_5 &= -7.20929 \times 10^{-8} \\ & & a_6 &= 1.67237 \times 10^{-9} & & \end{aligned}$$

Droplets 3500 µm and larger have terminal velocities of at least 10 m/s and are too fast to be calculated with the speed of the graupel examined in this study. For all the regimes, the conditions inside the outer boundary are assumed to be at 800 hPa in the atmosphere with a temperature of $-8$ °C (265.15 K). We can determine the density of air, $\rho_a$ with

$$\rho_a = \frac{\mathrm{P}}{RT} \qquad\qquad R = 287.05 \tag{25}$$

and the dynamic viscosity, $n_a$ by Pruppacher and Klett (1997)

$$n_a(\text{poise}) = (1.718 + 0.0049T) \times 10^{-4}, \quad T(^\circ\mathrm{C}) \leq 0^\circ\mathrm{C} \tag{26}$$

$$n_a(\text{poise}) = (1.718 + 0.0049T - 1.2 \times 10^{-5}T^2) \times 10^{-4}, \quad T(^\circ\text{C}) > 0^\circ\text{C} \tag{27}$$

After the terminal velocity is calculated and it is determined the droplet will not fall away from the graupel, we can begin simulating the droplet path. The program uses a combination of the second-order Runge-Kutta method and applying the trajectory model proposed by Miller and Wang (1989).

$$\frac{d\mathbf{v}(t)}{dt} = \frac{1}{m_p}[\mathrm{F}_d\mathrm{F}_e - \mathrm{F}_g + \mathrm{F}_{th} + \mathrm{F}_{df}] \tag{28}$$

Since the conical graupel is assumed to not have any electrical charge, temperature gradient, or a flux of water vapor, there will be no effects from the electrostatic force, $\mathrm{F}_e$, the thermophoretic force, $\mathrm{F}_{th}$, and the diffusiophoretic force, $\mathrm{F}_{df}$. Leaving the buoyancy corrected gravitational force, $\mathrm{F}_g$, and the drag force, $\mathrm{F}_d$. This leaves us with

$$\frac{d\mathbf{v}(t)}{dt} = \frac{1}{m_p}[\mathrm{F}_d - \mathrm{F}_g] \tag{29}$$

where $\mathrm{m}_d$ is the mass of the particle calculated by

$$m_d = \frac{4}{3}\pi\rho_w r_d^3 \tag{30}$$

with $\rho_w$ the density of the super cooled droplet assumed to be $1000.0\,\mathrm{kg/m^3}$ and $r_d$, the radius of the droplet. We determine $\mathrm{F}_g$ with $g$, gravity acceleration, and a buoyancy correction.

$$\mathrm{F}_g = m_p g\frac{\rho_w - \rho_a}{\rho_w} \tag{31}$$

The drag force on the super cooled droplet is

$$\mathrm{F}_d = 6\pi n_a r_d\frac{u - v_d}{C_{sc}} \tag{32}$$

where u is the velocity at that position and $v_d$ is the droplets velocity in the previous step. The slip correction factor (calculated differently than before), $C_{sc}$, is negligible for the larger drops but it affects the drop sizes of 50 $\mu$m and smaller.

$$C_{sc} = 1.0 + \alpha N_{kn} \tag{33}$$

where

$$\alpha = 1.26 + 0.40 \exp\left(\frac{-1.1}{N_{kn}}\right) \tag{34}$$

with the Knudsen Number, $N_{kn}$

$$N_{kn} = \frac{\lambda}{r_d} \tag{35}$$

where $\lambda$ is the mean free path of the air molecules. (Note: the drag force needed to be corrected for larger particles, see the Appendix for details). The second-order Runge-Kutta helps reduce computational error by splitting the calculation into two half steps.

$$v_k = d\mathbf{v}(d_k, t) + v_d \tag{36}$$

Use the new velocity, $v_k$, to calculate the half-step particle position.

$$d'_k = \frac{dt}{2} v_k \tag{37}$$

Calculate what the velocity would be at the next location.

$$v'_k = d\mathbf{v}(d_k, t) + v_d \tag{38}$$

The determine the full step, we need to add the new position change to the previous location.

$$d_{k+1} = d_k + dt v'_k \tag{39}$$

The droplet velocity and a new position are calculated in the first step, these values are then used to determine the velocity and new position from the second step. Figure 11 illustrates this process.

The program simulates the droplet until it either hits the conical graupel or exits through the top out the outer boundary. A successful hit is determined when the droplet passes within one droplet radius of the conical graupel. This process is repeated iteratively until it determines a initial offset, $y_c$. The program can also determine when the droplets have stalled and it determines them as misses.

Once $y_c$ is found, we can calculate the collision efficiency, E. The collision efficiency is the effective cross-section of the collision between the graupel and the super cooled droplet. Since the graupel is a non-uniform shape, we use collision efficiency from Wang (1983) using gravitational collision kernels.

$$E = \frac{K}{K^*} \tag{40}$$

where K is the collision kernel and K* is the geometric kernel. The geometric kernel is the volume that the graupel sweeps out of the air per unit time, defined by the sum of radius of the graupel, $a_1$, and the radius of the droplet, $a_0$. For tilted drops, $a_1$ is the effective radius of the graupel.

$$K^* = \pi(a_0 + a_1)^2 v \tag{41}$$

and the effective kernel is the volume of droplets per unit time that collide with the graupel within the critical radius.

$$K = \pi(y_c)^2 v \tag{42}$$

By using the size ratio (also referred to as the interception efficiency), $(a_0/a_1)$, we can compare how each diameter graupel captures droplets of increasing size.

# 3. Results

We will first present the results of the flow field calculations and discuss the collision efficiency results thereafter.

*a. Flow Fields*

In order to understand the impact of the inclined orientation during the fall on the flow characteristics, we performed calculations for inclination angles varying from 0° (i.e., vertical as the orientation in Figure 12) to 45° at 5° interval. While the graupel orientation is inclined, its fall path is assumed to be vertical. Experimental observations by Jayaweera and Mason (1965) and Pflaum et al. (1978) showed that an inclined conical body may fall in a helical path whose flow field is difficult to model directly. However, since the characteristic time of the flow field is on the order of tens of milliseconds (Hashino et al. 2010) and the helical motion frequency of the graupel is a few hertz (Pflaum et al. 1978). This implies that the period of the helical motion is normally longer than 0.1 s which is much longer than the characteristic time. Thus the air would have quickly adjusted to the changing position of the graupel, and hence the flow field we calculated should be close to the instantaneous flow field. In our study, we assume that the conical orientation is fixed but the air may perform helical motions. Jayaweera and Mason also stated that for Re $>$ 800, the flow becomes turbulent and the cones may tumble as they fall. In the present study the tumbling motion is not considered as the Re is smaller than that.

In the following, we will describe the flow field characteristics of the uninclined and inclined (using the $\theta = 30°$ as an example) graupel and discuss their differences. We also describe some possible impacts of such flow fields on the cloud microphysics.

1) Changing inclination with $\lambda = 1$ ($\theta = 0$)

An example of the flow around the uninclined case ($\theta = 0$) of $\lambda = 1$ on the y-z plane is shown in figure 12. The vectors show the direction of the flow field. Note that these vectors are the projections of the 3-D vectors onto the y-z plane, so not all vectors are on the same plane. The vectors are concentrated near the graupel in order to capture the more complicated flows and less concentrated further away from the graupel where the gradients of the flow are not as high, this is a result of the fine mesh near the graupel and the coarser meshing further away from the surface. At this time in the simulation, an eddy on the left side of the graupel is about to be shed, which is the main driver for the periodic (or quasi-periodic) flow downstream of the graupel. The waving of the unsteady flow diminish further downstream of the graupel (about 2-3 times the graupel height).

Upstream of the graupel, the flow is steady, but shifts around the graupel where it is approaching a high pressure region. Any calculations of the physical properties would have to begin far enough upstream where the flow is unchanged. The graupel mainly affects flow within a vertical column of its fall path, only disturbing a small amount of the outside area up to a few diameters. It is important to note that the flow is not purely periodic; the 3-D nature of this simulation creates a quasi-periodic flow. The x-z plane shows similar flow patterns and will not be shown or discussed.

Figure 13 shows two randomly chosen frames in the simulation where we can see how the periodic nature of the flow changes the pressure around the graupel. In the rest of this study, the unsteady flow figures will be chosen for the flows effects on various characteristics (pressure, velocity magnitude, and vorticity magnitude).

As the flow is unsteady, there will be vortex shedding in the downstream. Unlike the case of a two-dimensional infinite cylinder where an alternating leftright shedding vortices form the familiar regular von Karman vortex street (see, for example, Dyke (1979), p. 57, Fig. 96), the shedding in the present case is of 3-D nature and the vortex structure appears to be much more complicated. In the following, we shall first examine the pressure distribution

and then the vortex shedding.

These frames show the typical pressure distribution in unsteady flow: high pressure upstream and alternating low pressure pattern downstream of the graupel. The magnitude and gradient of the high pressure upstream of the graupel has little or no change as the flow oscillates. The low pressure center, however, shifts back and forth between the left and right side of the graupel. Although, the magnitude at the center of each low pressure center is different and the gradient of pressure is not as strong on the right as it is on the left. This difference leads to the quasi-periodic nature of the flow, where the oscillation is not quite balanced. Allowing the simulation to run for longer than 0.2 seconds (2000 time steps) could be achieve balance, but we believe the error is low enough to not make much of a difference.

Looking at the velocity magnitude (Figure 14), we can see the waving motion of the flow and the oscillating maximum velocity on the left and right sides of the graupel. A vortex on the left side of the graupel remains in both time steps, but it is weakened by the shift in pressure. It looks like there is a bias to this side.

When considering the vorticity magnitude (Figure 15), we see that the vortex does shift from one side to another (although with a lower strength). The highest vorticity is on the waist of the graupel with the other regions of high voticity in the eddies in the wake. We can see that the higher vorticity of the eddies directly corresponds to the lower pressure regions. The height of the vorticity is affected when on side generates an eddy, curving it towards the center of the graupel. The velocity magnitude is also higher in the regions of high vorticity on the sides of the graupel. Where the lowest velocities are inside the eddy vorticies.

Figure 16 shows the vector field along with an isosurface region of -2 Pa in 3-D. There are two low pressure features of interest. The first is a low pressure ring around the base of the graupel that shifts as the periodicity of the flow changes. A larger bulge shows a deeper pressure region. The low pressure region in the wake looks like a larva rotating around the top of the graupel. Its shape is chaotic, where it bulges and shrinks, showing the deepening or weakening of the low pressure. It also breaks into two or more regions, or can

grow or shrink in length, which also shows the deepening or weakening of the low pressure and vorticity. The larva rotates around the z-axis, but it shifts between rotating clockwise and counter clockwise and changes the speed of the rotation. We are not sure if this is the actual behavior of a pressure region behind a graupel or an artifact of the simulation and non-uniform mesh.

### 2) Changing inclination with $\lambda = 1$ ($\theta = 30$)

We ran simulations of increasing inclination from 5° to 45°, the $\theta = 30$ case is representative of the changes that inclination brings to the flow. Smaller and larger inclinations provide the same effects to smaller and larger magnitudes, respectively.

When we look at the pressure distributions in Figure 17, we see that the high pressure center is not directly in the middle of the graupel, but is now seated slightly to the left. This will deflect aerosol particles form this area and cause them to hit higher up on the graupel, if at all. The low pressure centers hugging the sides of the graupel have changed as well. The left side of the graupel has moved upward on the graupel and has intensified, which is due to the change in the location of the high pressure center. The right side of the graupel sees a weaker and lower low pressure center. The bias of the wake alternating low pressure centers have shifted to the right side of the graupel due to the inclination. The alternating pressure centers are fairly balanced, but they are much more unbalanced with the inclined graupel and end up biasing the flow to that side as well.

Figure 18 shows the velocity magnitude and its bias towards the right side of the graupel. You can still see that the upstream area is mostly steady and does not change until you reach the high pressure region. The more noticeable changes are the inclination in flow to the right of the graupel, shifting the column of unsteady wake from the uninclined case. Another difference relating to the high velocity on the sides of the graupel is the weaker right side. Although, when an eddy is shedding the right side strengthens considerably (seen in frame b). This causes a slight pulse of the wake to the right, but it is instantly countered

by an eddy shedding on the left side to bring the wake bias back to the right.

The vorticity magnitude of the inclined case can be seen in Figure 19. The incline causes the height and magnitude of the vorticity to be larger on the right side of the graupel even when the left side is shedding an eddy. There is also a large difference between the vorticity in eddies shed on the right side versus those shed on the left, the right has a much stronger vorticity. The vorticity on the right side also starts lower on the graupel, this is due to the pressure gradient shifting to the left side.

The isosurface of -2 Pa pressure is shown in Figure 20. The band of pressure around the side of the graupel is mainly on the left side and it is higher on the graupel. Its only fluctuation is the change in bulging which is still chaotic. The larva behaves differently from the inclination as well, where it is always larger on the right than it is on the left. Interestingly, it gains a non-chaotic motion. The larva grows on the right side, moves counterclockwise around the z-axis to the left, and shrinks on the left side until it disappears and the process starts again.

### 3) Flow fields of a falling graupel with a diameter of 3.17 mm and shape parameter $\lambda = 5$

We ran a simulation using the same parameters as the tilt cases before, but with $\lambda = 5$. This gives the graupel a rounder more spherical shape. Its Reynolds number is 500 and it behaves with an unsteady flow. We see many of the same characteristics as the $\lambda = 1$ case but there are a few differences.

Figure 21 shows the pressure differences around the graupel. This graupel has a larger low pressure area around the waist of the graupel due to the rounder edge. There is also an alternating low pressure center in the wake, which is a characteristic of unsteady flow. But there is a much lower pressure center and a weaker gradient than the $\lambda = 1$ case. From the curvature of the bottom of the graupel, the high pressure area takes up a smaller amount of area.

The velocity magnitude is shown in figure 22. There is not much difference between the previous case and the current case. There are strong velocity areas on the sides of the graupel, low velocity from the high pressure center on the bottom, and swirling velocity from the eddies. However, we can see that there is a lower velocity in the wake of this graupel. This attribute is from the larger spherical shape blocking the flow and is almost similar to how a sphere would behave in this situation.

Figure 23 shows us the vorticity magnitude of the $\lambda = 5$ case. The vorticity is attached to more of the surface of the graupel, where we saw the increased low pressure area at the waist. The eddies coming off of the graupel have a lower magnitude than the $\lambda = 1$ case. It looks like the reduction in velocity behind the graupel has dampened the vorticity of the eddies.

We have an isosurface of -1.5 Pa with the velocity vectors in figure 24. The behavior of the larva in the wake is exactly the same as the $\lambda = 1$ case. The low pressure band on the waist of the graupel covers a larger area. It is also important to note that the slant of the band is different in this case, that may be a result of the meshing or the perturbations we inserted into the simulation to achieve unsteady flow more quickly.

### 4) Steady and Unsteady flow fields of falling graupel with changing size and a shape parameter of $\lambda = 1$

We ran six simulations of graupel with different radii and kept their length to width ratio the same. These simulations had the diameter 0.5 mm, 1 mm, 2 mm, 3 mm, 4 mm, and 5 mm. The 0.5 mm and 1 mm cases show steady state flow and the 2 mm and higher cases show an unsteady flow field like the cases we have seen before.

Lets first look at the cases of steady flow of 0.5 mm and 1 mm. Figure 25 shows both cases with their pressure distributions. Since the flow is steady, we do not need to show two time steps of the simulation. Both cases show a balance between the two low pressure centers on the sides of the graupel. The 1 mm case has a lower center and a higher gradient

from the increased speed of the flow around the graupel. There is also a high pressure area centered on the bottom of both graupel particles.

Figure 26 shows the velocity magnitude of both steady flow cases. They both have a slower speed on the bottom of the graupel where the high pressure is and a lower velocity in their wake. The 0.5 mm graupel has a smaller wake and does not affect the surrounding area as much as the 1 mm graupel does. This is a factor of the size of the 1 mm graupel and the speed around the 1 mm graupel. We can start to see the beginnings of unsteady flow in the 1 mm graupel. It shows higher velocity jets on the sides of the graupel and a small downward velocity on the z-axis.

The vorticity of each case is found in figure 27. Due to the higher speed of the flow, we can see that the maximum vorticity is higher in 1 mm than it is in 0.5 mm. The vorticity on the 0.5 mm case touches most of the sides of the graupel. The small peak size and low flow speed allow it to almost reach around the top of the graupel. Both cases show a balanced vorticity on both sides of the graupel.

In the isosurface of the negative pressure differences (figure 28), only the band of low pressure exists around the waist and there is not a larva in the wake of the graupel. The band of low pressure covers the sides more than the 0.5 mm case, but that is because the selected isosurface is of a different value (although same percentage change in pressure). We can also see a faster upstream flow for the 0.5 mm case and the beginning of eddy formation on the 1 mm case.

Once the graupel diameter is 2 mm or greater ($> 222$ Re), we start to see unsteady flow as described before in the $\lambda = 1$ case. Since those flow fields are similar, we will only look at the 5 mm case at two different time steps to see how a large graupel diameter can change the flow.

Figure 29 shows the pressure distribution for the 5 mm case. We see the same high pressure at the bottom, low pressures on the sides of the graupel, and an alternating low pressure center in the downstream wake of the graupel. The magnitudes are much larger

than all the other cases, mainly attributed to the high flow speed and large size of the graupel. However, this 5 mm graupel shows the closest periodicity that we have seen in all of the unsteady flow cases. The magnitude and the gradient of the low pressure centers in the wake are very similar in both time steps even though they are on the right and left sides of the graupel.

There is the same level of periodicity shown in the velocity magnitude (Figure 30). The downward velocity in the center of the graupel wake is similar in shape and almost the same in magnitude. The 5 mm case has the largest eddies and wake of any of the other cases where the high speed of the flow (3.88 m/s) and the diameter of the graupel make the largest impact. The high velocity jets on either side of the graupel show an interesting feature of having a jet near the base of the graupel and another near the top height of the graupel. These features are the result of a higher frequency of eddy shedding than any of the other cases.

Figure 31 shows the vorticity magnitude of the graupel. The vorticity is attached to the bottom, but they have a large gap between each side. There is also a higher attachment of the vorticity to the sides, the high velocity and high pressure on the bottom may be driving the highest regions of vorticity further up the side of the graupel. We can also see that the periodicity is more balanced here. The heights of the right and left side switch every period, with the lower side forming an eddy.

We have an isosurface of -6 Pa in figure 32. The band around the waist of the graupel is fairly uniform, unlike the other cases. This further shows the balanced nature of the periodicity and may be a sign that the periodicity is fully established in the flow. The larva rotates around the top of the graupel in a mainly clockwise rotation, only switching for a handful of the time steps.

### 5) Frequency and Drag Coefficient

All of the unsteady cases (every case but 0.5 mm and 1 mm) produce eddy shedding into their wake. This affects the drag coefficient with a quasi-periodic oscillation, an example of this is shown in figure 33. We calculate the drag coefficient, $C_D$, by using the following formula (Pruppacher and Klett 1997)

$$C_D = \frac{\mathrm{F}_d}{\rho_a u_\infty^2 A} \tag{43}$$

where $F_d$ is the drag force, A is the projected area, $\rho_a$ is the density of the air, and $u_\infty$ is the flow speed of the outer boundary. This can be used to determine the shedding frequency in the same way we used the lift coefficient in the collision detection program.

Figure 34 shows the change in shedding frequency with inclination angle from $\theta = 0$ to $\theta = 45$. The frequency of shedding increases as the inclination increases, as the area for the alternating low pressure center shrinks with inclination. We can fit the data points to the polynomial:

$$\mathrm{Freq} = 100.09 + 0.6983 \times 10^{-1}\theta - 0.012 \times 10^{-2}\theta^2 \tag{44}$$

where theta is in degrees. The drag coefficient (Figure 35) decreases with increasing inclination. This curve can be fitted with the following:

$$C_D = 53.28 - 1.121\cos(\theta) + 59.61\cos^2(\theta) \tag{45}$$

The $C_D$ appears to be a straight line and since the projected area of increasing inclination also increases linearly, the increase in $C_D$ may be just a function of an increasing projected area. It is also important to note that the $C_D$ is inbetween that of a sphere (0.58) and a circular disk ($\sim$1). The length of an eddy in the wake of the graupel (defined as the furthest disturbance of the pressure by the graupel from the apex of the graupel) shows to be 1.9 times the height of the graupel for each of the inclined cases.

Figure 36 shows the change in shedding frequency for the different diameter cases D = 0.5 mm to D = 5 mm. The shedding frequency also increases with diameter as the Re and $u_\infty$ increase. We can fit the following polynomial to this increase:

$$Freq = -32.31 + 46.724D + 5.2683D^2 - 0.9527D^3 \tag{46}$$

where D is the diameter of the graupel in mm. The drag coefficient decreases until it hits 4 mm where it levels off. The following equation provides a fit for the drag coefficient:

$$C_D = 0.69 + \frac{0.66^2}{D} \tag{47}$$

It is an exponential decay function until it evens out at $C_D = 0.69$. More tests will have to be completed to see if the drag continues to stay level if the diameter increases. The length of the eddy in the wake of the graupel also does not change much with diameter, but the average for this shape is ∼1.4 times the height of the graupel.

The $\lambda = 5$ case has a shedding frequency of 138. If we calculate the frequency of a 2-D cylinder of diameter D = 3.62 mm, $u_\infty = 2.5$ m/s and Re = 500 using the Strouhal formula (Massey 1979)

$$N_{strou} = \left(\frac{fd}{u_\infty}\right) = 0.198\left(1 - \frac{19.7}{\mathrm{Re}}\right) \tag{48}$$

where $f$ is the eddy shedding frequency. The shedding frequency result from this equation is 131, making the $\lambda = 5$ case similar to a 2-D cylinder. The eddy height is the same as previous cases, approximately 1.4 times the height of the graupel.

*b. Collision efficiencies with which conical graupel collide with supercooled droplets*

The collision between supercooled water drops and an ice particle with the drops freeze subsequently on ice is called riming. Riming is a major growth mode for large ice hydrometeors such as graupel and hail. In the following, we present computational results: collision

efficiencies with which conical graupel colliding with supercooled droplets.

Figure 9 shows how the grazing collision trajectory is computed as a collision with the graupel. If the trajectory nears the graupel within a distance of the droplets radius, it is considered a collision. This emulates the riming process as a droplet will freeze to the surface of the graupel once a part of the droplet wall collides with the graupel.

We can analyze the data created by FLUENT and the collision detection program in several ways. The flow field characteristics differ from size, shape, and inclination. With the sizes smaller that 3 mm of diameter we see a steady flow downstream of the graupel, but the larger graupel hydrometeors have unsteady flow. The frequency and drag coefficient of the flow downstream is also affected by the characteristics of the graupel.

Looking at the results from the droplet collision detection program, we will discuss the changes in collision efficiency. They are not only dependent on the size, shape, and inclination, but the droplet axis is also important. We see previously theorized, but never before seen, results from the droplet paths.

### 1) Droplet trajectory behavior

There seem to be five main behaviors of the droplets paths and can be grouped according to collision efficiency and droplet size, E. The first (small droplet size and $E < 0.1$), is stalling and wake capture, where the droplet has a difficult time colliding (Pruppacher and Pitter 1997) with the graupel because of its low momentum and can easily get captured in the graupels wake. The second behavior occurs after the droplets have gained some momentum ($0.1 < E < 0.85$), they begin colliding with the graupel particle closer to the side of the graupel. The third ($0.85 < E < 1.0$), is when the droplets have a relatively large momentum and behave in almost a straight path. The fourth behavior ($E < 1.0$ and with large droplet size) is when the terminal velocity of the droplet is closer to the velocity of the graupel. They move at the same speed of the graupel and their momentum is greatly affected by the flow field. The last behavior (E = 0) is deflection; the droplets are moving almost exactly

the same speed as the graupel. Once they enter the high pressure area at the bottom of the graupel, they are pushed away, deflected, and never collide with the graupel.

We can see these five types of behavior with the 3 mm case in figure 39. Since the flow is nearly symmetrical, we will not show the droplet paths hitting the graupel from the other direction. There is a fair amount stalling in the droplet size (0.8 µm) as it falls in the first behavior, and there may be some wake capture if the droplet gets caught in the wake. The second droplet at 7 µm, shows that it has some momentum and begins getting closer to the side of the graupel at a E = ∼0.5. The 60 µm droplet is flowing in almost a straight path, with a slight deviation into or away from the flow. This deviation depends on which side of the droplet was shedding when the droplet came near the graupels wake.

The 280 µm droplet has a much slower momentum and is affected by the high velocity jet on the side of the graupel. The jet causes the droplets to veer off to the right and starts decreasing the collision efficiency to E = ∼0.85. Finally, at 290 µm, we see that the droplets become deflected by the graupel. They near the high pressure area on the bottom of the graupel and lose all of their momentum and gravity takes over. Once they enter the higher velocity flow, they can increase their speed and momentum, but they ultimately end up missing the graupel.

The steady flow cases (.5 mm and 1 mm), had similar droplet paths as the unsteady flow case. However, no wake capture occurs . While the steady flow still has eddies, they did not capture any cloud droplets. The 1 µm drop shown in figure 39 can be used as an example.

While the 3 mm case had quasi-symmetrical flow, the inclined cases do not. We will take a look at how the inclined cases differ with the $\theta = 45$ case. In order to get a full picture of how the droplets react to this asymmetrical flow, we determined the collision efficiency of the droplets from either side of the graupel. Figure 40 shows the five behaviors from the right side of the $\theta = 45$ case.

The 10 µm droplet gets caught briefly in an eddy, but does not get captured. As we released more and more droplets towards the center of the graupel, none of the droplets

collided with the graupel. This is from the high pressure center resting on the bottom left side of the graupel, pushing the small droplets into the stronger flow. At 15 µm the droplets start to gain momentum, where they no longer get caught in the eddy shedding of the graupel, but they do not collide with the graupel. It is not until 80 µm when the droplets have a large amount of momentum that their E = ∼0.94. The droplets with a radius of 260 µm start to fall away from the graupel and are pushed away with the high velocity jet on the side of the graupel. A 270 µm droplet is not able to hit the graupel due to deflection.

Coming from the left side on the $\theta = 45$ case (Figure 41). At 3 µm , some of the droplets are pushed to the right of the high pressure center and hit to the right of the center of the drop. The droplets that flow around the left side of the graupel get caught in the wake on the right side of the graupel and are captured on the top of the graupel. Droplets with a radius of 1 µm and smaller do not hit the graupel. They end up flowing to the right side of the graupel and get caught in the eddy shedding. At 8 µm the droplet gains some momentum and begins hitting the side of the graupel (E = ∼0.2). When the droplet is 75 µm the momentum peaks and the collision efficiency is large (E = ∼0.94). Where the droplet is 260 µm, we can see the high velocity jet on the side of the graupel is pushing the droplets away from the graupel, reducing the collision efficiency. At 270 µm, the droplets are completely deflected from the graupel.

For $\lambda = 5$, the droplet behaviors are similar to the cases discussed before. However, there is a lack of rear wake capture and droplets being caught in eddies. The strong curvature of the graupel does not allow for droplets to find the eddies before being caught in the main flow. The five droplet behaviors for $\lambda = 5$ are shown in figure 42.

Figure 43 shows a 1 µm droplet colliding on the left side of a graupel with a diameter of D = 3.67 mm and an inclination of $\theta = 15$. This rear wake capture grabs droplets after they barely miss the side of the graupel. The droplets circulate in the eddies and eventually either hit the top of the graupel or continue downstream of the wake. There are some droplets that perpetually circulate in the wake and become stuck in it. These droplets would fall with

the graupel until an external force disturbs the flow. This wake trapping mechanism could explain how some aerosols are removed from the atmosphere, but more work will need to be studied to understand this process.

Long range wake capture can be accomplished by the graupels wake (Figure 44). The droplet must have a terminal velocity close to the graupels and be traveling slower than it. This allows the droplet to speed up to its terminal velocity after it passes the graupel and the flow will slowly bring the droplet into itself. Once the droplet enters the slower velocity wake, its drag force becomes weaker and gravity takes over; drawing the droplet ontop of the graupel. Long range wake capture can capture droplets from up to two times the droplets diameter away. However, for this to work, there must be no other forces acting on the droplet over such a long distance.

Stalling of a droplet happens when the droplet is small and the gravitational force on the droplet is also small. The droplet approaches the graupel, but enters the high pressure area near the bottom and is repulsed and slowed down by the drag force. The droplets velocity slows to near zero when it nears the surface of the graupel and does not have the momentum to collide with it. The weak gravity pulls the droplet down slowly, but the flow field near the base of the graupel moves it laterally instead of upward. The droplet oscillates between the edge of the flow field and a zero velocity area near the surface of the graupel. It either stops moving or slides out from underneath the graupel and continues into the flow field.

Scattering occurs when the droplet has a terminal velocity slightly higher than the graupel and it is falling at that speed. The droplet slowly flows towards the graupel and has enough momentum to strike the graupel as it nears the bottom of the graupel. AS the droplet nears the side of the graupel, its momentum is very small, so the flow that points horizontally at the bottom of the graupel can propel the droplet horizontally scattering it far from the graupel. An example of this is shown in figure 45, where a 353 µm radius droplet is scattered by the a graupel with a diameter of 4 mm.

The collision efficiency is the percentage of droplets in the path of the graupel that it will

acquire as it falls. There are two ways to look at it, as a function of droplet radius and the interception efficiency which is the ratio of the droplet radius to the radius of the graupel.

### 2) Impact of different graupel size on the collision efficiency

The collision efficiency for different graupel size is shown in figure 46 as a function of droplet radius. The largest graupel collects the largest droplets, because of the high velocity flow around the graupel and its large size. The smallest collects the least droplet sizes for the opposite reasons. The D = 0.5 mm case does not have as large as a collision efficiency peak as the others. This behavior is similar to that for drop-drop collision as explained in Pruppacher and Klett (1997).

Figure 47 shows how the collision efficiency of the graupel changes when the cloud droplets have a small enough radius to rime on the graupel. Notice the collision efficiency of all diameters tends to increase quickly around 5 µm.

The collision efficiency as a function of size ratio (Figure 48) has the D = 0.5 mm case as having the highest interception efficiency while the D= 5mm case has the lowest. Also note that the D = 0.5 mm case starts collecting droplets near a 0.03 size ratio (labeled as interception efficiency in the figure), where the larger graupel have collisions at a size ratio much closer to zero. This is from the droplets all start to have enough momentum to collide with the graupel particles around the same droplet radius. The ratio is very small for larger graupel sizes, but larger for the small graupel size.

### 3) Impact of different graupel inclination on the collision efficiency

The inclination cases have overall similar collision efficiency curves, where the difference between all inclination cases is no more than E = ∼0.2 (Figure 49). The difference is more significant at smaller drop sizes than it is at larger drop sizes. The top of the collision efficiency curve is the $\theta = 0$ case, where the bottom of the curve on the legs is the $\theta = 45$

case coming from the right and the bottom of the curve in the middle is $\theta = 45$ from the left.

The collision efficiency with respect to the size ratio is a different case (Figure 50). The changing tilt of the graupel reduces the width of the graupel fall path. This results in having the final interception efficiencies to be spread out for each case.

Looking at figure 51, the inclination cases have the left side of the graupel collecting smaller and larger droplets than the right side, but the right side has a slightly higher overall collision efficiency than the left. This is from the high pressure center being closer to the left side than the right. It keeps a constant push on higher momentum drops so that they cannot hit the side directly.

#### 4) Impact of the shape factor on the collision efficiency

Figure 52 shows the differences between the various graupel shapes used in the collision detection program. The graupel with a diameter of 3 mm and shape parameter of $\lambda = 1$ has collisions at the largest droplet size, because of the high velocity in the wind tunnel. The graupel with a diameter of 3.17 mm and shape parameter of $\lambda = 5$ case has a higher overall collision efficiency than the graupel with a diameter of 3.67 mm and shape parameter of $\lambda = 1$ case due to its more blunt shape. The droplets are more likely to get caught in that region.

## 4. Conclusions

In this study, we have performed simulation of the flow fields around falling conical graupel of diameter 0.5 to 5 mm by numerically solving the time-dependent Navier-Stokes equations. Both steady (D $<$ 2 mm) and unsteady flow cases (D $>$ 3 mm) are simulated. We have also simulated the flow fields around a graupel of 3.67 mm with apex shape factor $\lambda = 1$ and $\lambda = 5$ falling in an inclined manner with inclination angle changing from 0° to 45°. All

simulated flow fields appear to be reasonable. Even though the results cannot be compared directly with experimental data as the latter are not yet available, they do compare reasonably well with the results for flow past other shapes, such spheres, in the similar Reynolds number range, in drag coefficient and eddy shedding behavior. The change characteristics of the flow fields for different cases can be explained by basic physical principles. We believe this is the first time the flow fields past conical graupel over a complete size spectrum are presented.

We have also used these flow fields to determine the collision efficiencies with which conical graupel collide with supercooled cloud droplets by numerically solving the equation of motion of the droplet in the vicinity of the falling graupel. Such efficiencies play a central role on the riming growth of graupel to hail. A complete set of data of such efficiencies for graupel diameter 0.5 to 5 mm and drop radius 0 to $\sim$200 µm are generated and the properties of the results are explained based on physical principles.

The collected particles investigated in the present study are assumed to be spherical as they are all small cloud droplets. In the next phase of study, we plan to study the collision between conical graupel and non-spherical ice crystals, which will be a much more challenging problem, as the response of the ice crystal to an external flow field involves complicated motions. But from the experience gained in the present study, we feel that it is possible to simulate such complicated motions if adequate computing resources can be secured.

# APPENDIX

## Drag Force Correction

The collision detection program produced believable results for the first several model runs. However, when a droplet radius became larger than 100 µm, it would accelerate much faster with gravity than the smaller droplets. We created another program that would place droplets into an infinite outer boundary of uniform flow in the Z-direction. The program was able to iteratively determine the droplet's terminal velocity based on the superposition scheme described previously. We found that a large amount of error occurred when the droplet was 100 µm and larger. The drag force, $F_d$, was not strong enough to counteract the gravity force, $F_g$. In order to fix this issue, we had to rewrite the drag force equation. We could no longer assume that the droplets fell in the Stokes regime (Pruppacher and Klett 1997) where

$$\frac{C_D N_{\mathrm{Re}}}{24} \neq 1 \tag{A1}$$

This changed the drag force equation to

$$F_d = 6\pi n_a r_d \frac{C_D N_{\mathrm{Re}}}{24} \frac{u - v_d}{C_{sc}} \tag{A2}$$

with

$$C_D = \frac{4(\rho_w - \rho_a) g 2 r_d}{3 \rho_a V_\infty^2} \tag{A3}$$

After testing the new equation, we found that the drag force still had 25 % error. By multiplying the drag force by $\frac{3}{4}$, our program was able to get terminal velocity results with an error less than 0.1 %. With this result, we could run the collision detection program for all large droplet sizes.

# REFERENCES


Beard, 1976: Need all of this. *J. Atmos. Sci.*, **66**, 2359–2366.

Blohn, N. V., K. Diehl, and S. K. Mitra, 2009: Riming of graupel: wind tunnel investigations of collection kernels and growth regimes. *J. Atmos. Sci.*, **66**, 2359–2366.

Davies, C. N., 1945: Definitive equations for the fluid resistance of spheres. *Proc. Phys. Soc.*, **57**, 259–270.

Dorsch, R. G. and P. T. Hacker, 1951: Experimental values of the surface tension of supercooled water. National Advisory Committee for Aeronautics Tech. Note NACA TN 2510, Lewis Flight Propulsion Laboratory, 21 pp.

Dyke, M. V., 1979: *An Album of Fluid Motion*. 1st ed., The Parabolic Press, 176 pp.

Garner, F. H. and D. A. Lihou, 1965: Mass transfer to and from drops in gaseous streams. *DECHEM A Monogr.*, **55**, 155–178.

Gittens, G. J., 1969: Variation of surface tension of water with temperature. *J. Colloid and Interface Sci.*, **30**, 406–412.

Hashino, T. ., M. Chiruta, and P. K. Wang, 2010: A numerical study on the riming process in the transition from a pristine crystal to a graupel particle. *13th Conference on Cloud Physics*, Portland, Oregon, American Meteorological Society, 1.86.

Jayaweera, K. O. L. F. and B. J. Mason, 1965: The behavior of freely falling cylinders and cones in a viscous fluid. *J. Fluid Mech.*, **22**, 709720.

Ji, W. and P. K. Wang, 1998: On the ventilation coefficients of falling ice crystals at low-intermediate reynolds numbers. *J. Atmos. Sci.*, **56**, 829836.

Knight, C. A. and N. Knight, 1973: Conical graupel. *J. Atmos. Sci.*, **30**, 118124.

List and Schemenauer, 1971: Free-fall behavior of planar snow crystals, conical graupel and small hail. *J. Atmos. Sci.*, **28**, 110115.

Locatelli, J. D. and P. V. Hobbs, 1974: Fall speeds and masses of slid precipitation particles. *J. Geophys. Res.*, **79**, 21852197.

Massey, B. S., 1979: *Mechanics of Fluids*. 4th ed., Van Nostrand Reinhold, 543 pp.

Miller, N. L. and P. K. Wang, 1989: Theoretical determination of the efficiency of aerosol particle collection by falling columnar ice crystals. *J. Atmos. Sci.*, **46**, 16561663.

Pflaum, J. C., J. J. Martin, and H. Pruppacher, 1978: A wind tunnel investigation of the hydrodynamic behavior of growing, free falling graupel. *Q. J. R. Meteorol. Soc.*, **104**, 179187.

Pruppacher, H. and Pitter, 1997: Need al of this. *Q. J. R. Meteorol. Soc.*, **104**, 179187.

Pruppacher, H. R. and J. D. Klett, 1997: *Microphysics of Clouds and Precipitation*. 2d ed., D. Reidel, New York, 954 pp.

Wang, P. K., 1982: Mathematical description of the shape of conical hydrometeors. *J. Atmos. Sci.*, **39**, 26152622.

Wang, P. K., 1983: On the definition of collision efficiency of atmospheric particles. *J. Atmos. Sci.*, **40**, 10511052.

Wang, P. K. and H. R. Pruppacher, 1977: Acceleration to terminal velocity of cloud and raindrops. *J. App. Meteorol.*, **16**, 275280.

# List of Tables

TABLE 1. This is a list of the different sizes and shapes of graupel used in the flow field and collision detection simulations.

| $D$(mm) | $\lambda$ | $a$(mm) | $c$(mm) | ratio | $u_\infty$(m/s) |
|---|---|---|---|---|---|
| 0.5 | 1 | 0.137 | 0.229 | 11/12 | 0.72 |
| 1.0 | 1 | 0.275 | 0.458 | 11/12 | 1.20 |
| 2.0 | 1 | 0.550 | 0.916 | 11/12 | 1.99 |
| 3.0 | 1 | 0.824 | 1.374 | 11/12 | 2.67 |
| 3.67 | 1 | 1.000 | 1.500 | 0.829 | 2.50 |
| 3.17 | 5 | 1.000 | 1.500 | 0.829 | 2.50 |
| 4.0 | 1 | 1.099 | 1.832 | 11/12 | 3.29 |
| 5.0 | 1 | 1.373 | 2.290 | 11/12 | 3.88 |

# List of Figures

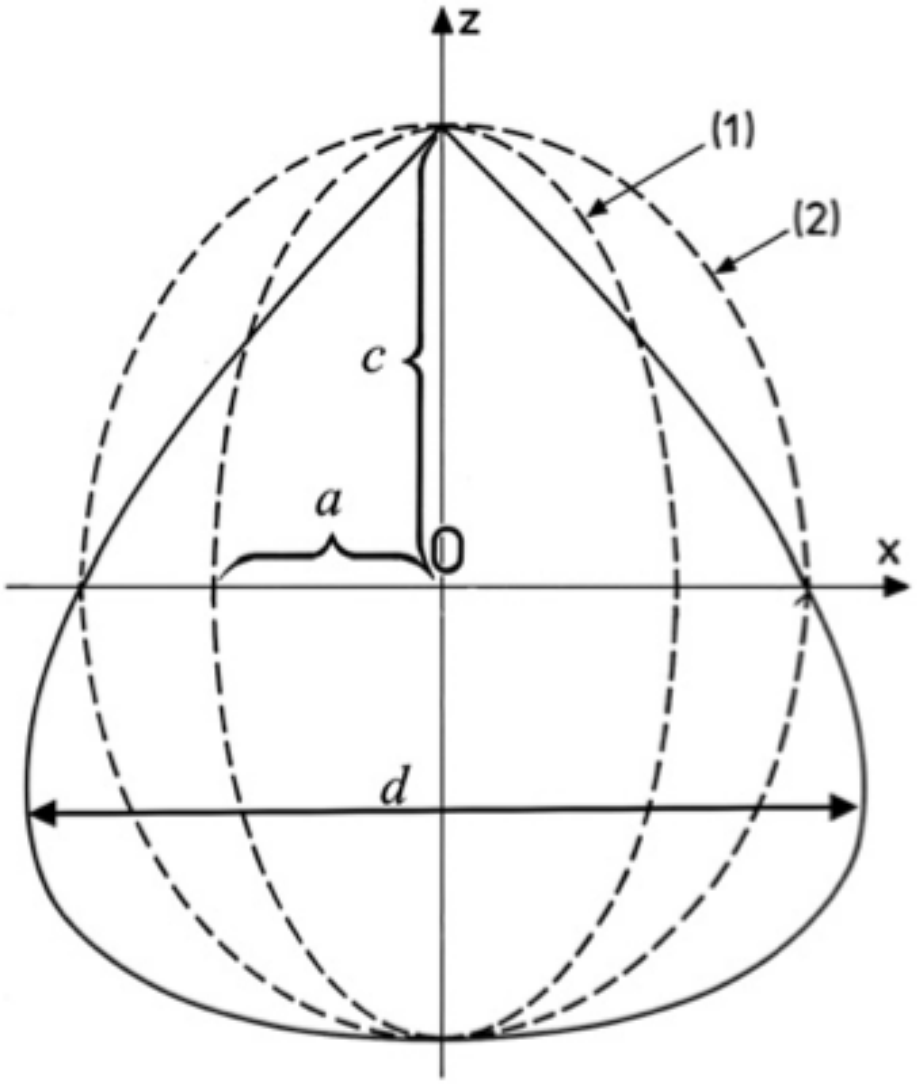


FIG. 1. Sketch of equation 1. Figure from Wang (1982).

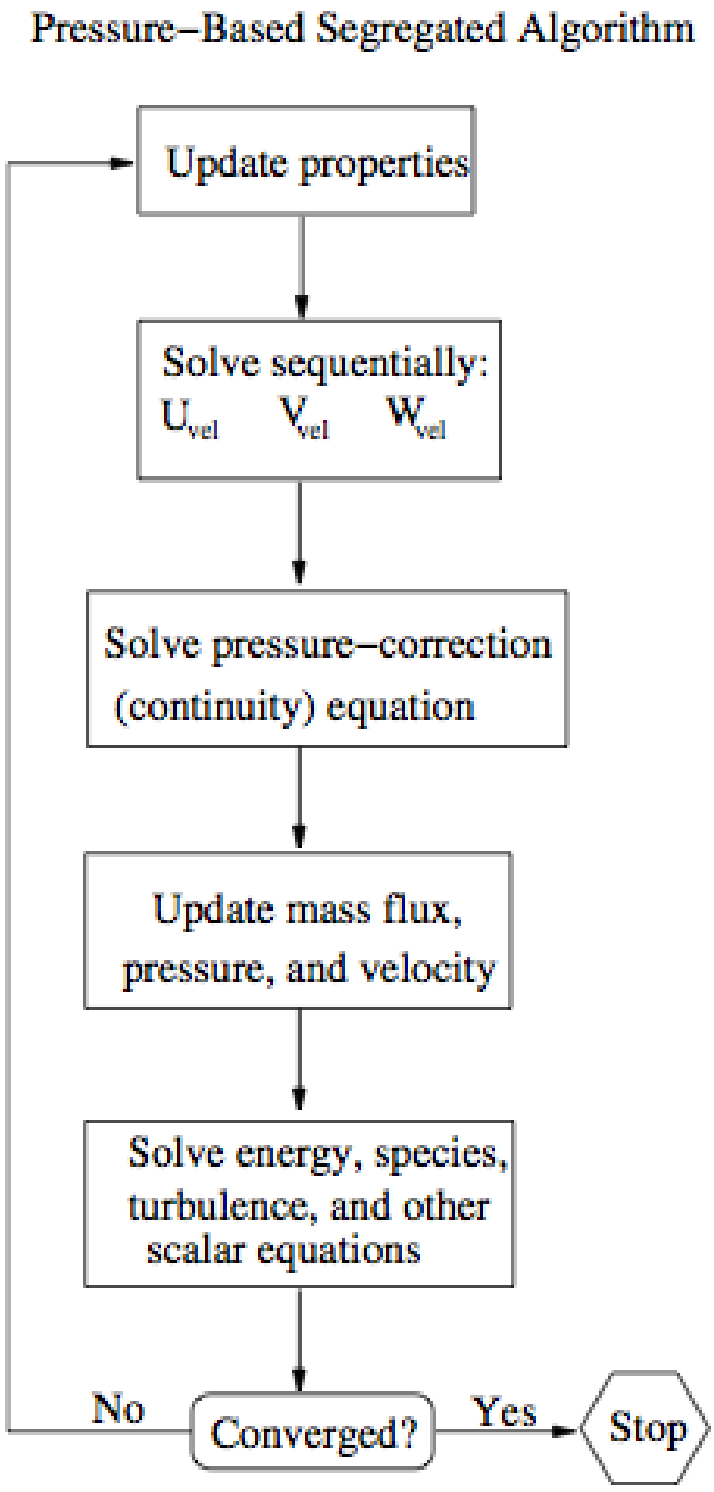


FIG. 2. Flow chart for the FLUENT pressure solver algorithm. (FLUENT 12.1 Theory Guide).

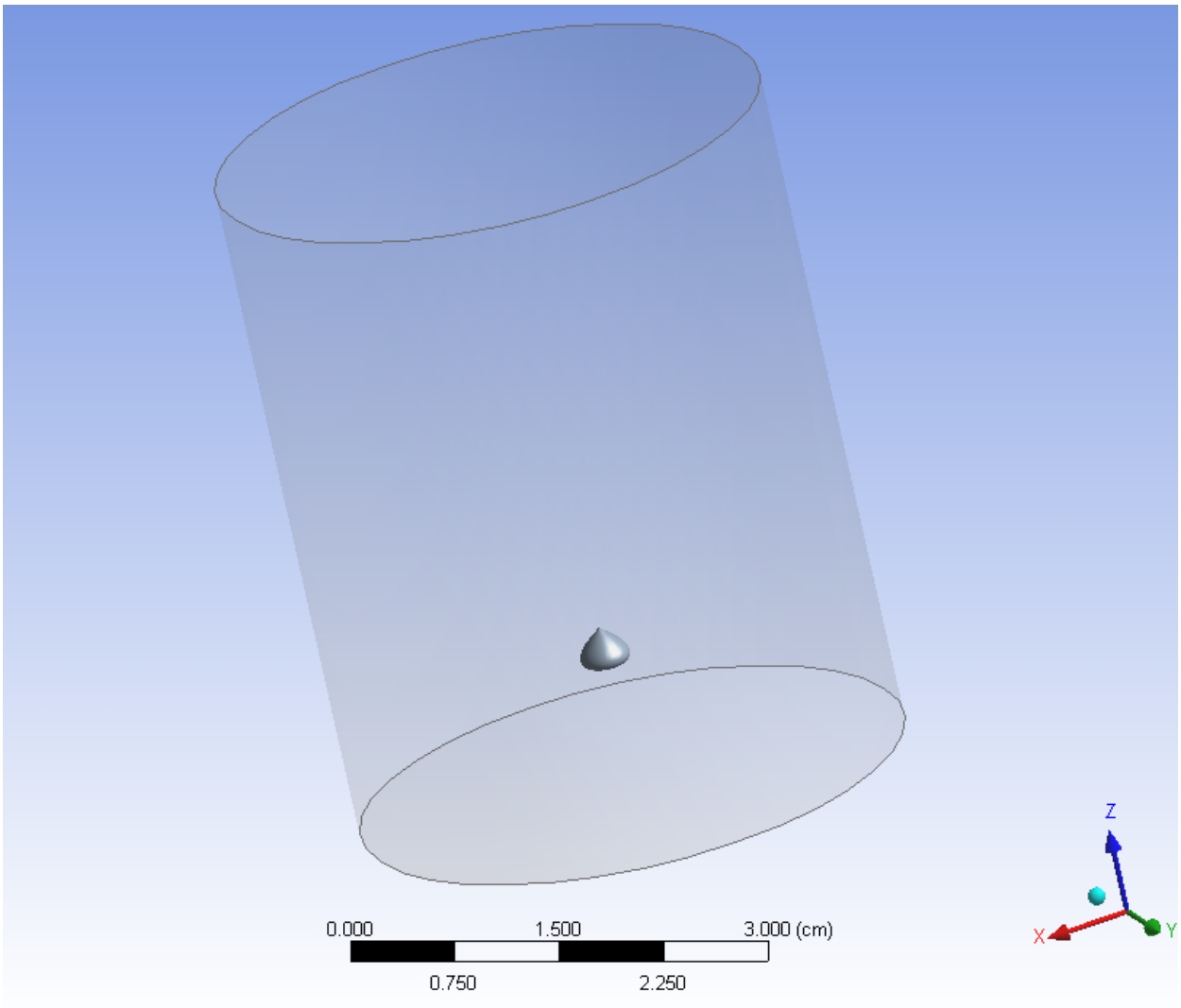


FIG. 3. Screenshot from the ANSYS modeling software, showing a 3-D model of the graupel (solid) in the middle of the outer boundary (transparent).

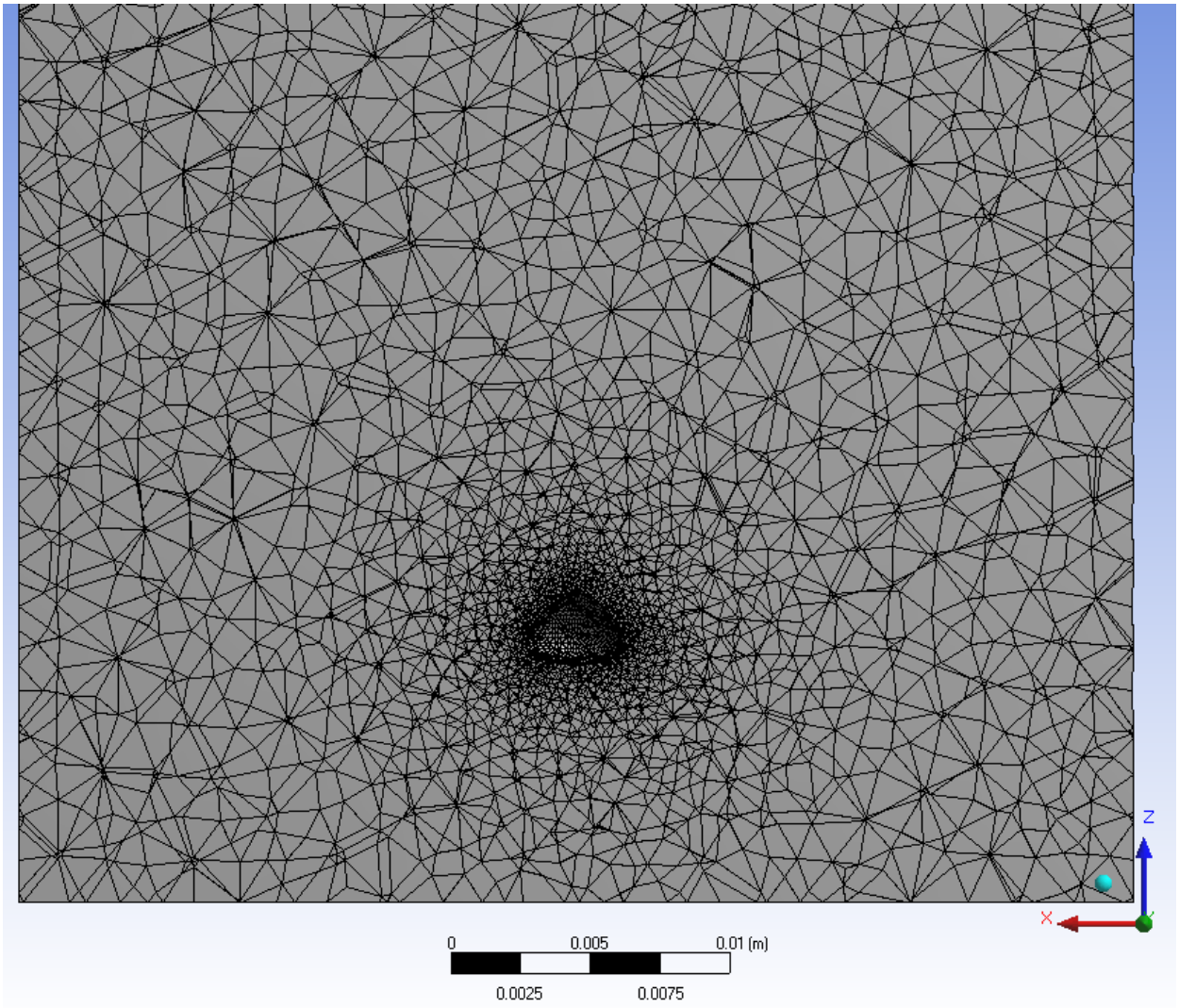


FIG. 4. Screenshot from the ANSYS meshing software. This is a slice through the x-axis at $x = 0$. Notice that the mesh is finer towards the graupel and is coarse further away from the graupel.

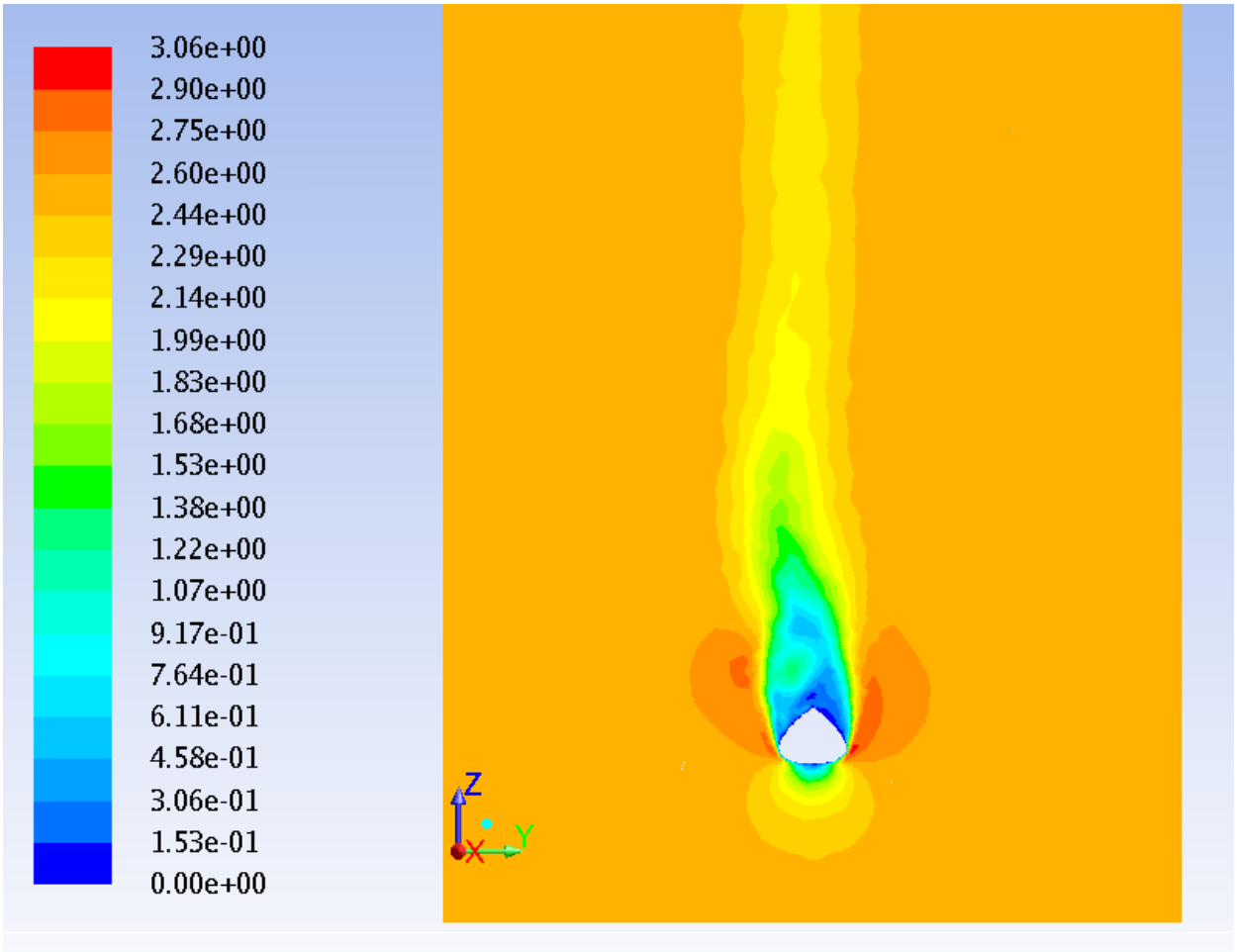


FIG. 5. Screenshot from the FLUENT software. This is a slice through the y-axis at $y = 0$, showing velocity magnitude in m/s. An example of the unsteady flow created after the steady state is solved.

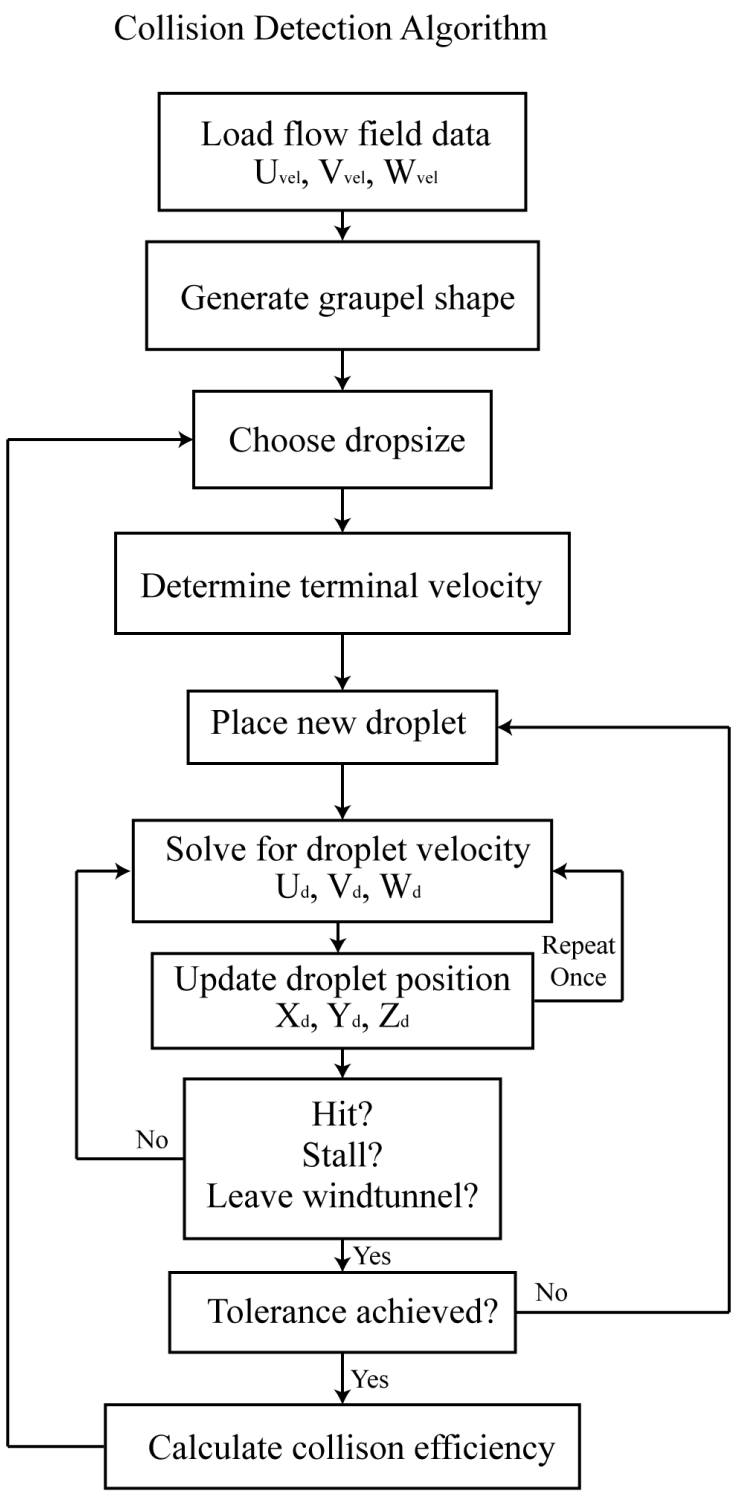


FIG. 6. Flow chart of the collision detection program.

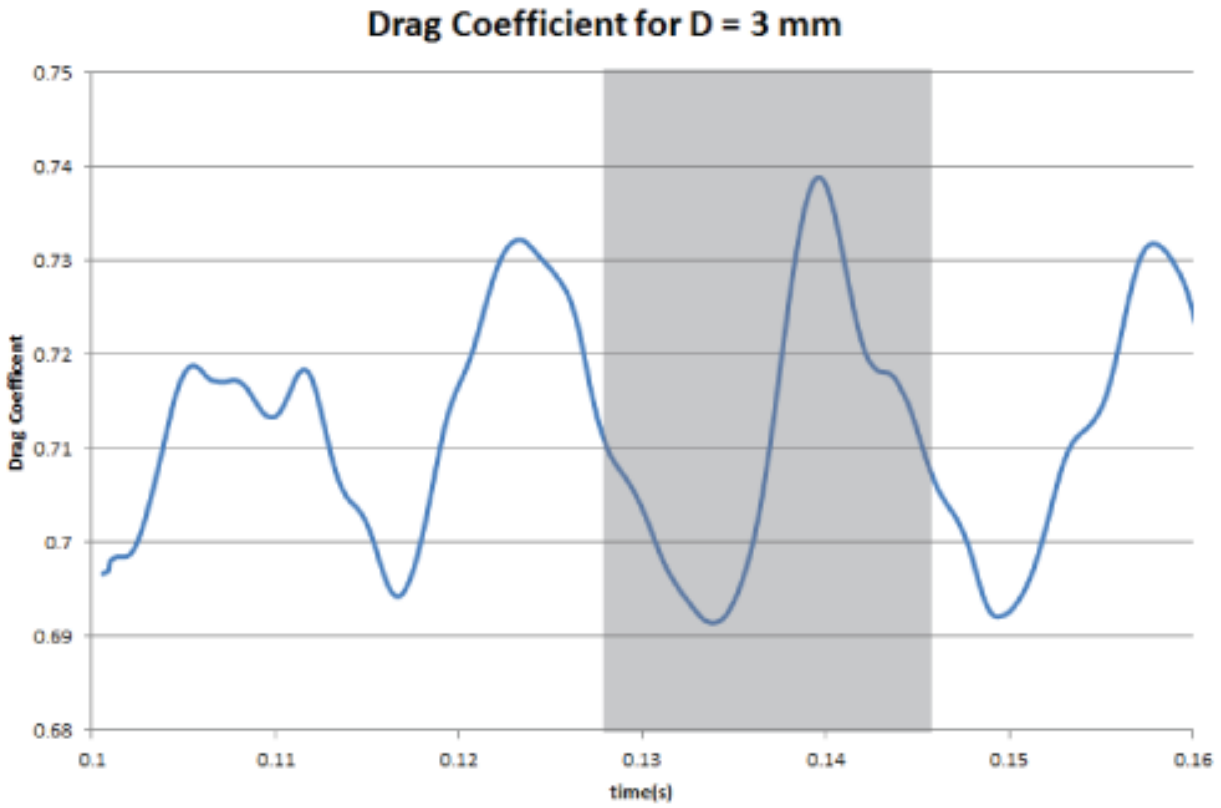


FIG. 7. Drag coefficient for graupel with a size of 3 mm and $\lambda = 1$ shape. The gray area represents which time steps were chosen for the simulation loop.

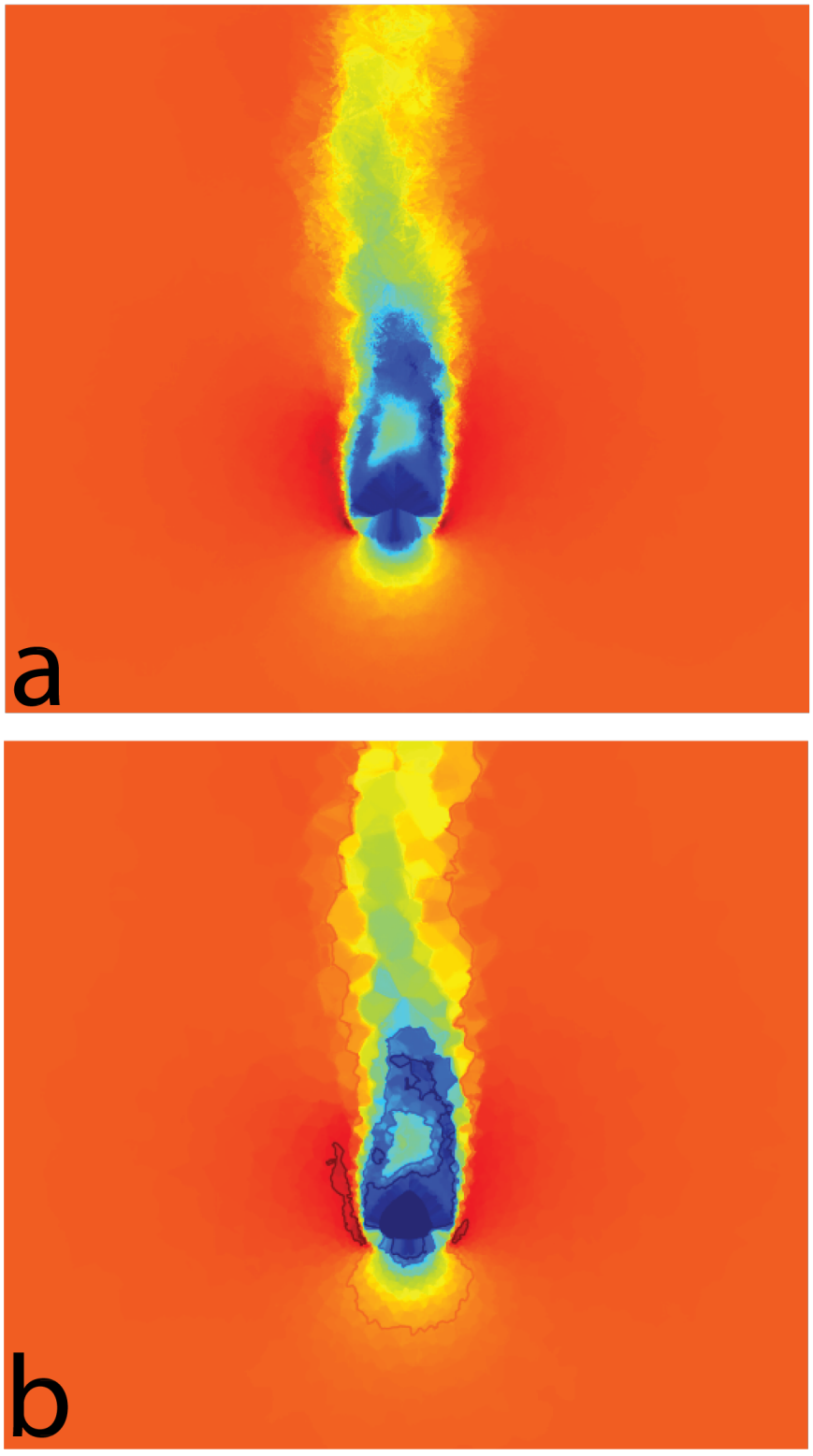


FIG. 8. The flow field z-velocity of a slice along the y-axis. (a) Uses straight averaging (b) Uses Shephard's method. The mesh and values of the flow field are better represented when using Shephard's method. This can be seen with the mesh-like appearance of (b)

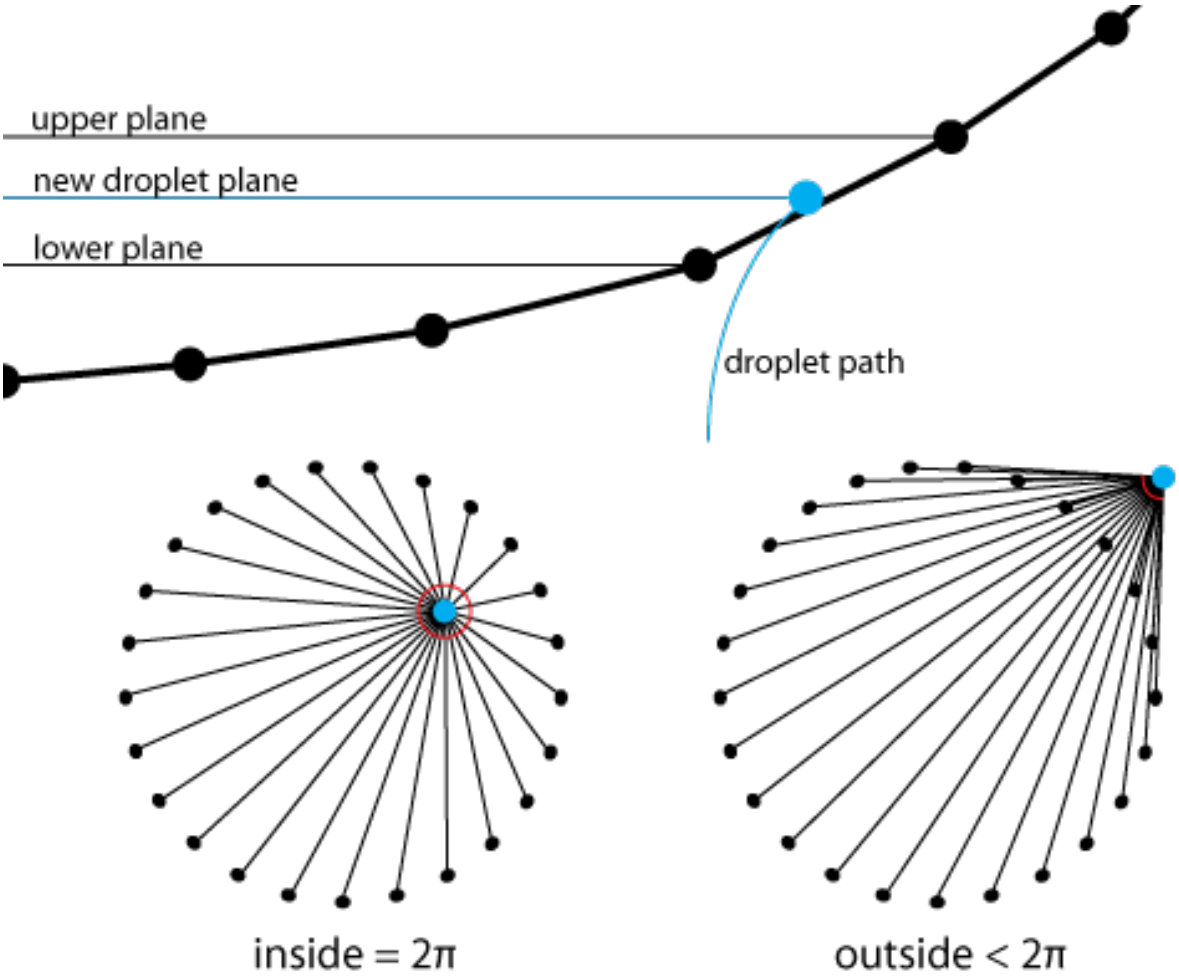


FIG. 9. Graphical representation of the point in polygon process. The top image shows how the program generates a new 2-D slice based on the droplet's position and the neighboring points. The bottom two images show how the it determines if the droplet is inside.

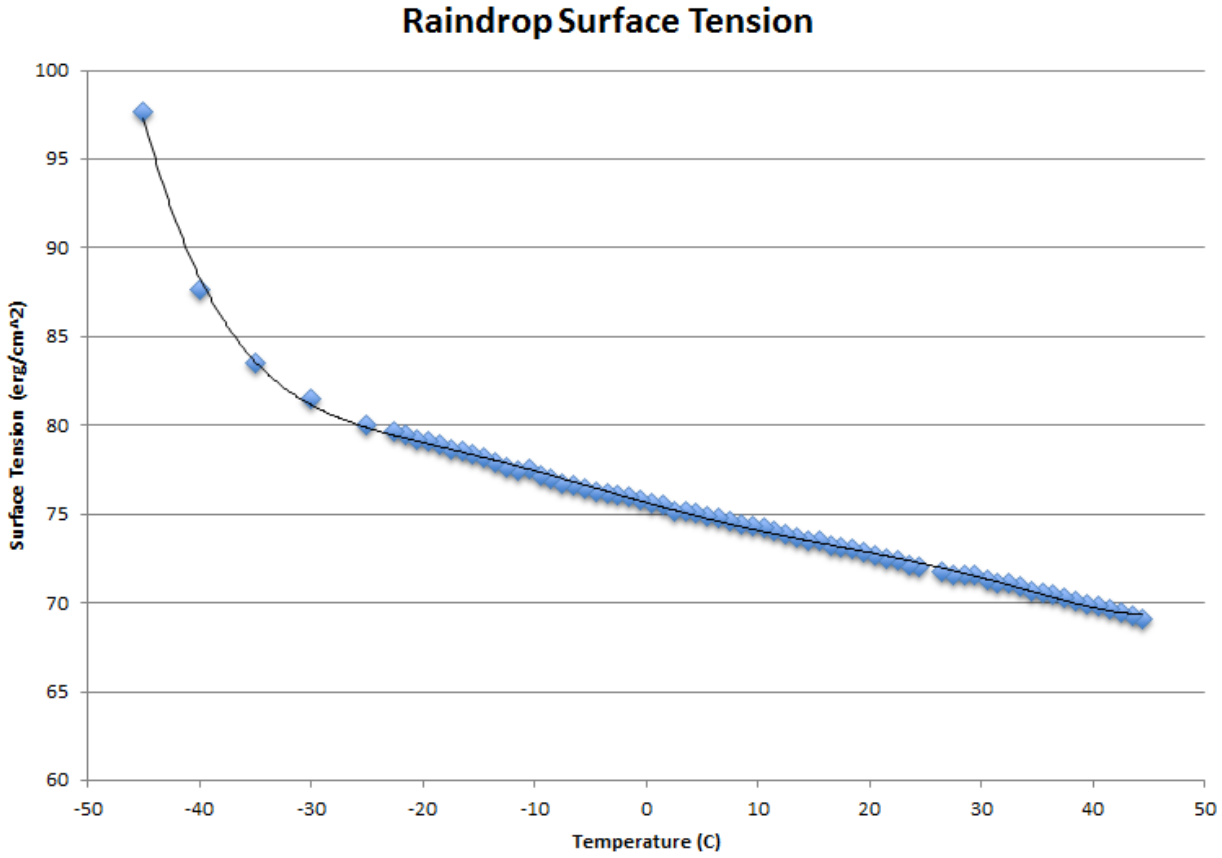


FIG. 10. Plot of surface tension values from -20 to 40 °C (Dorsch and Hacker 1951) and values from -45 to −20 °C (Gittens 1969). We can fit a polynomial curve to this data and find the coefficients for equation 24.

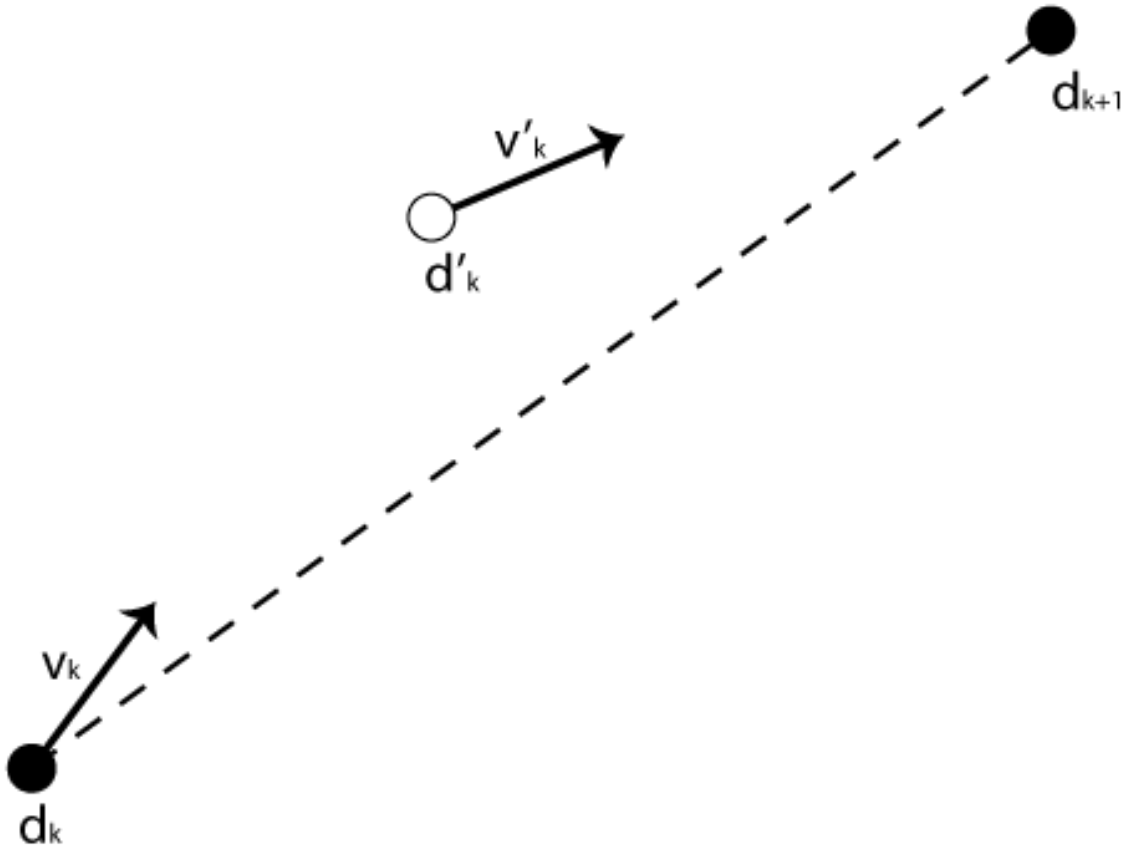


FIG. 11. An example of the two steps calculated in the second-order Runge-Kutta method.

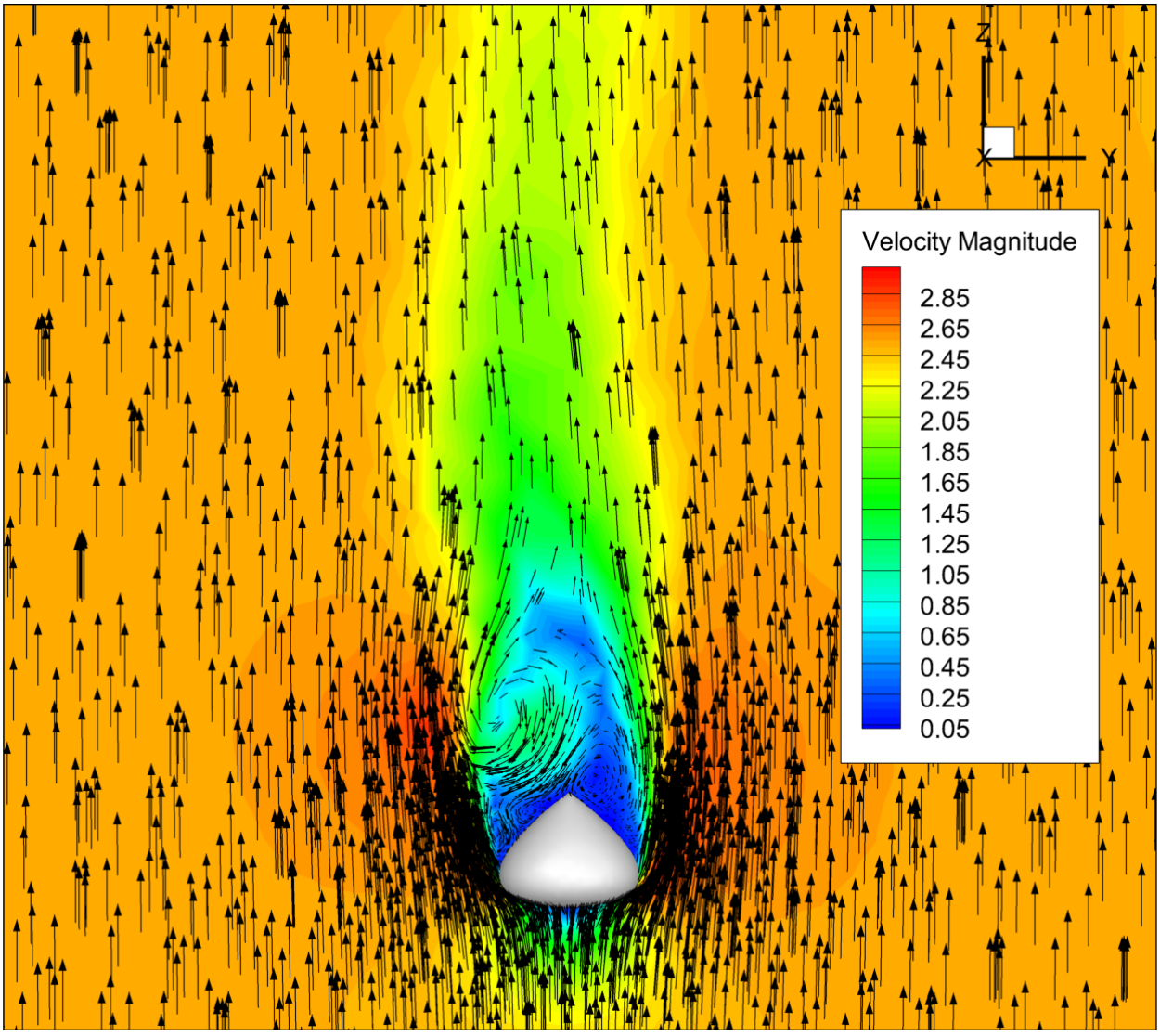


FIG. 12. Uninclined graupel with velocity vectors and velocity magnitude contours in m/s.

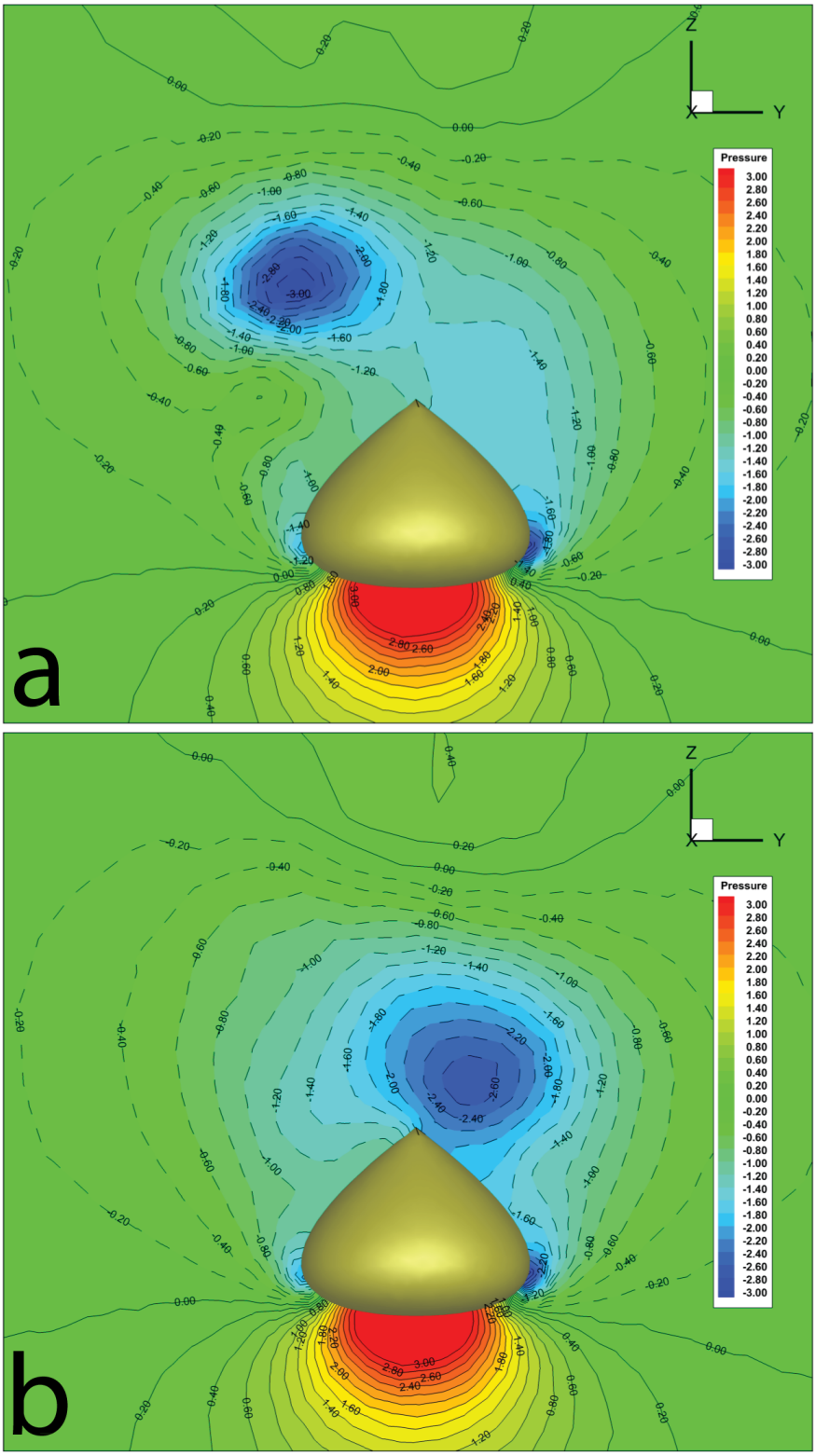


FIG. 13. Two randomly chosen frames of the computed pressure distributions around a falling graupel with no inclination of shape $\lambda = 1$. The negative contours are dashed. The pressure is unit Pa.

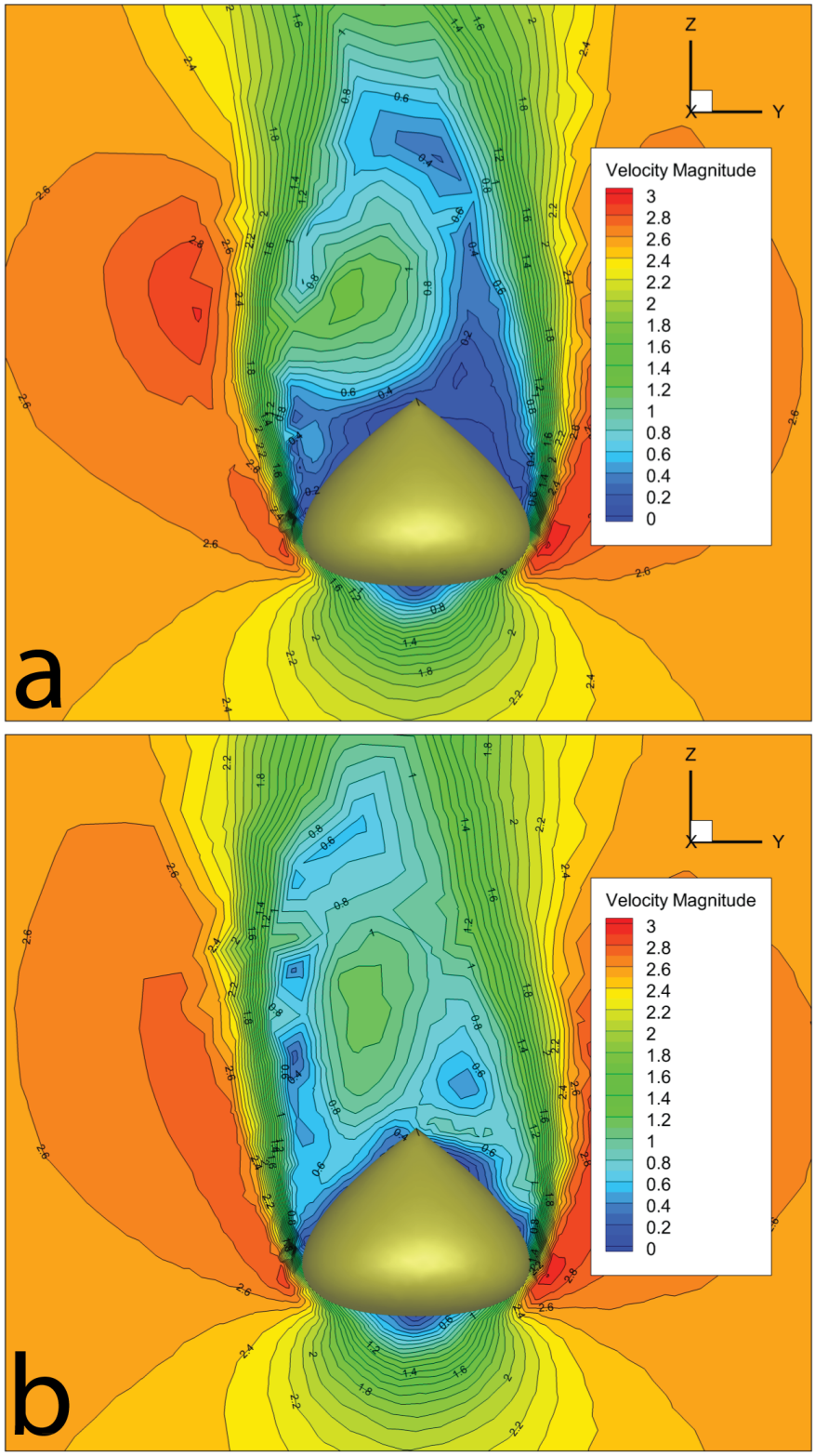


FIG. 14. Two randomly chosen frames of the computed velocity magnitude around a falling graupel with no inclination of shape $\lambda = 1$. The velocity is unit m/s.

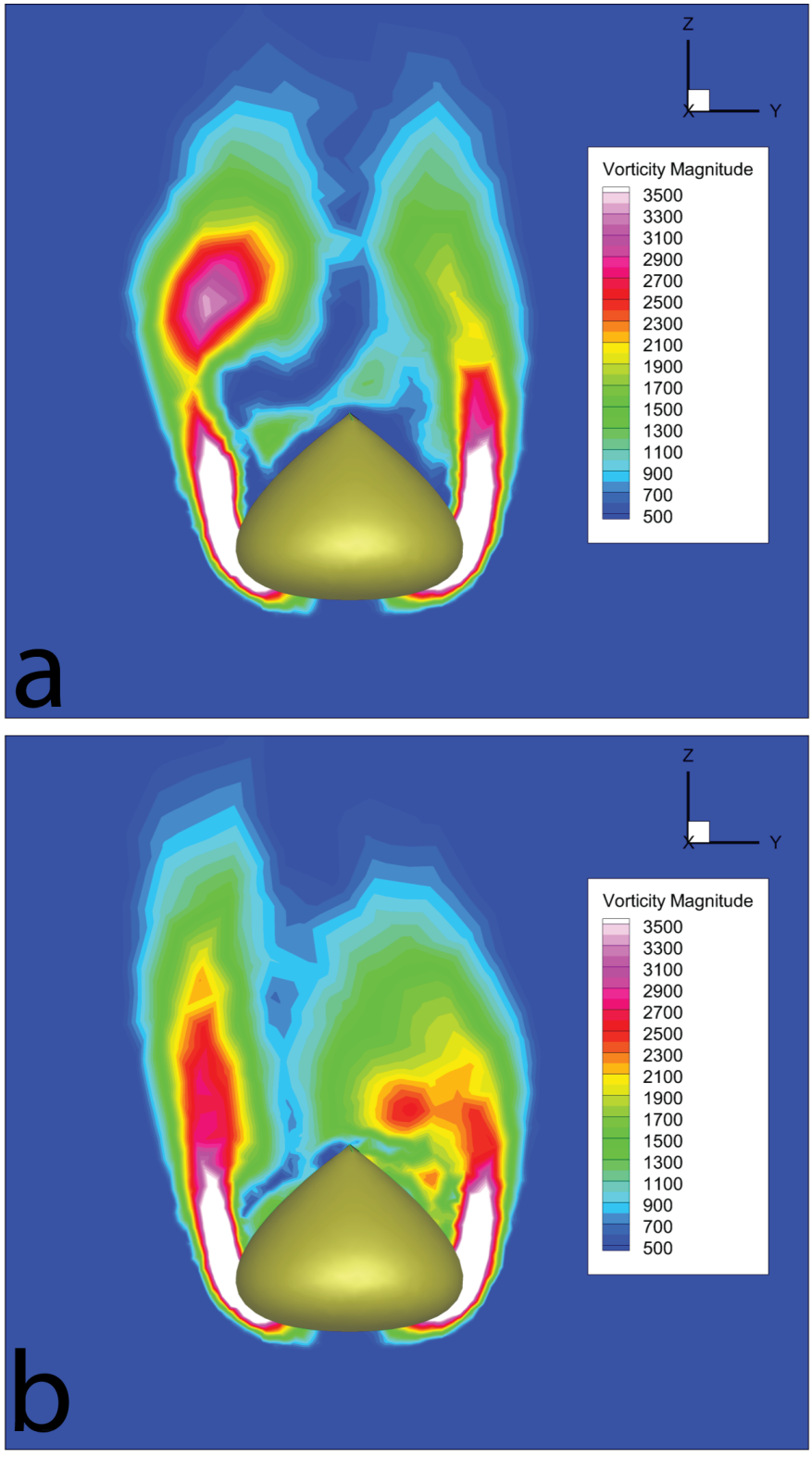


FIG. 15. Two randomly chosen frames of the computed vorticity magnitude around a falling graupel with no inclination of shape $\lambda = 1$. The velocity is unit 1/s.

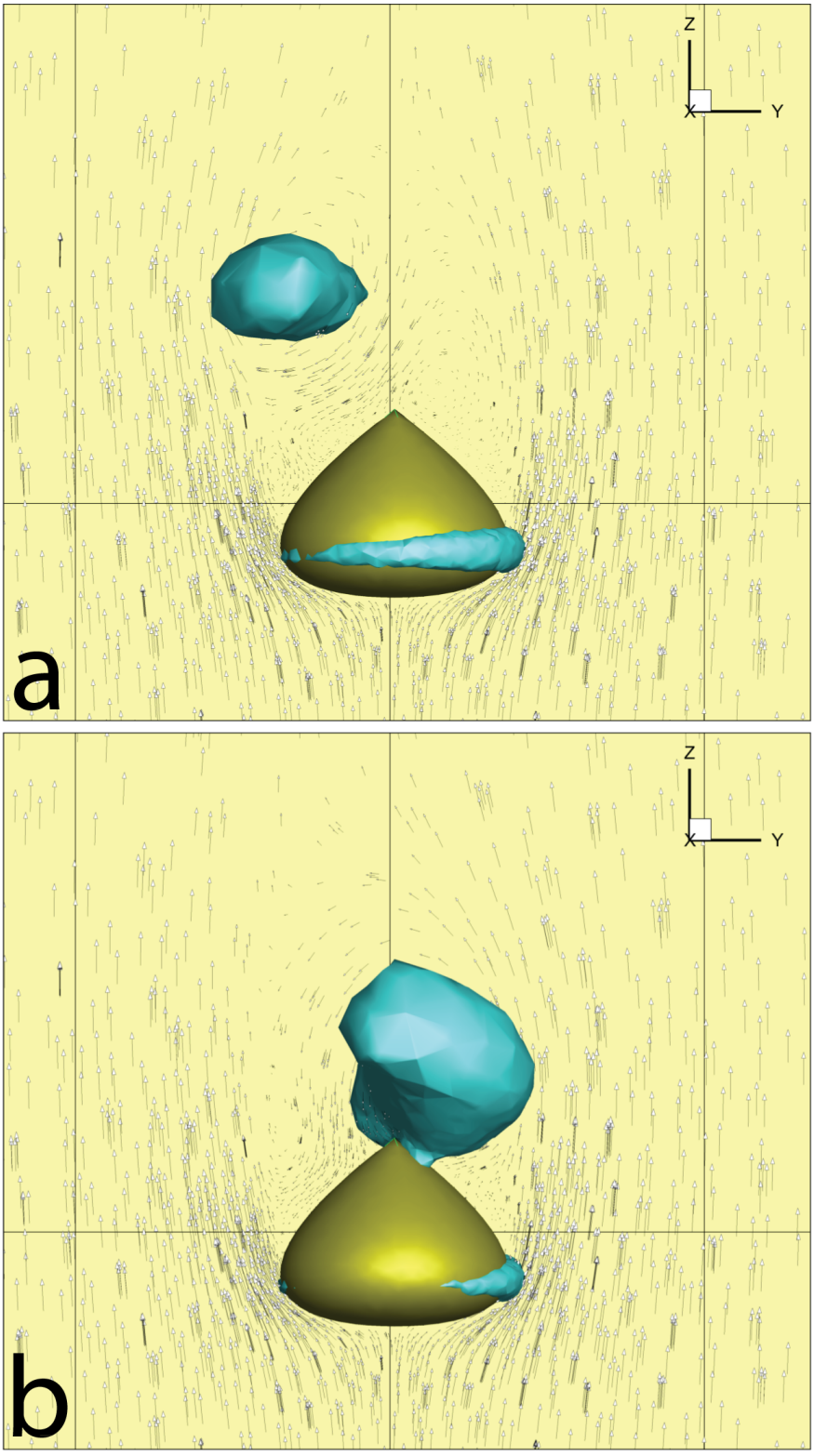


FIG. 16. Two randomly chosen frames of the computed velocity magnitude shown as orthogonal vectors around a falling graupel with no inclination of shape $\lambda = 1$. The isosurface is a pressure of P = -2 Pa.

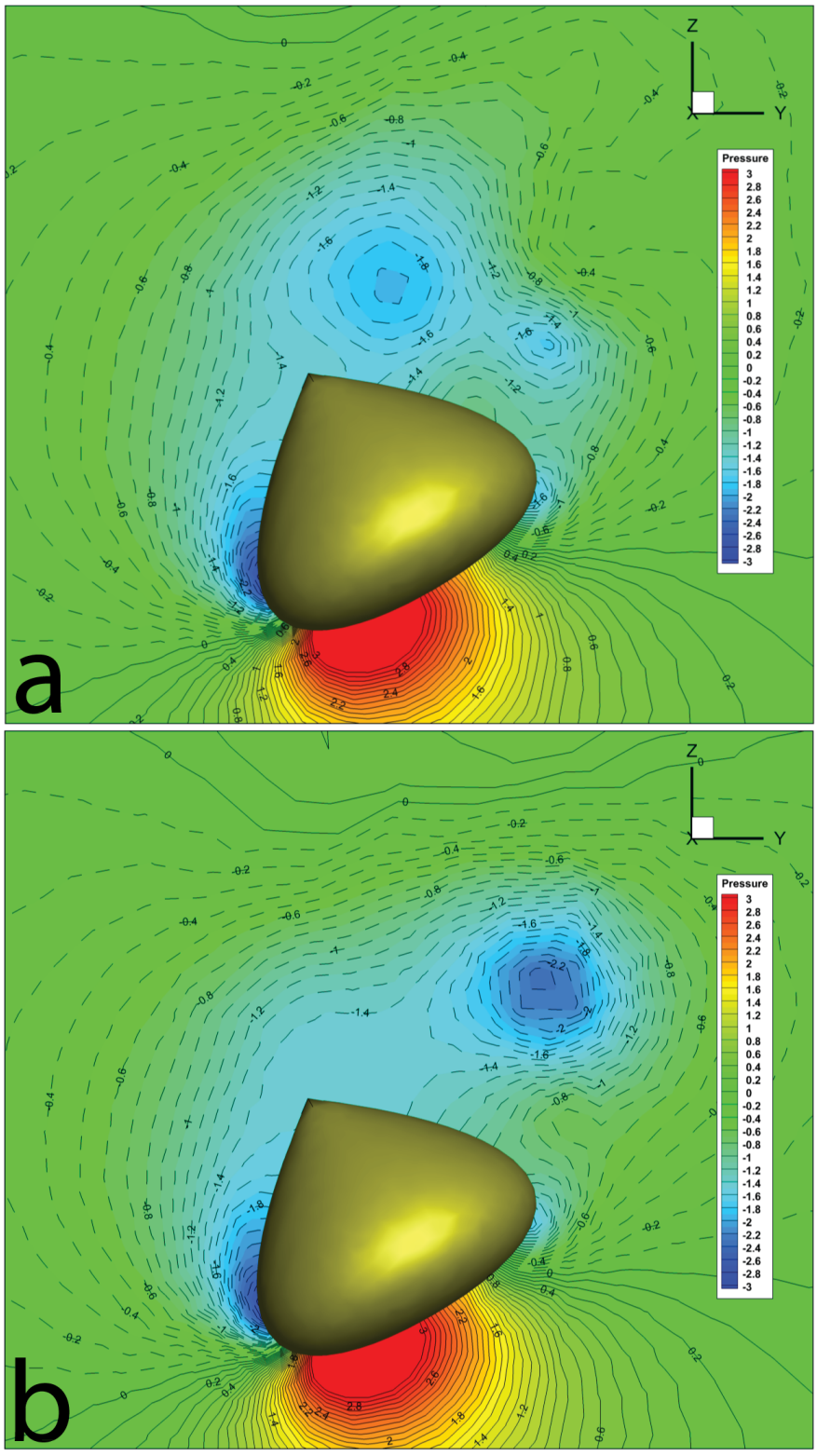


FIG. 17. Two randomly chosen frames of the computed pressure distributions around a falling graupel with an inclination of $\theta = 30$ with a shape of $\lambda = 1$. The negative contours are dashed. The pressure is unit Pa.

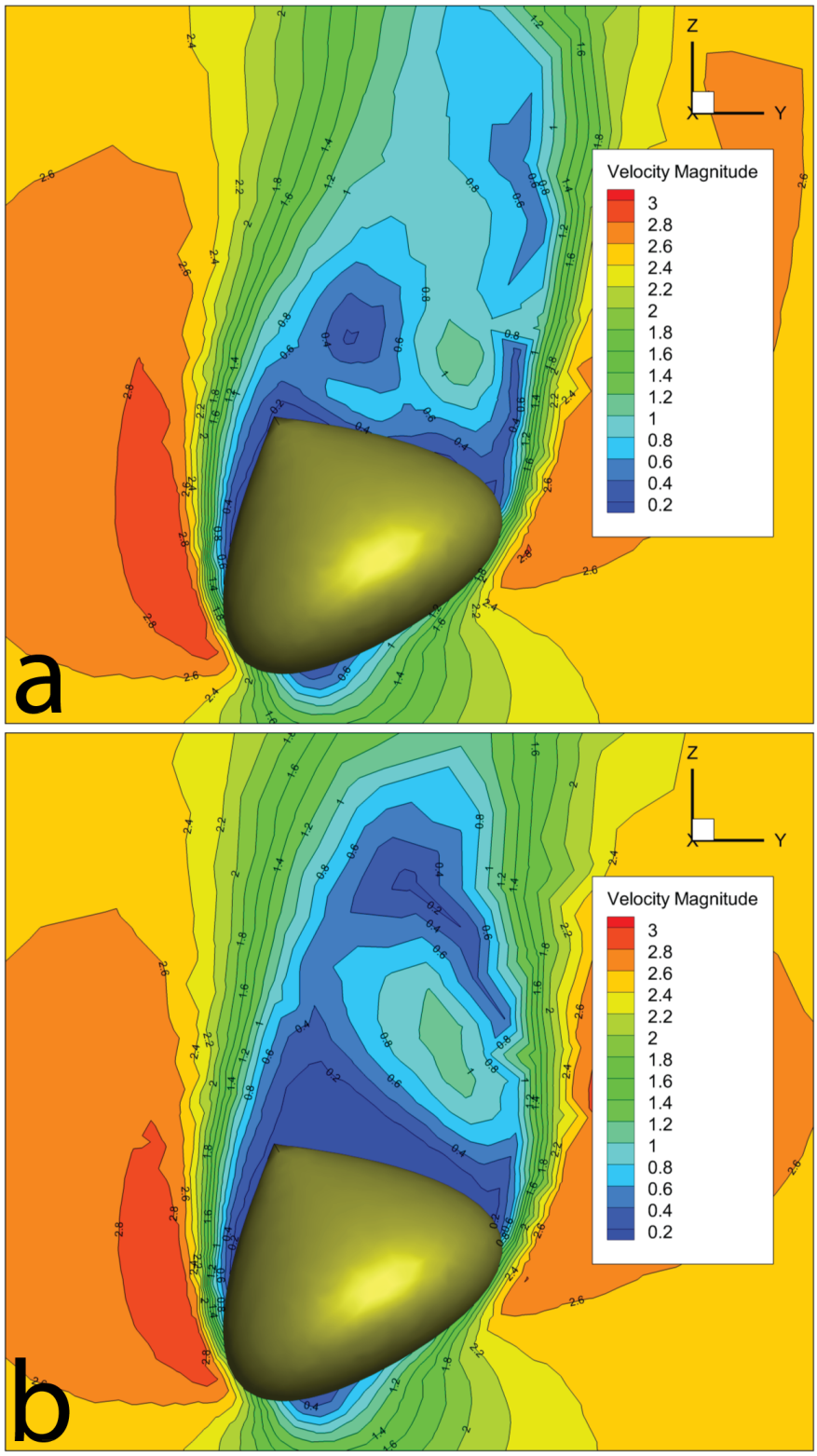


FIG. 18. Two randomly chosen frames of the computed velocity magnitude around a falling graupel with an inclination of $\theta = 30$ with a shape of $\lambda = 1$. The velocity is unit m/s.

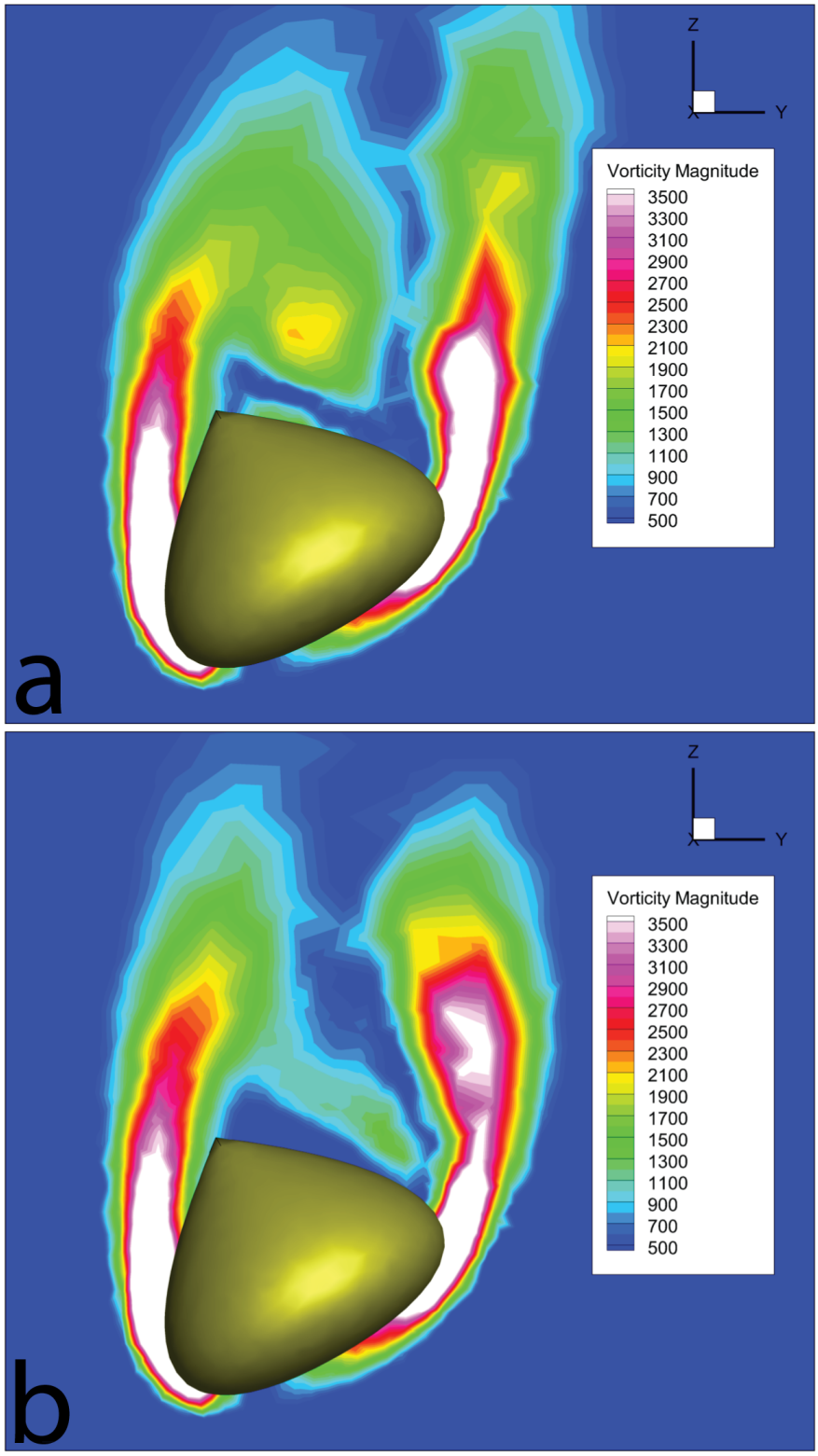


FIG. 19. Two randomly chosen frames of the computed vorticity magnitude around a falling graupel with an inclination of $\theta = 30$ with a shape of $\lambda = 1$. The velocity is unit 1/s.

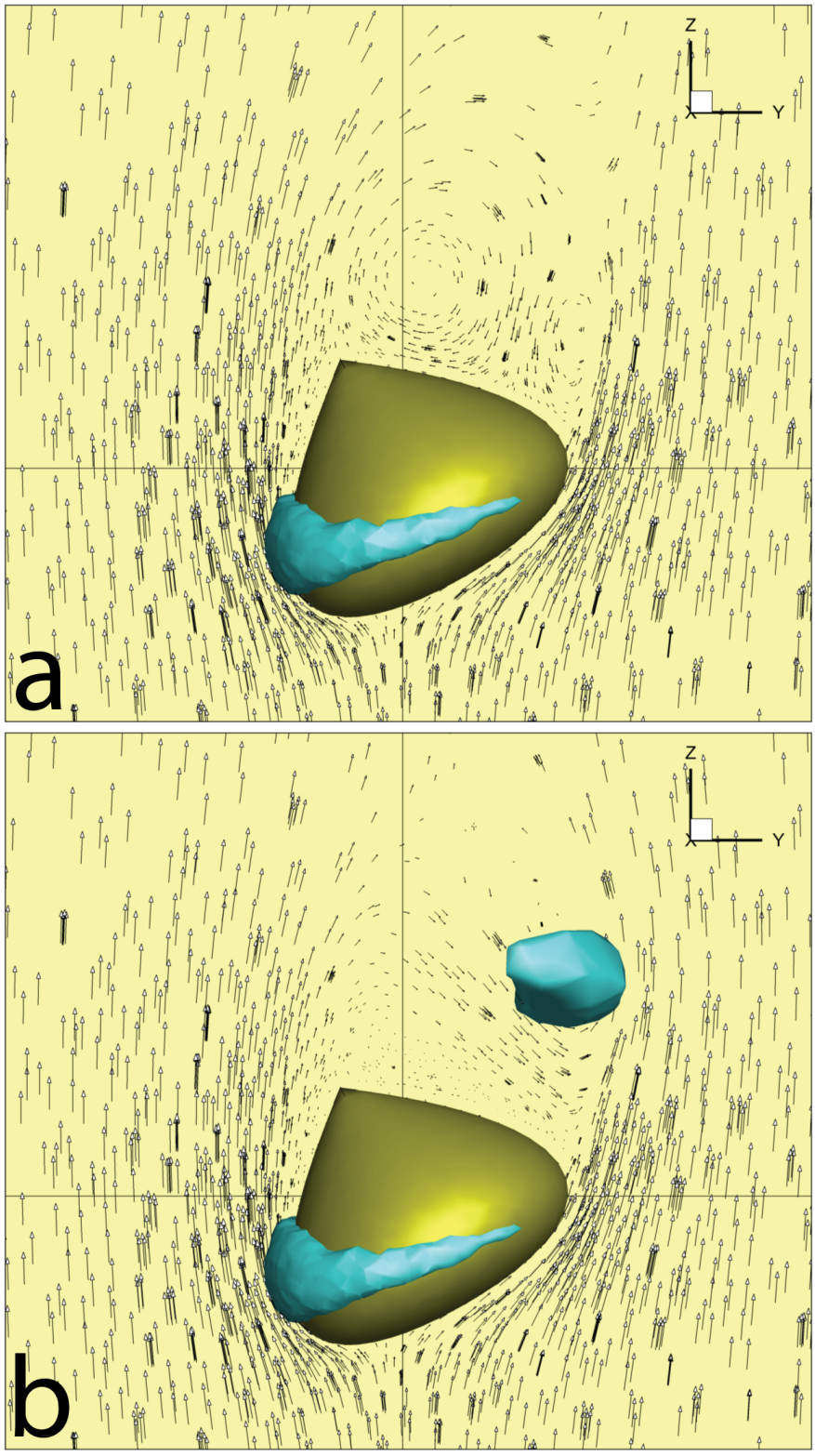


FIG. 20. Two randomly chosen frames of the computed velocity magnitude shown as orthogonal vectors around a falling graupel with an inclination of $\theta = 30$ with a shape of $\lambda = 1$. The isosurface is a pressure of P = -2 Pa.

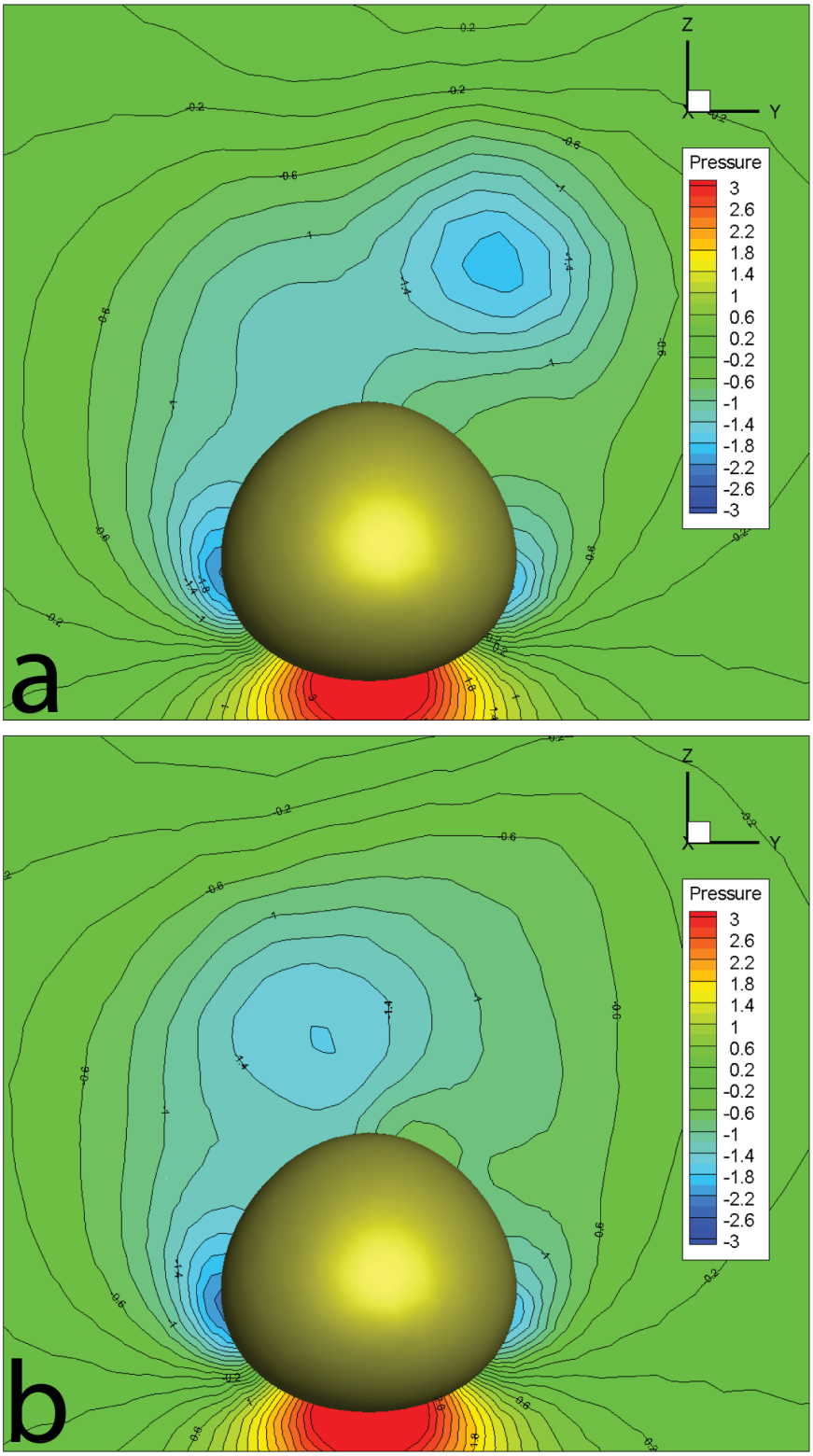


FIG. 21. Two randomly chosen frames of the computed pressure distributions around a falling graupel with a shape of $\lambda = 5$. The pressure is unit Pa.

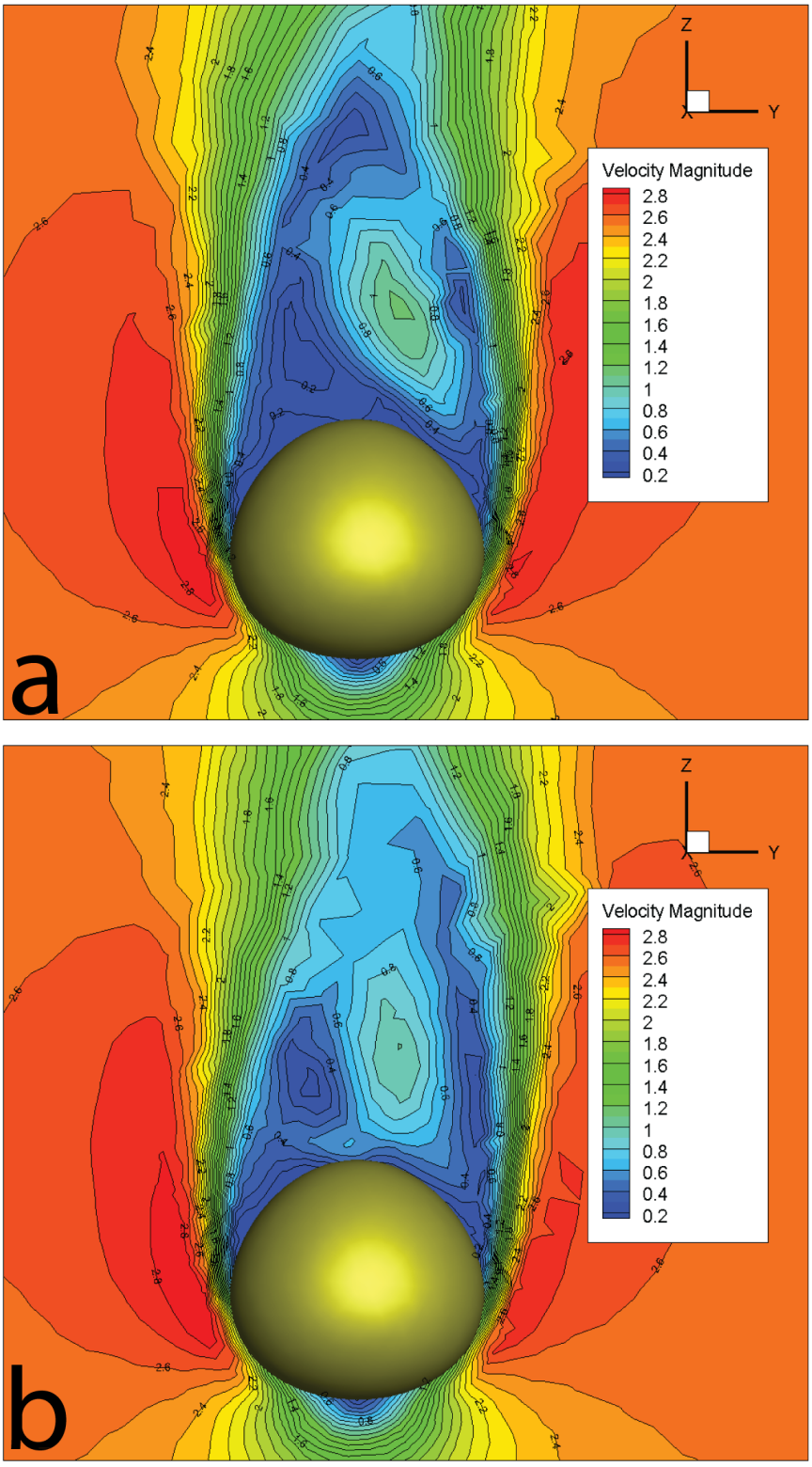


FIG. 22. Two randomly chosen frames of the computed velocity magnitude around a falling graupel with a shape of $\lambda = 5$. The velocity is unit m/s.

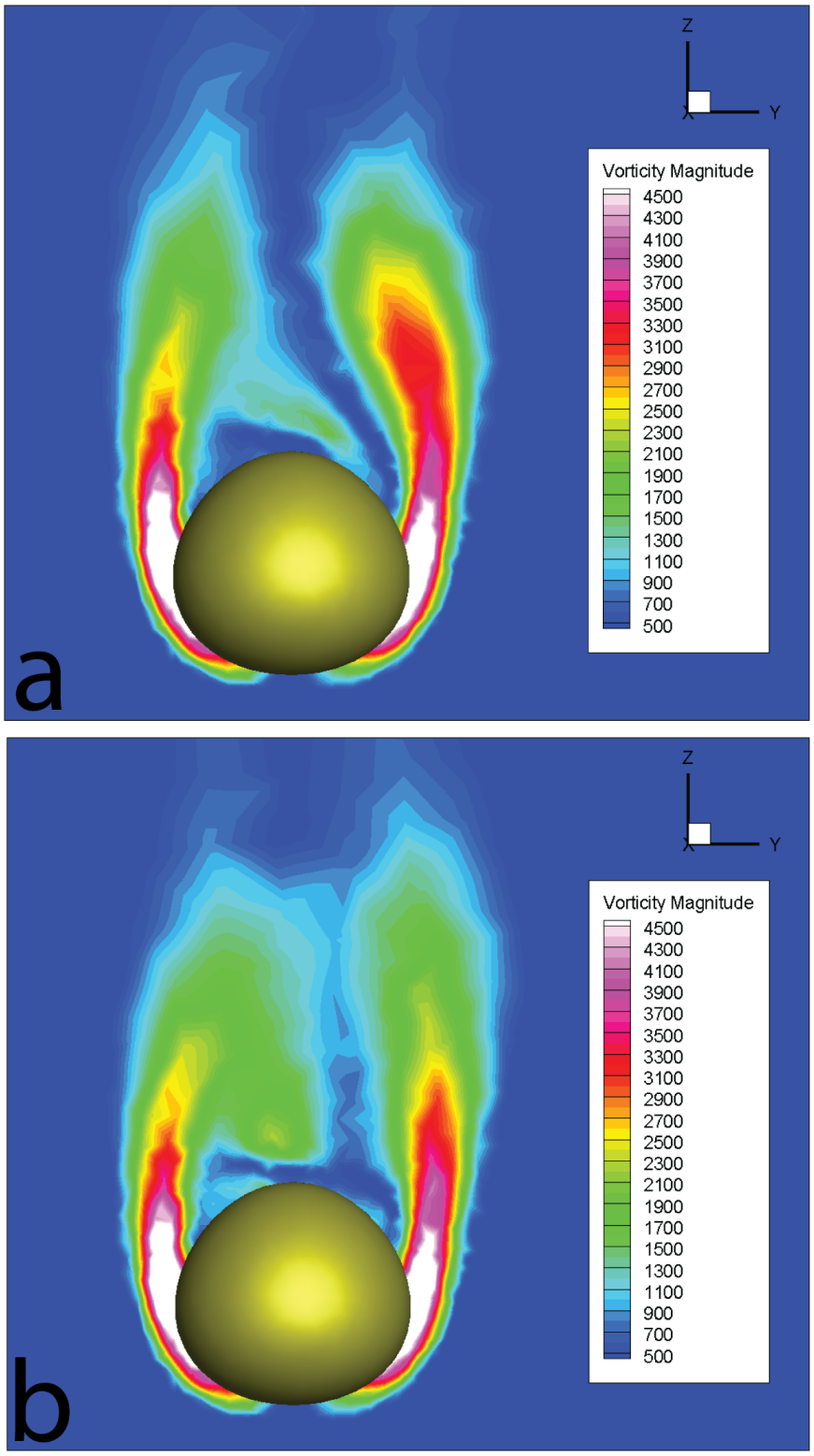


FIG. 23. Two randomly chosen frames of the computed vorticity magnitude around a falling graupel with a shape of $\lambda = 5$. The velocity is unit 1/s.

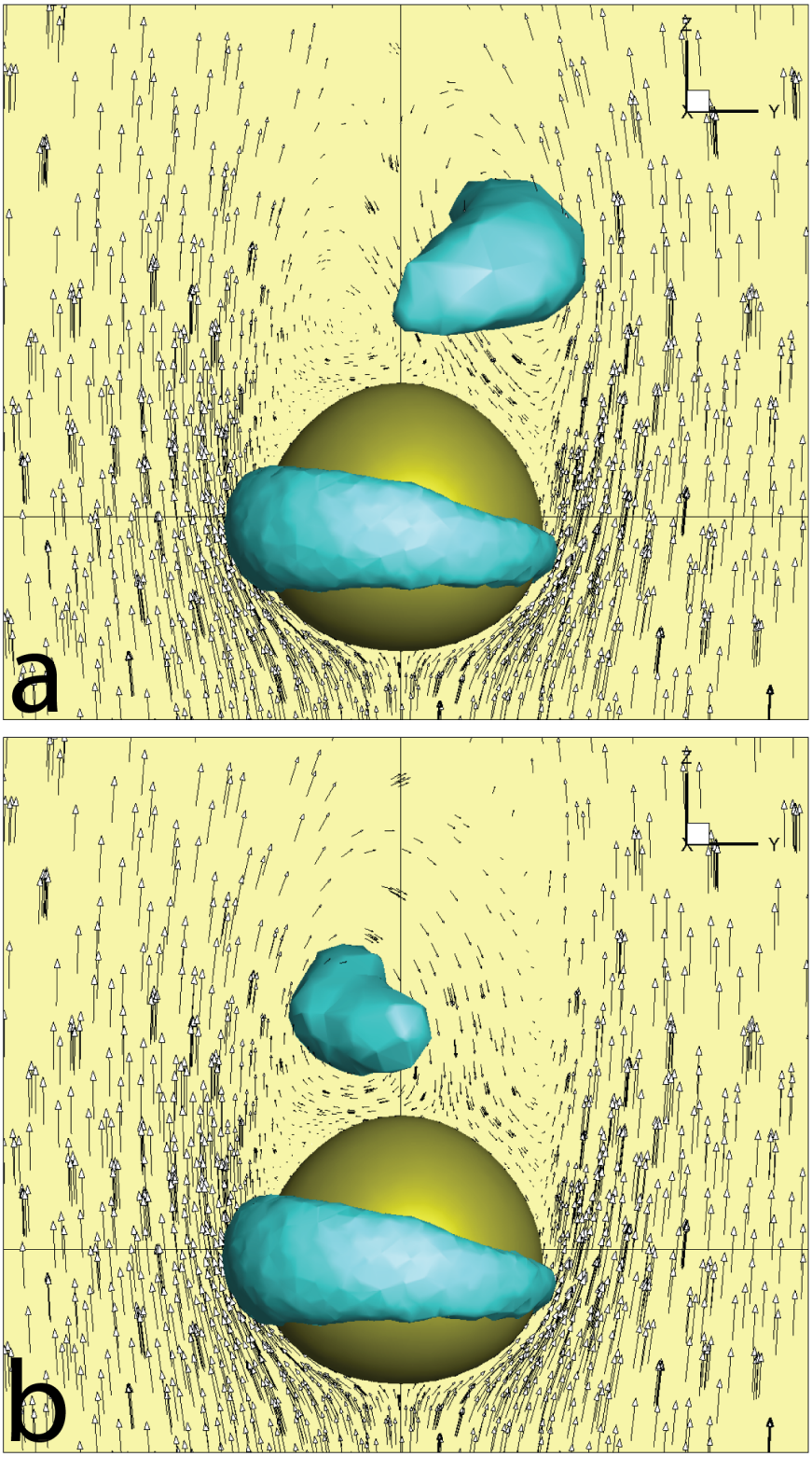


FIG. 24. Two randomly chosen frames of the computed velocity magnitude shown as orthogonal vectors around a falling graupel with a shape of $\lambda = 5$. The isosurface is a pressure of P = -1.5 Pa.

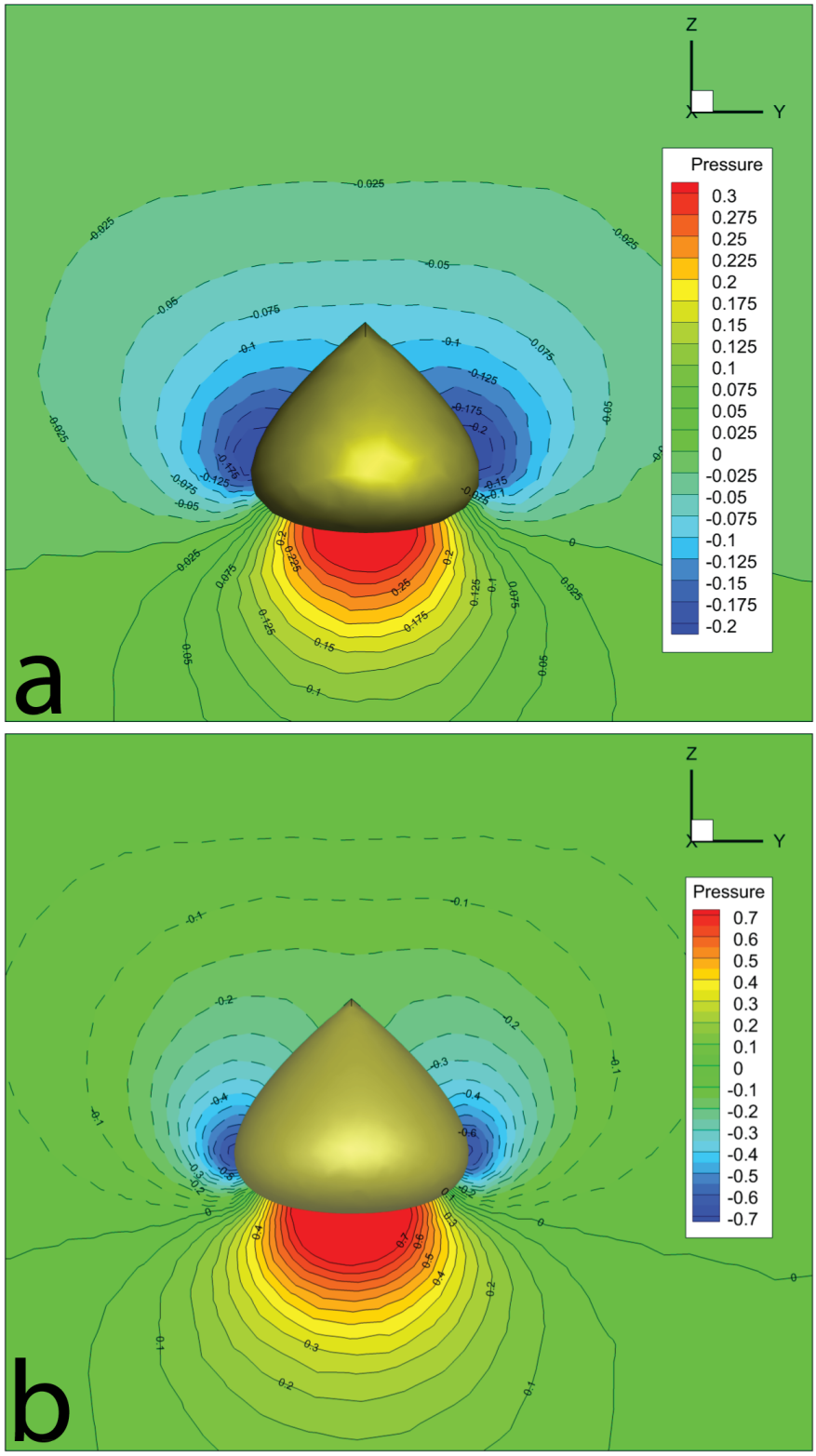


FIG. 25. Two randomly chosen frames of the computed pressure distributions around a falling graupel with a shape of $\lambda = 1$ and diameter of D = 0.5 mm (a) and D = 1mm (b). Negative values are dashed contours. The pressure is unit Pa.

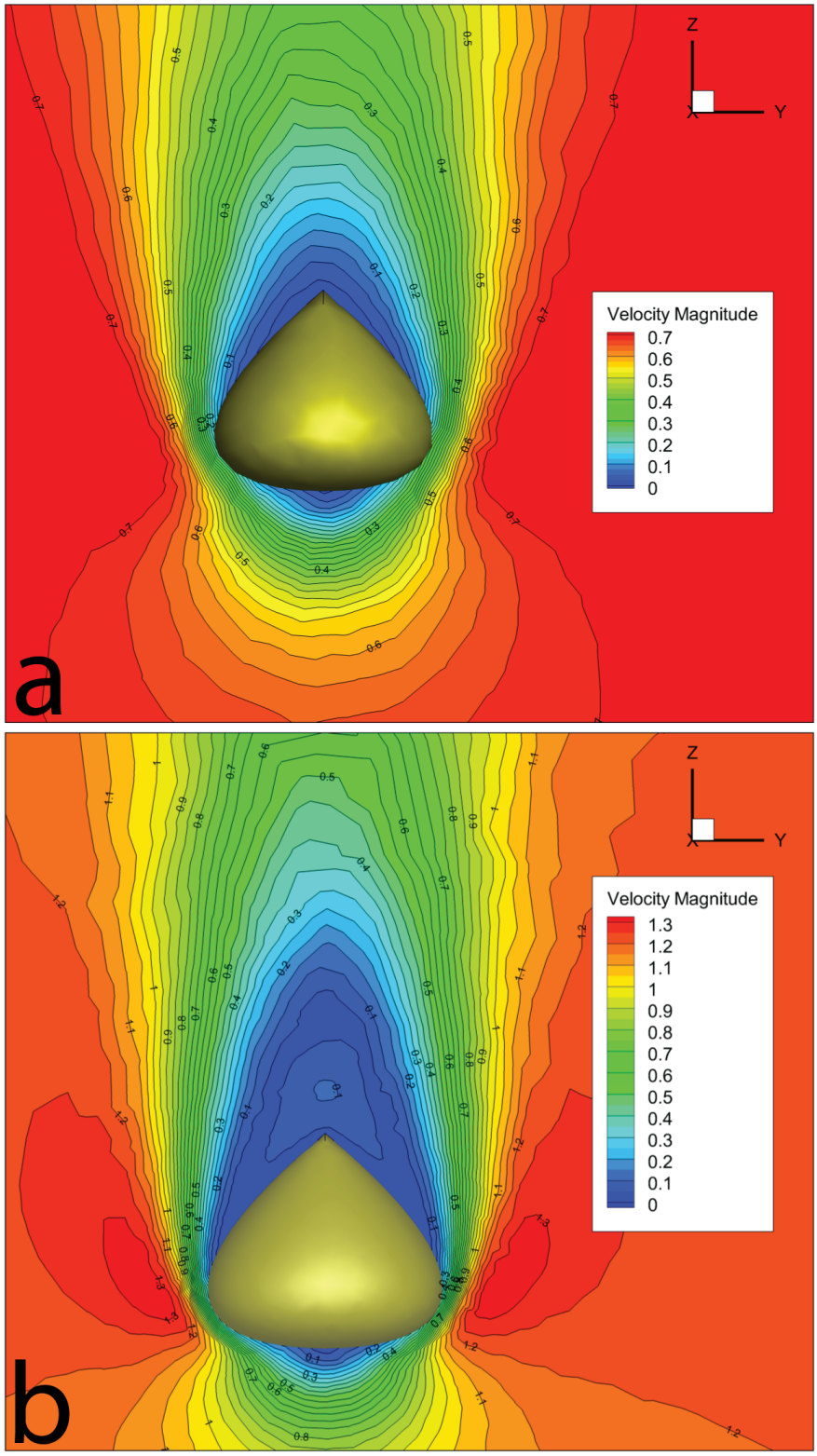


FIG. 26. Two randomly chosen frames of the computed velocity magnitude around a falling graupel with a shape of $\lambda = 1$ and diameter of D = 0.5 mm (a) and D = 1 mm (b). The velocity is unit m/s.

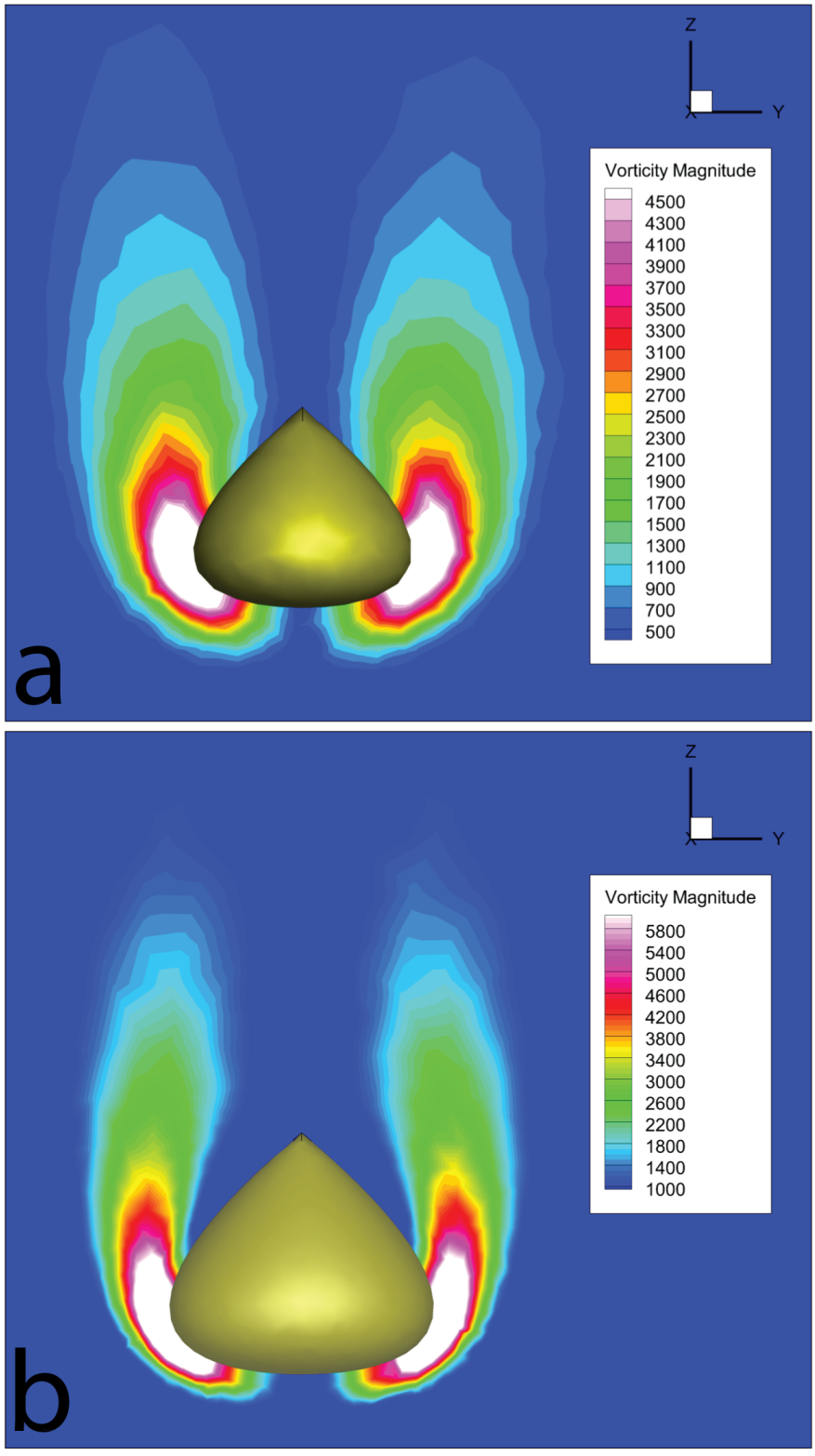


FIG. 27. Two randomly chosen frames of the computed vorticity magnitude around a falling graupel with a shape of $\lambda = 1$ and diameter of D = 0.5 mm (a) and D = 1 mm. The velocity is unit 1/s.

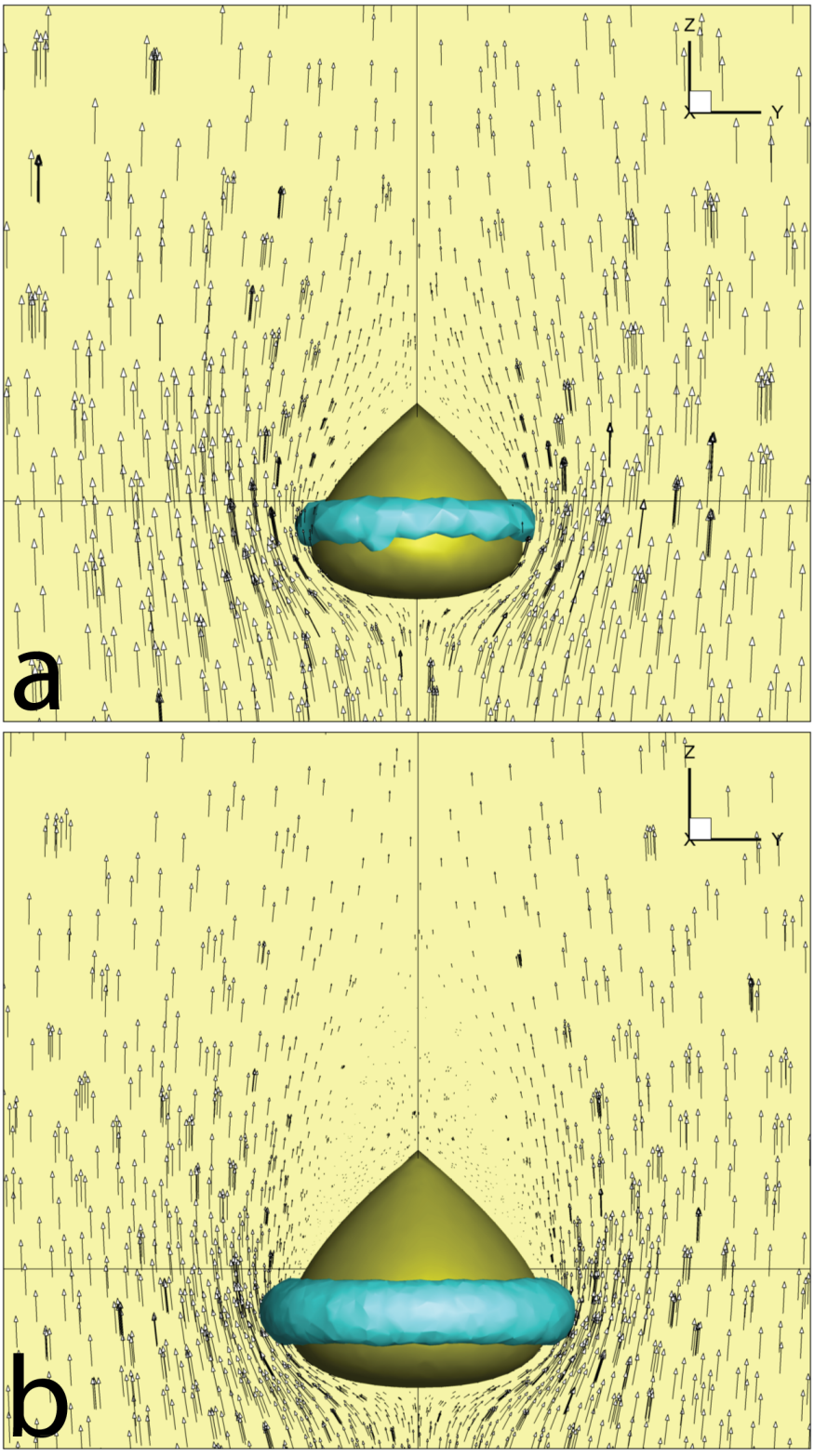


FIG. 28. Two randomly chosen frames of the computed velocity magnitude shown as orthogonal vectors around a falling graupel with a shape of $\lambda = 1$ and diameter of D = 0.5 mm (a) and D = 1 mm. The isosurface is a pressure of P = -1.5 Pa.

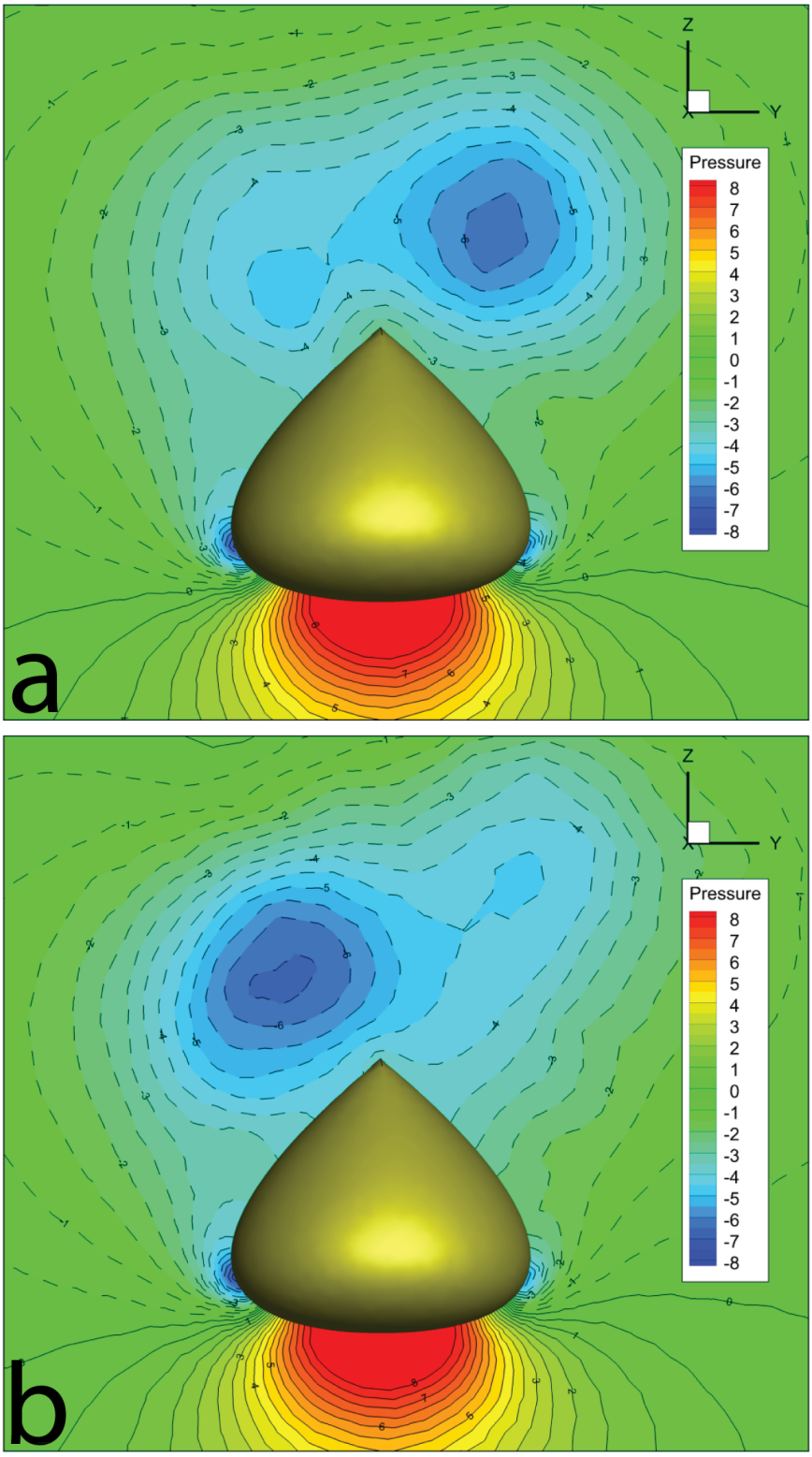


FIG. 29. Two randomly chosen frames of the computed pressure distributions around a falling graupel with a shape of $\lambda = 1$ and diameter of D = 5 mm. Negative values are dashed contours. The pressure is unit Pa.

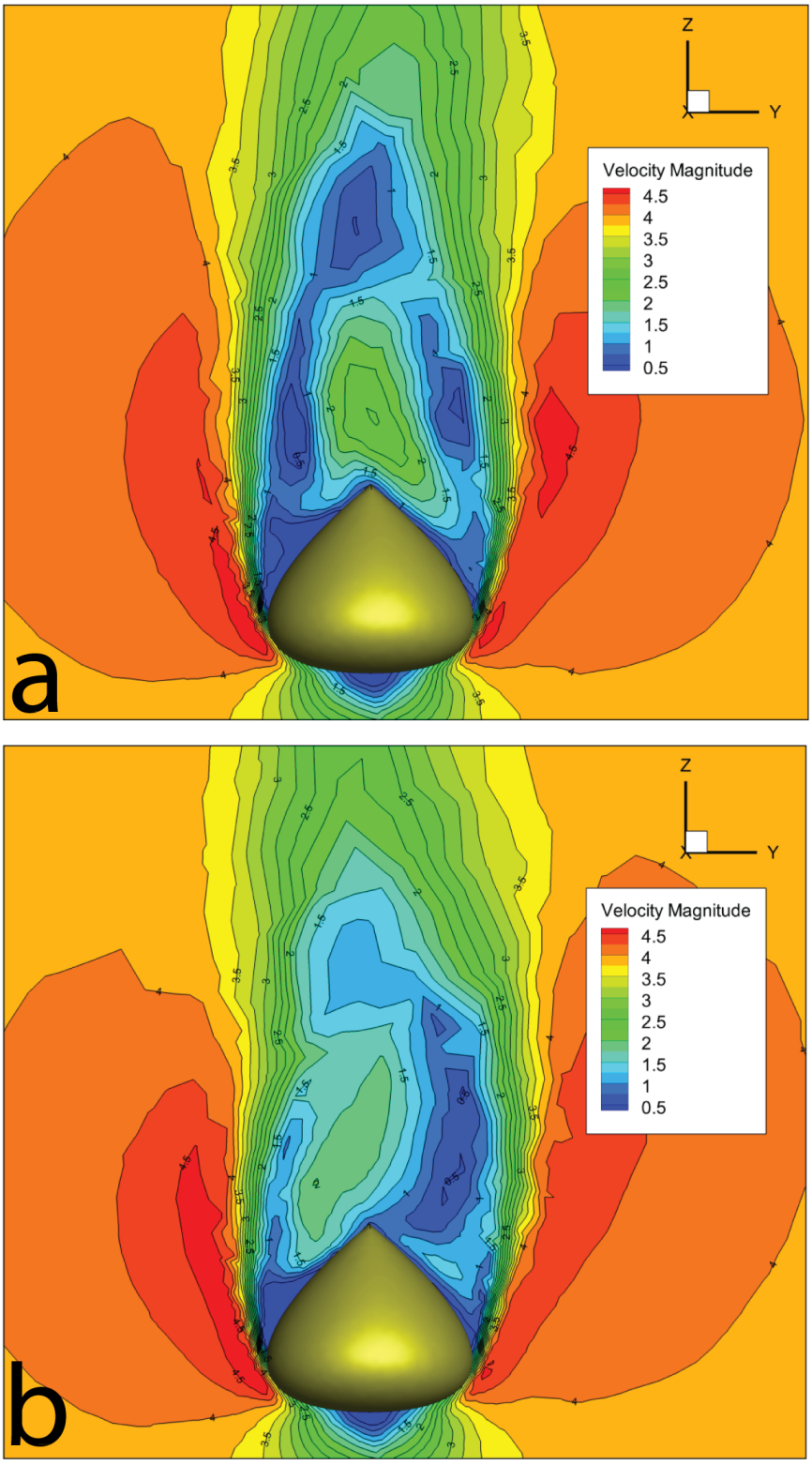


FIG. 30. Two randomly chosen frames of the computed velocity magnitude around a falling graupel with a shape of $\lambda = 1$ and diameter of D =5 mm. The velocity is unit m/s.

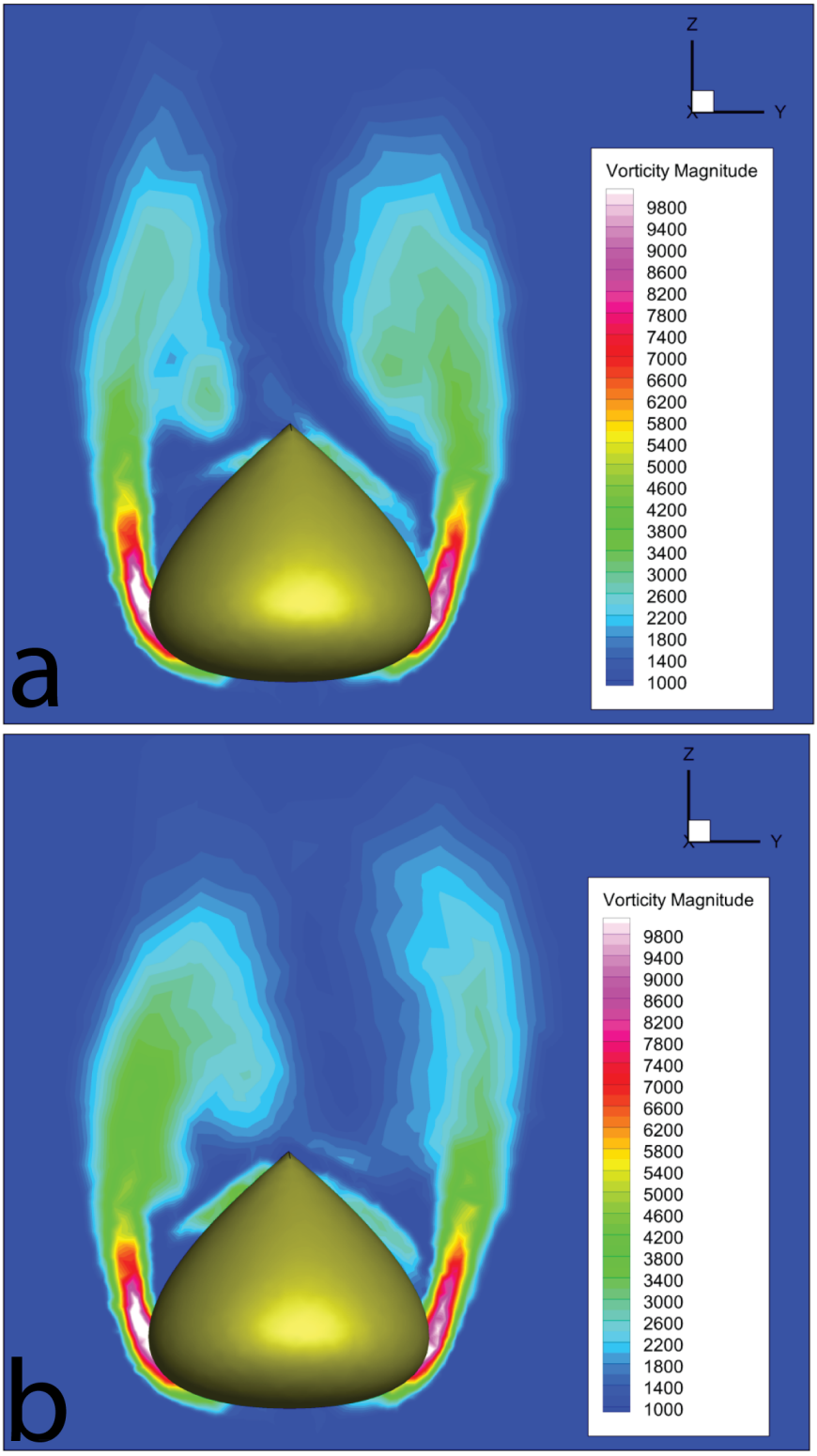


FIG. 31. Two randomly chosen frames of the computed vorticity magnitude around a falling graupel with a shape of $\lambda = 1$ and diameter of D = 5 mm. The velocity is unit 1/s.

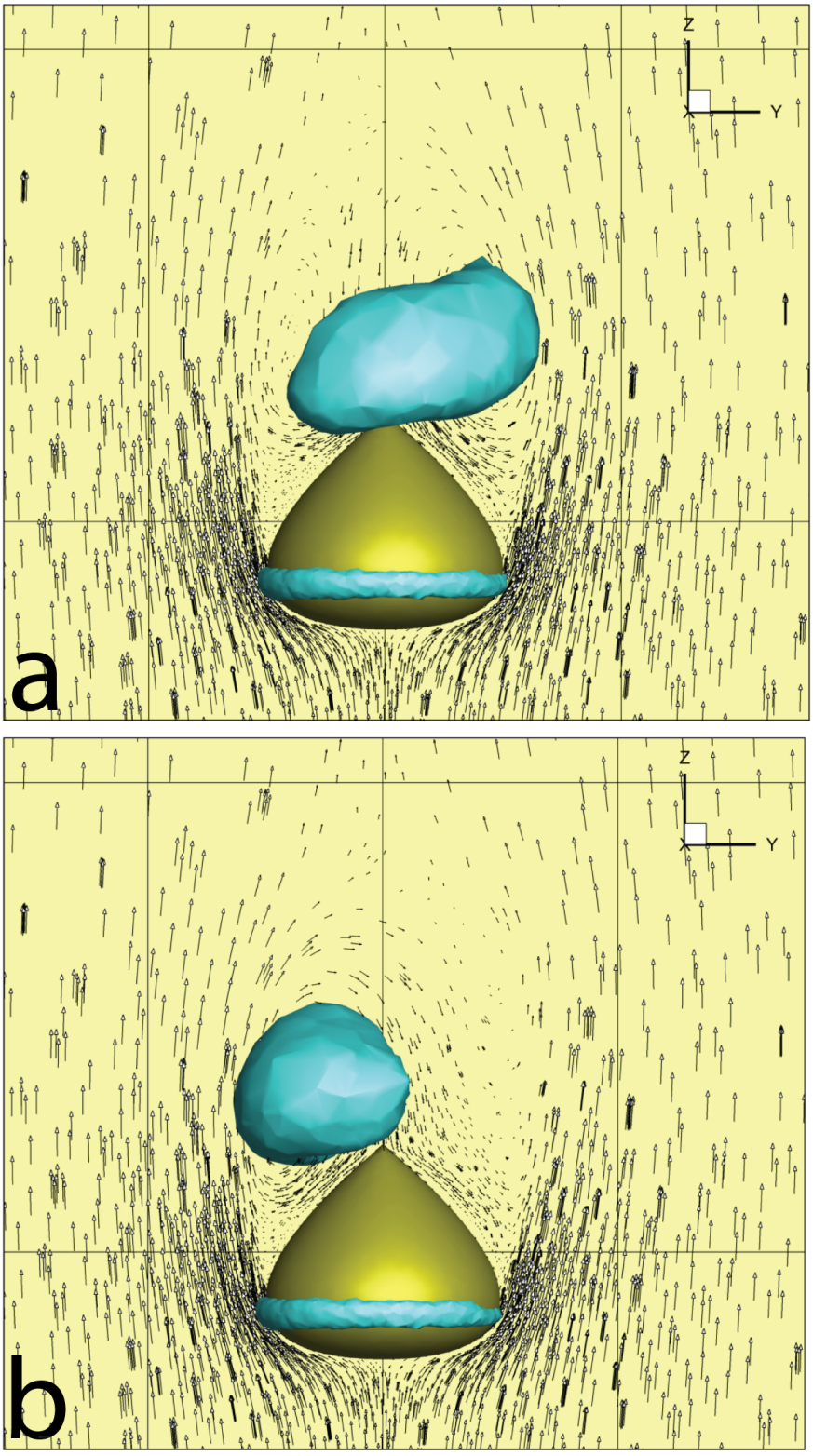


FIG. 32. Two randomly chosen frames of the computed velocity magnitude shown as orthogonal vectors around a falling graupel with a shape of $\lambda = 1$ and diameter of D = 5 mm. The isosurface is a pressure of P = -6 Pa.

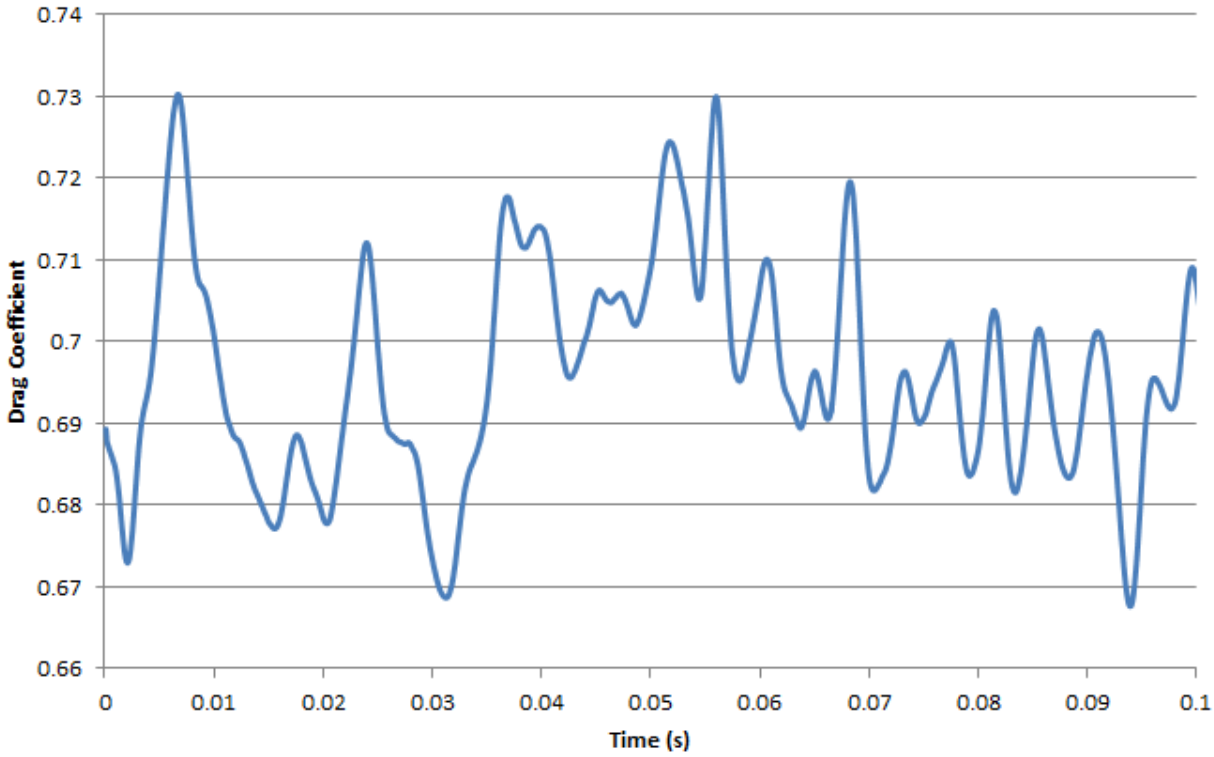


FIG. 33. Drag coefficient for falling graupel with a shape of $\lambda = 1$ and diameter of D = 5 mm.

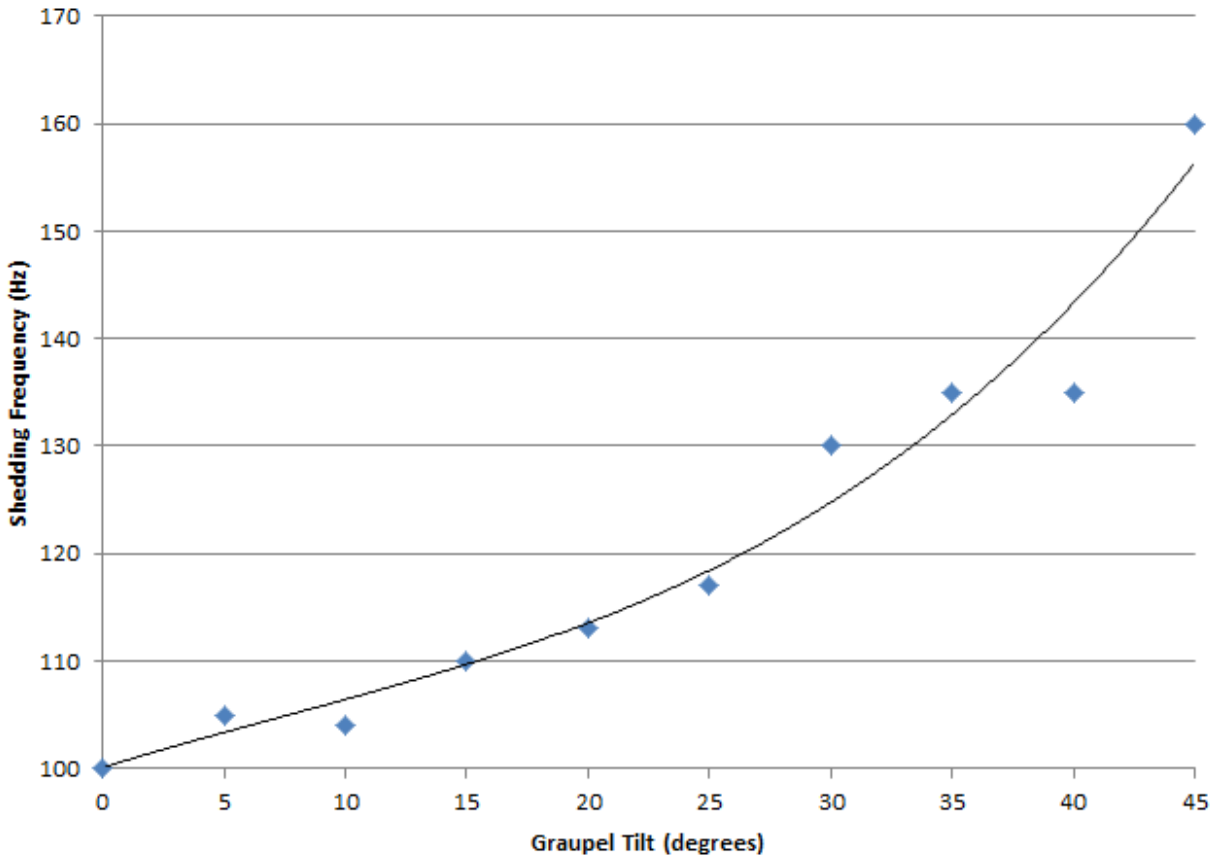


FIG. 34. Shedding frequency plot and fitted line for the inclined cases ($\theta = 0$ to $\theta = 45$) of falling graupel with shape $\lambda = 1$.

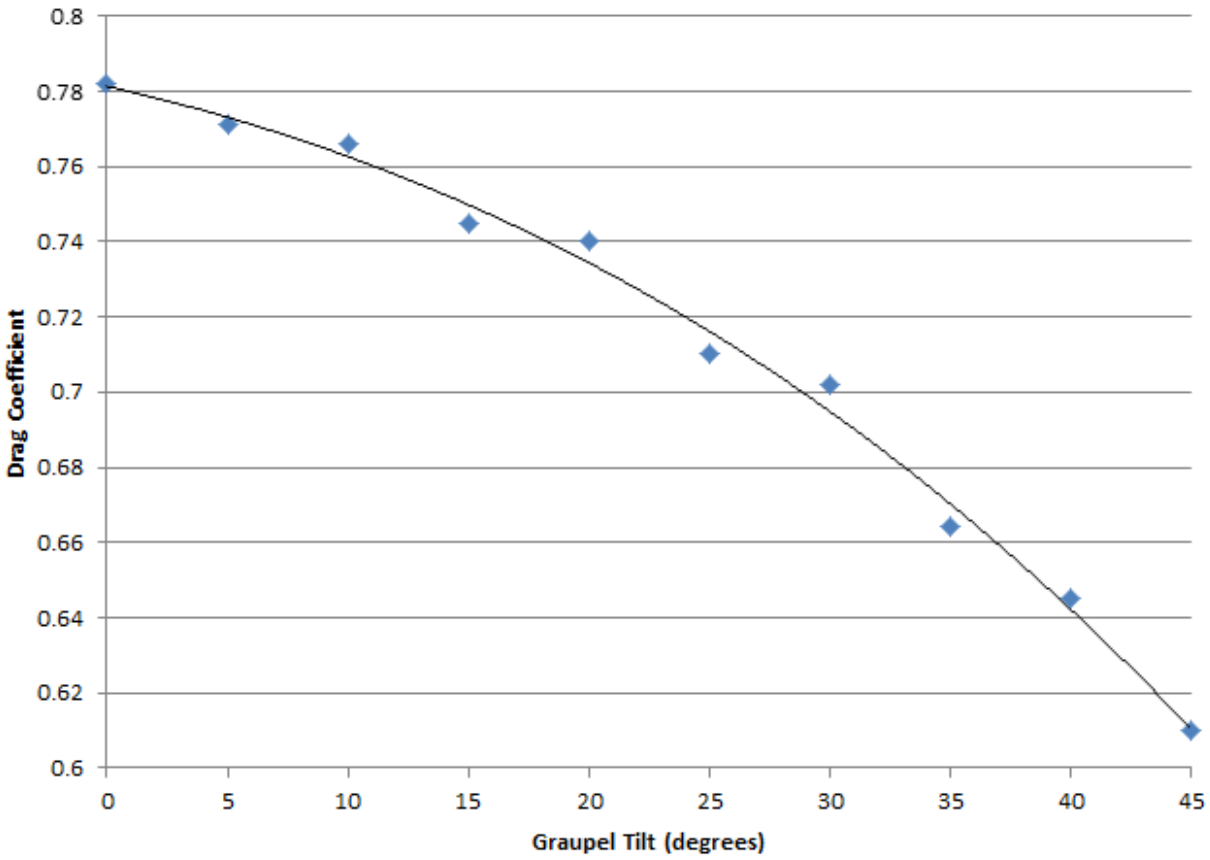


FIG. 35. Drag coefficient plot and fitted line for the inclined cases ($\theta = 0$ to $\theta = 45$) of falling graupel with shape $\lambda = 1$.

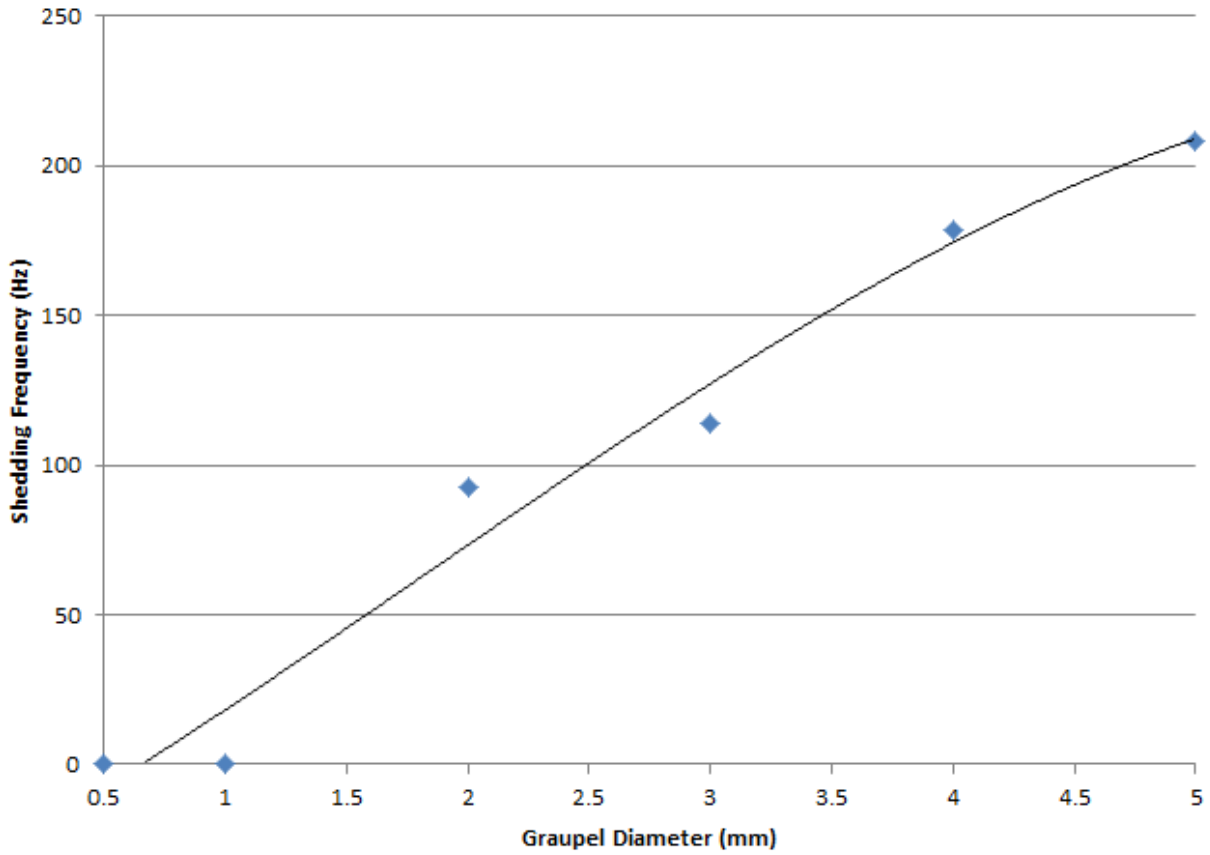


FIG. 36. Shedding frequency plot and fitted line for the different shape cases (D = 0.5 mm to D = 5 mm) of falling graupel with shape $\lambda = 1$.

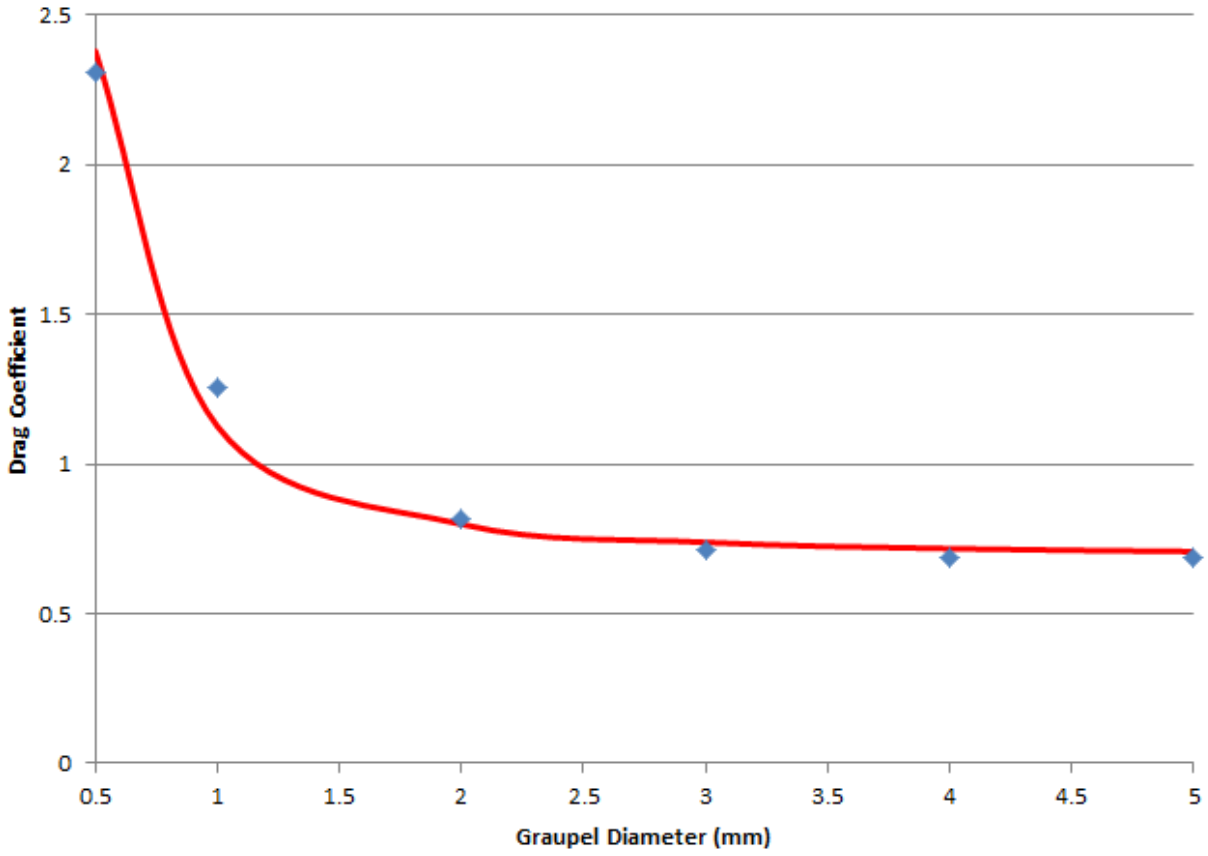


FIG. 37. Drag coefficient plot and fitted line for the different shape cases (D = 0.5 mm to D = 5 mm) of falling graupel with shape $\lambda = 1$.

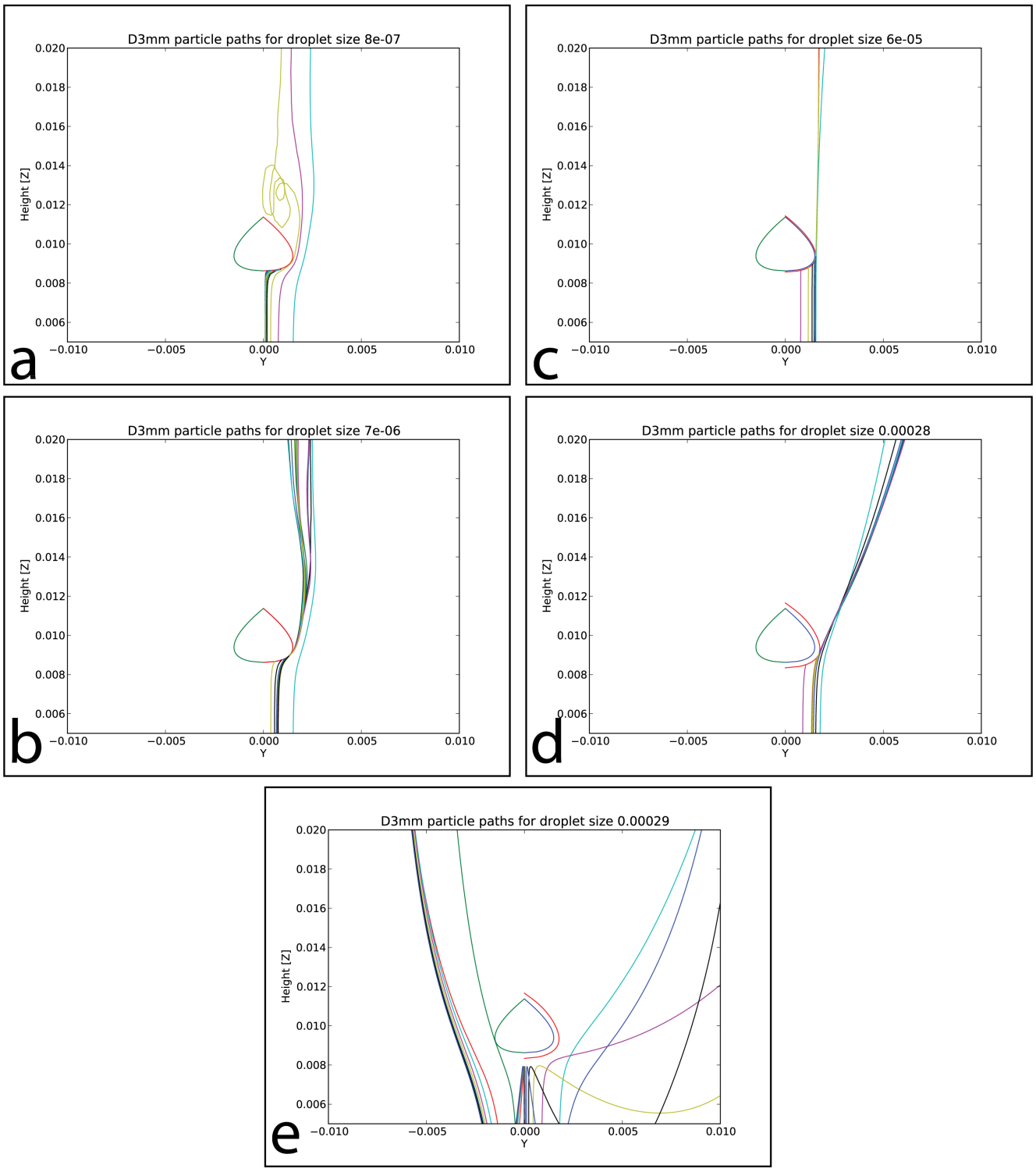


FIG. 38. Droplet path behaviors of falling graupel with shape $\lambda = 1$ and diameter of 3 mm. The red line on the outside of the graupel shows the minimum distance the droplet can approach the graupel before colliding. Droplet sizes of (a) 0.8 µm (b) 7 µm (c) 60 µm (d) 280 µm (e) 290 µm.

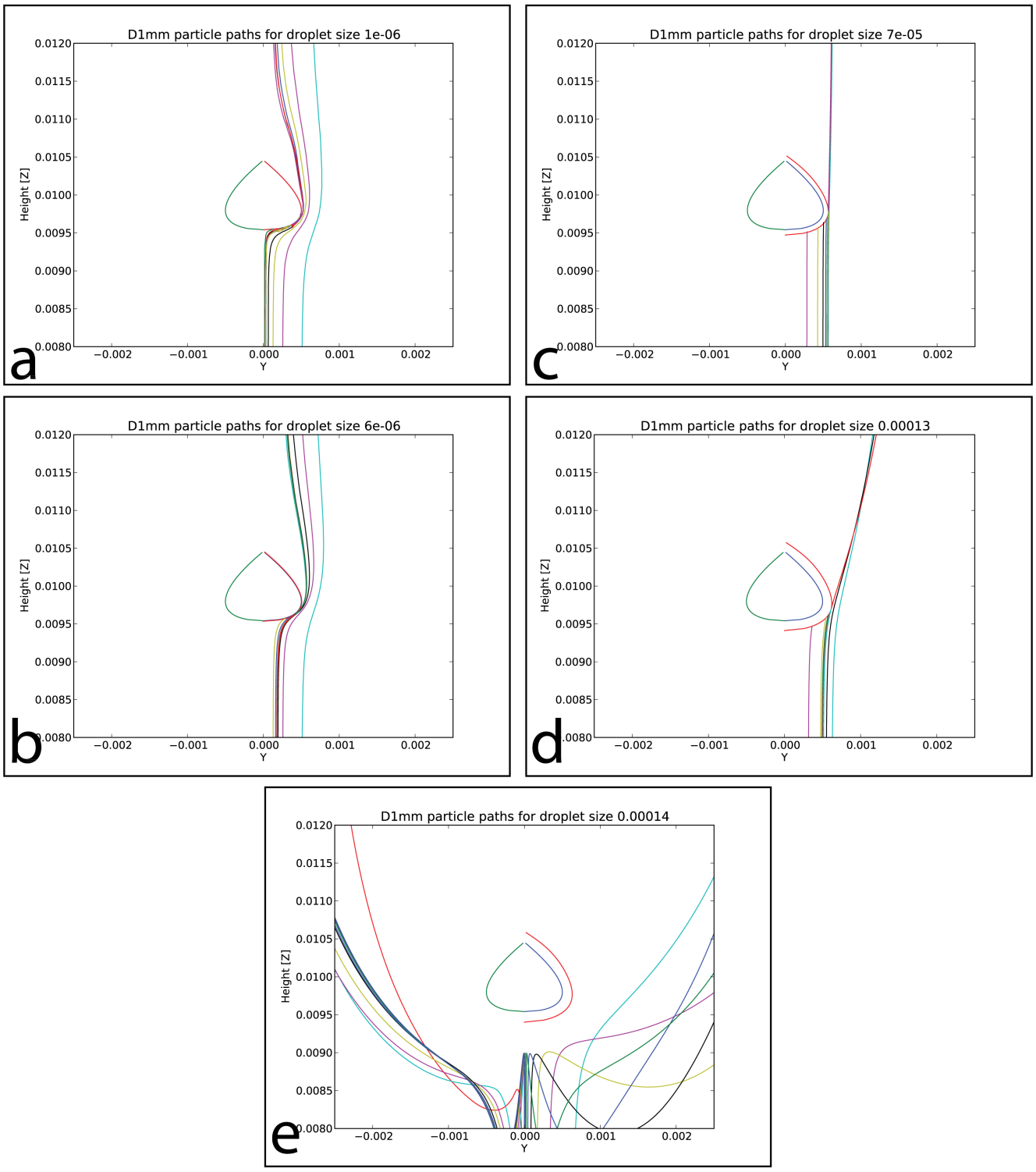


FIG. 39. Droplet path behaviors of falling graupel with shape $\lambda = 1$ and diameter of 1 mm. The red line on the outside of the graupel shows the minimum distance the droplet can approach the graupel before colliding. Droplet sizes of (a) 1 µm (b) 6 µm (c) 70 µm (d) 130 µm (e) 140 µm.

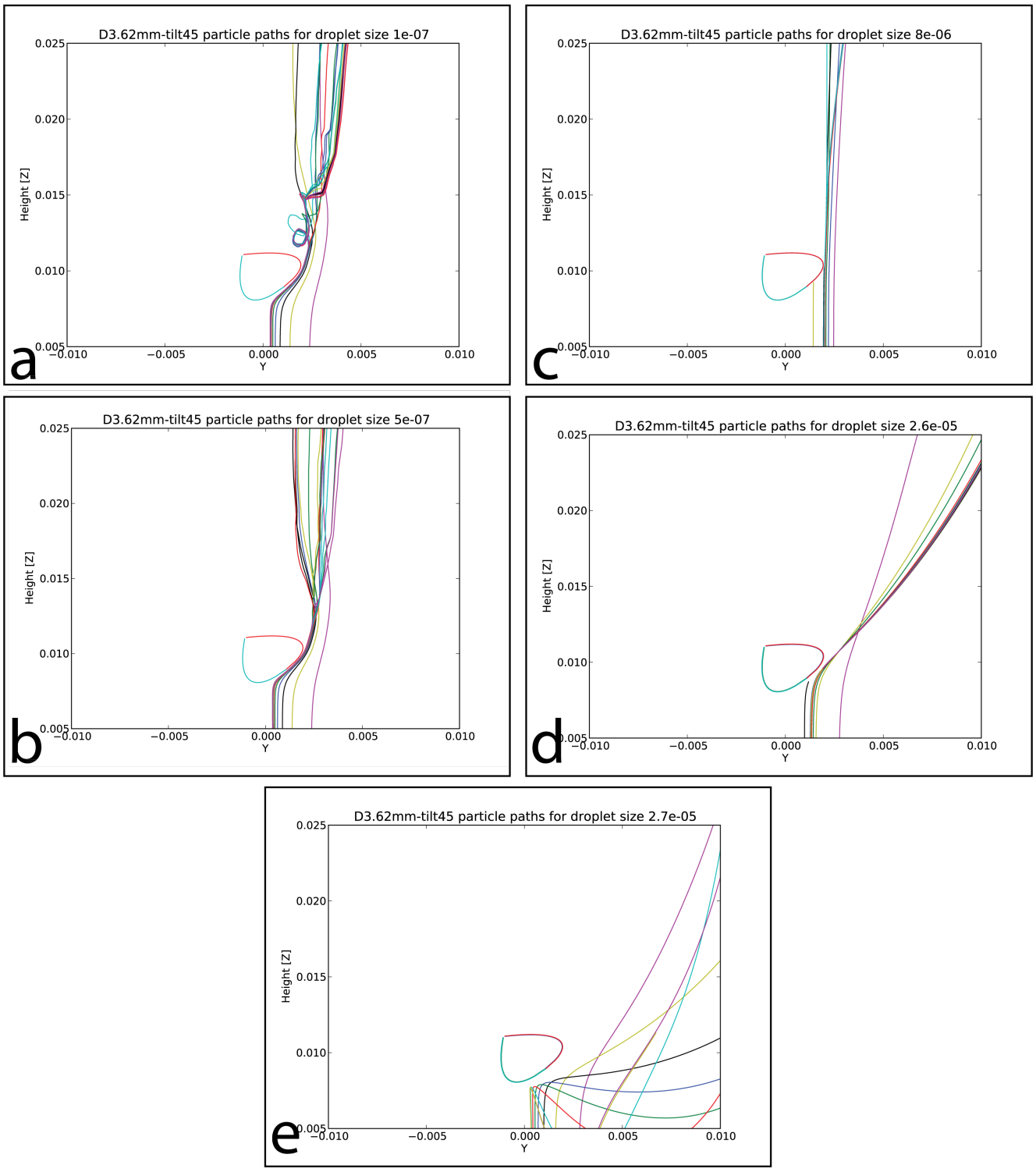


FIG. 40. Droplet path behaviors of falling graupel with shape $\lambda = 1$, diameter of 3.67 mm, and an inclination of $\theta = 45$. Droplets approach the graupel from the right. The red line on the outside of the graupel shows the minimum distance the droplet can approach the graupel before colliding. Droplet sizes of (a) 1 µm (b) 5 µm (c) 80 µm (d) 260 µm (e) 270 µm.

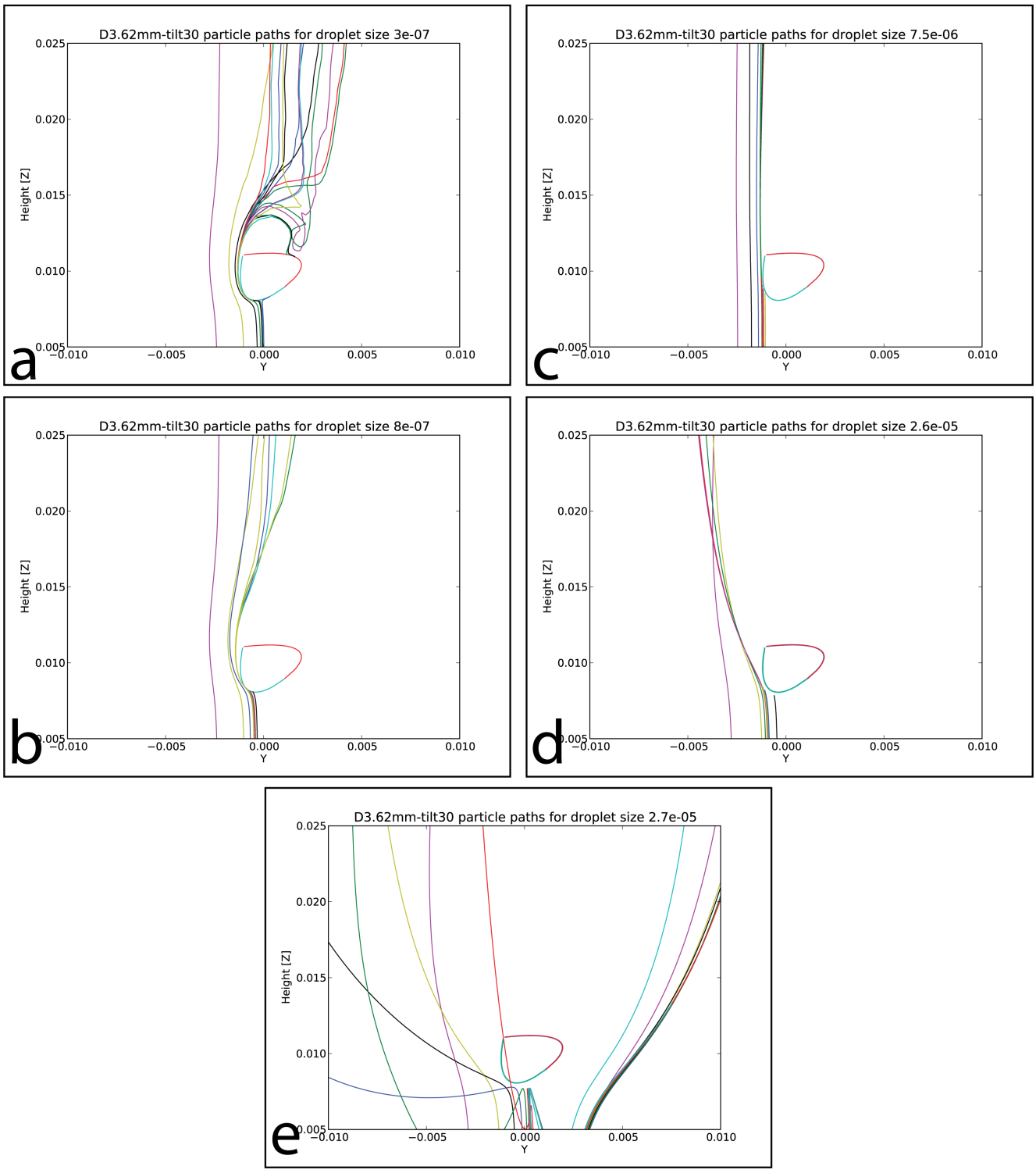


FIG. 41. Droplet path behaviors of falling graupel with shape $\lambda = 1$, diameter of 3.67 mm, and an inclination of $\theta = 45$. Droplets approach the graupel from the left. The red line on the outside of the graupel shows the minimum distance the droplet can approach the graupel before colliding. Droplet sizes of (a) 3 µm (b) 8 µm (c) 75 µm (d) 260 µm (e) 270 µm.

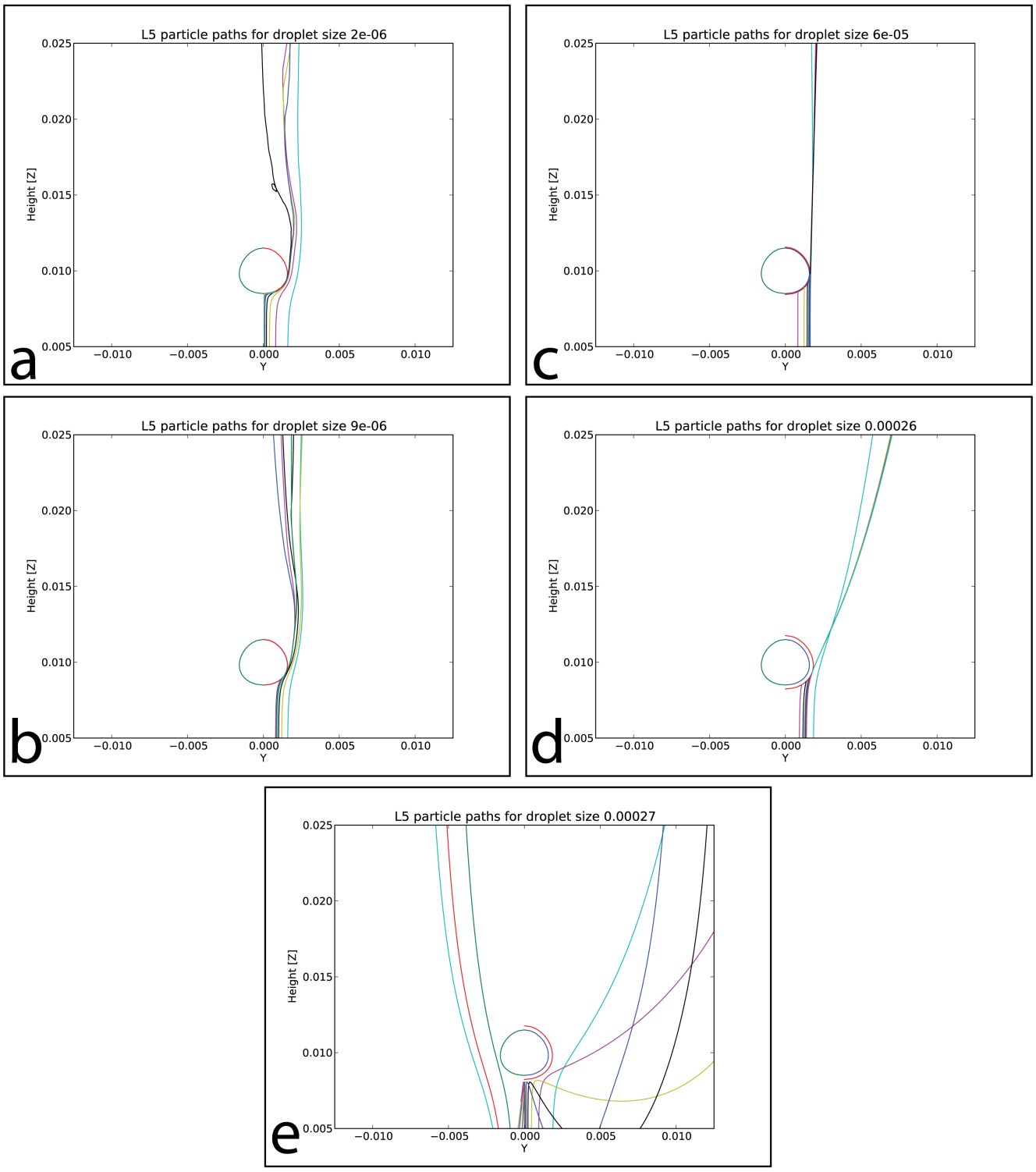


FIG. 42. Droplet path behaviors of falling graupel with shape $\lambda = 5$, diameter of 3.17 mm, and an inclination of $\theta = 45$. The red line on the outside of the graupel shows the minimum distance the droplet can approach the graupel before colliding. Droplet sizes of (a) 2 µm (b) 9 µm (c) 60 µm (d) 260 µm (e) 270 µm.

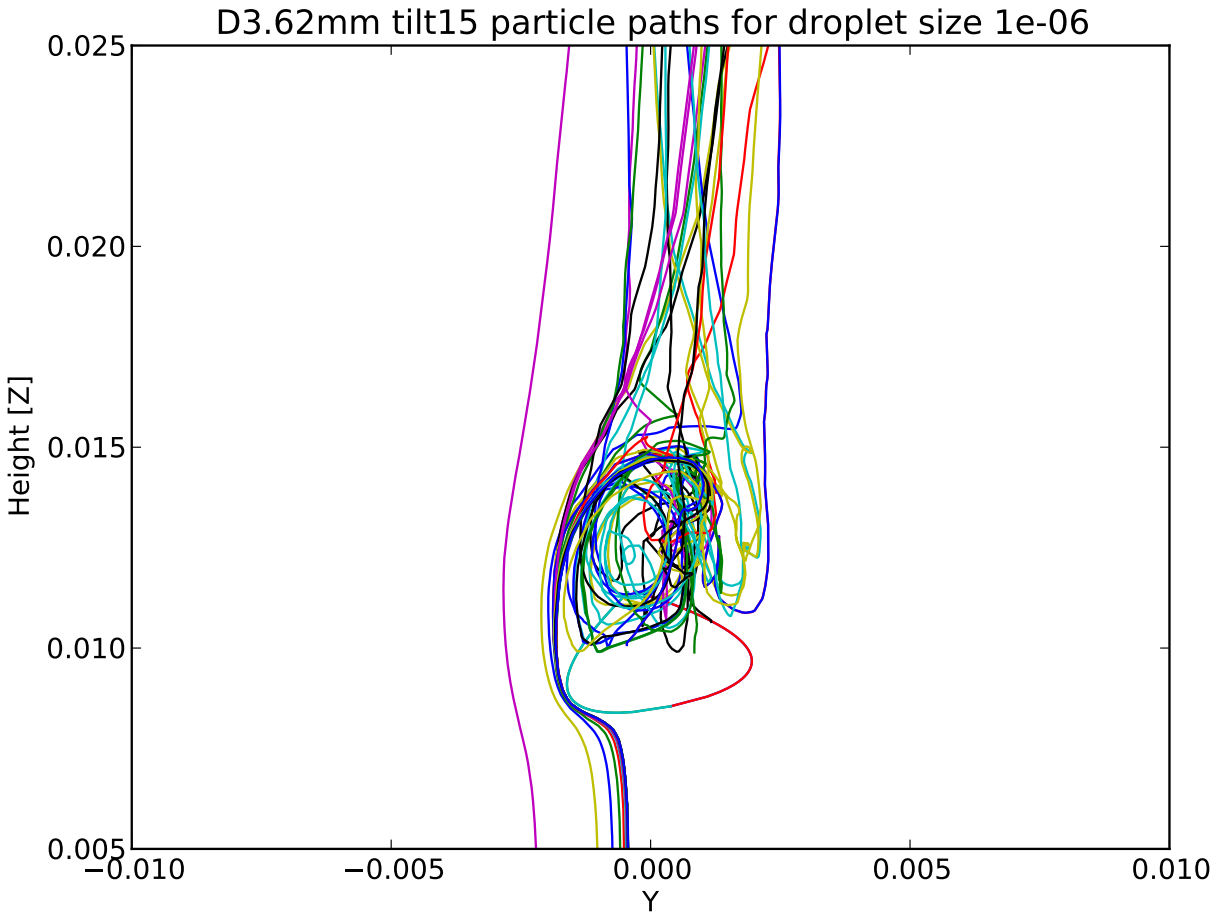


FIG. 43. Droplet path behaviors of falling graupel with shape $\lambda = 1$, diameter of 3.67 mm, and an inclination of $\theta = 15$. This shows the grazing collision trajectory of cloud droplets coming from the left of the graupel with droplet radii of 1 µm. Notice that the cloud droplets typically get captured by the graupel's eddies and are wake captured.

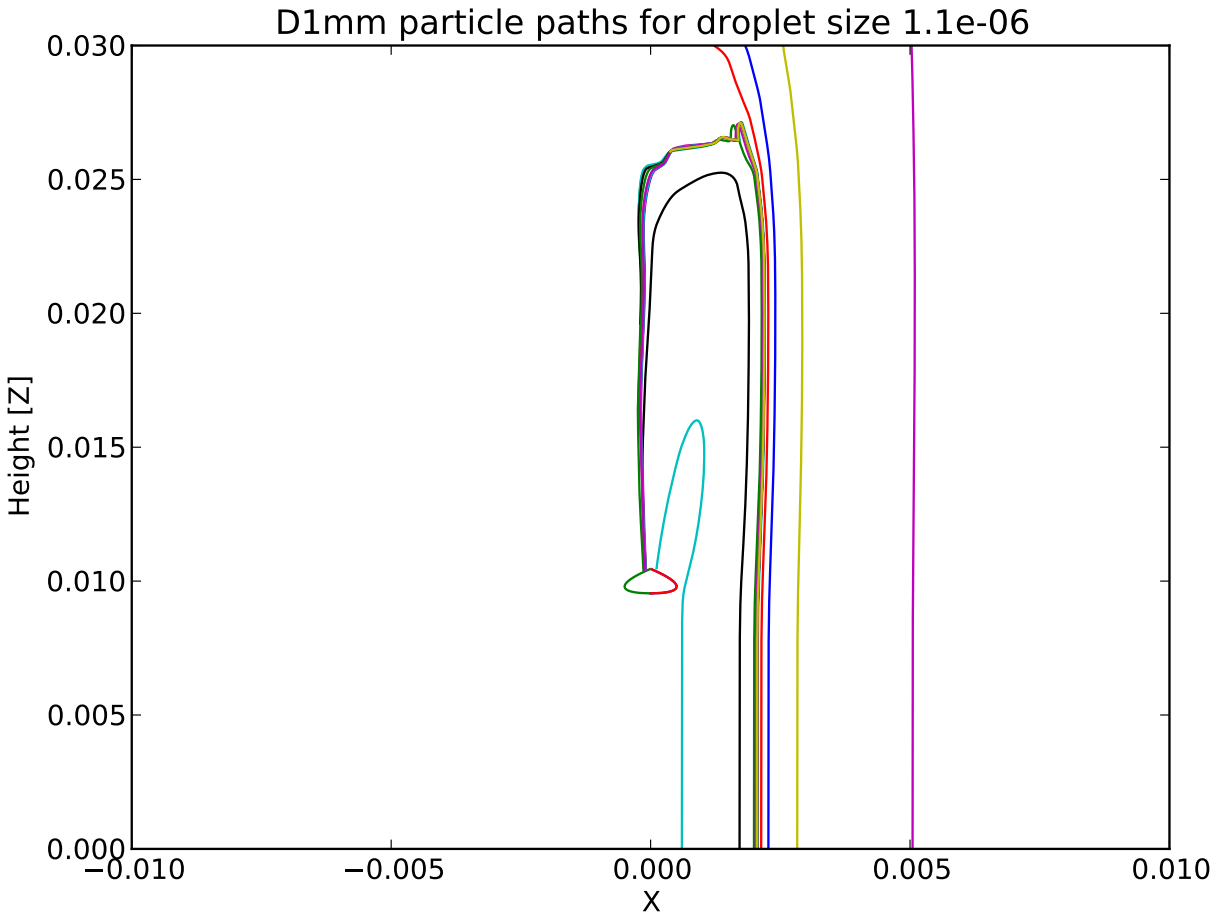


FIG. 44. Droplet path behaviors of falling graupel with shape $\lambda = 1$ and diameter of 1 mm. This shows the grazing collision trajectory of cloud droplets coming from the far right of the graupel with droplet radii of 1.1 µm. The droplets are traveling at .4 m/s above their terminal velocity and are wake captures from a long range.

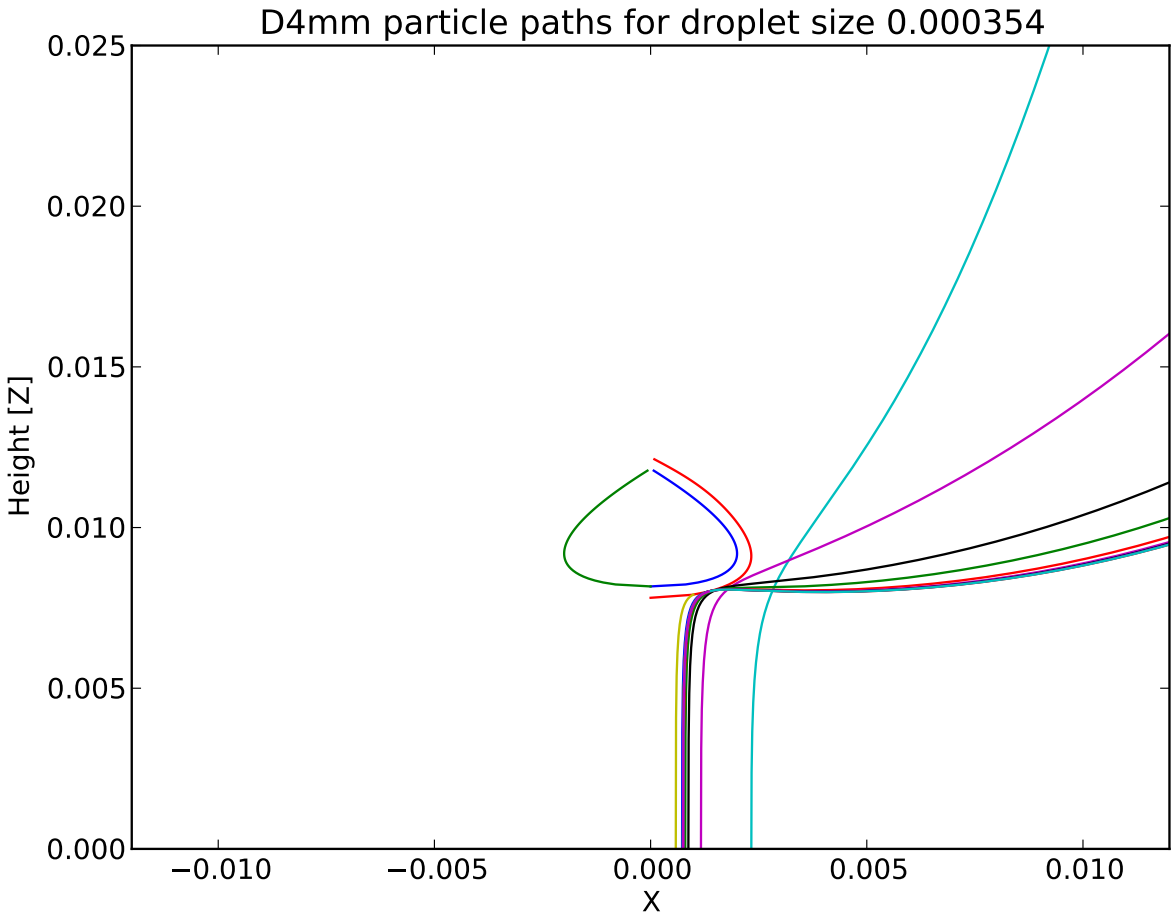


FIG. 45. Droplet path behaviors of falling graupel with shape $\lambda = 1$ and diameter of 4 mm. This shows the grazing collision trajectory of cloud droplets coming from the right of the graupel with droplet radii of 354 µm. The droplets are traveling near the terminal velocity of the graupel and are scattered as they approach the graupel's base.

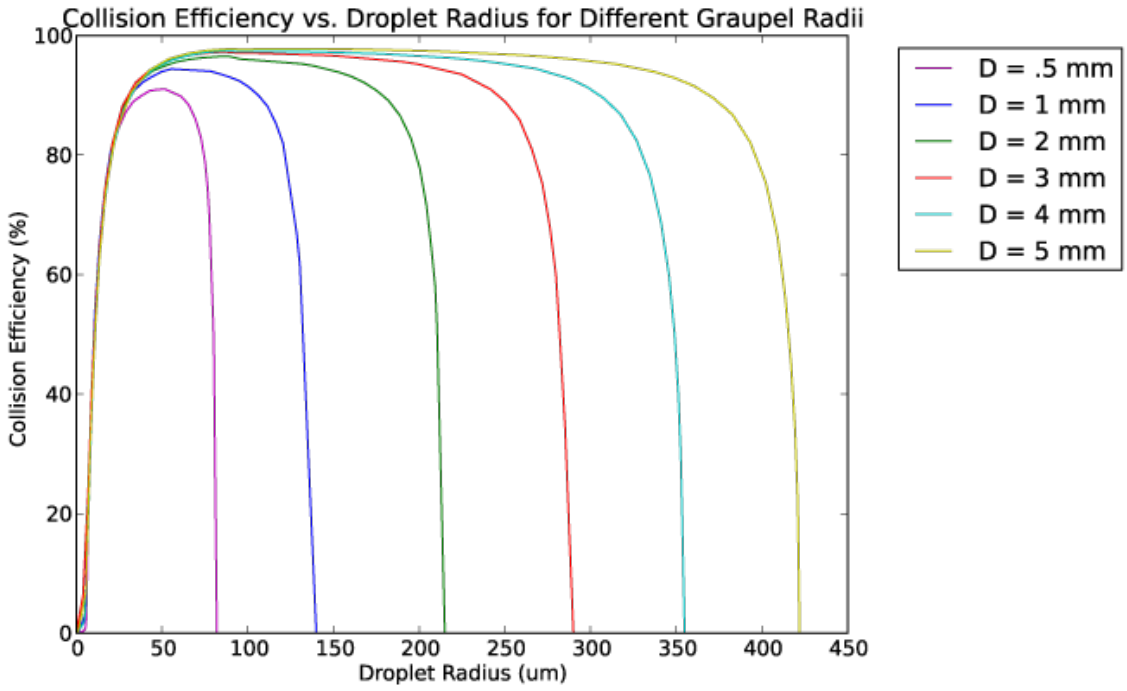


FIG. 46. Collision Efficiency with respect to drop size for graupel diameter D = 0.5 mm to D = 5 mm and shape $\lambda = 1$.

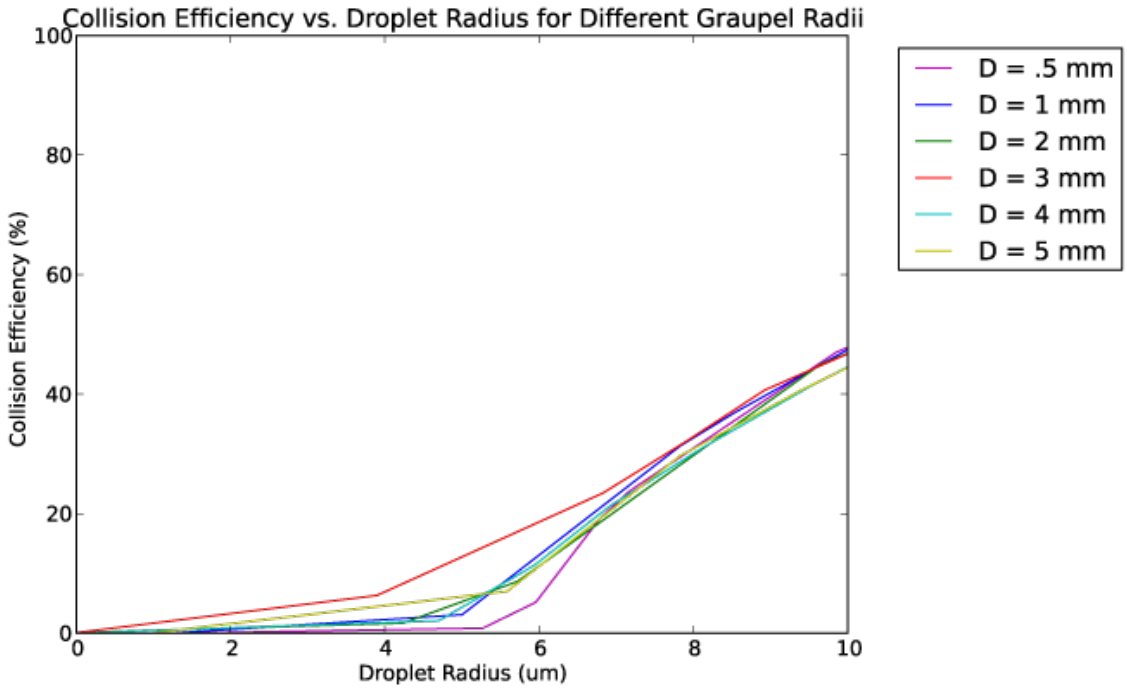


FIG. 47. Collision Efficiency with respect to Interception Efficiency (size ratio) for graupel diameter D = 0.5 mm to D = 5 mm and shape $\lambda = 1$. This looks at the beginning of the riming process where the cloud droplets have a radius from 0.1 µm to 10 µm

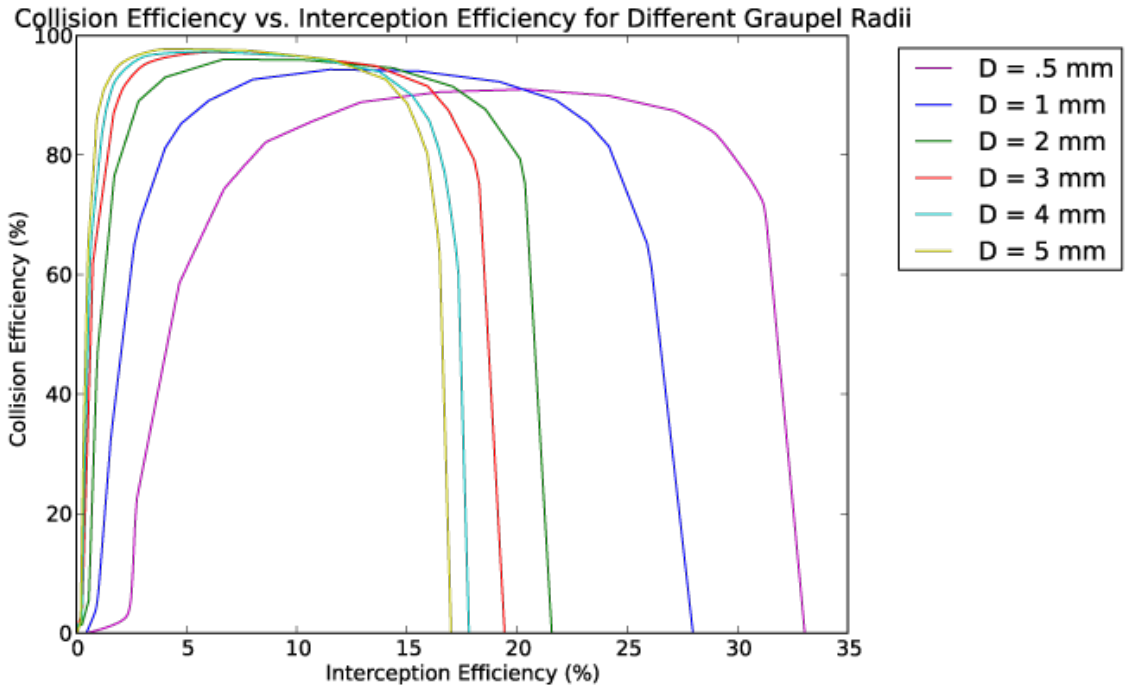


FIG. 48. Collision Efficiency with respect to Interception Efficiency (size ratio) for graupel diameter D = 0.5 mm to D = 5 mm and shape $\lambda = 1$.

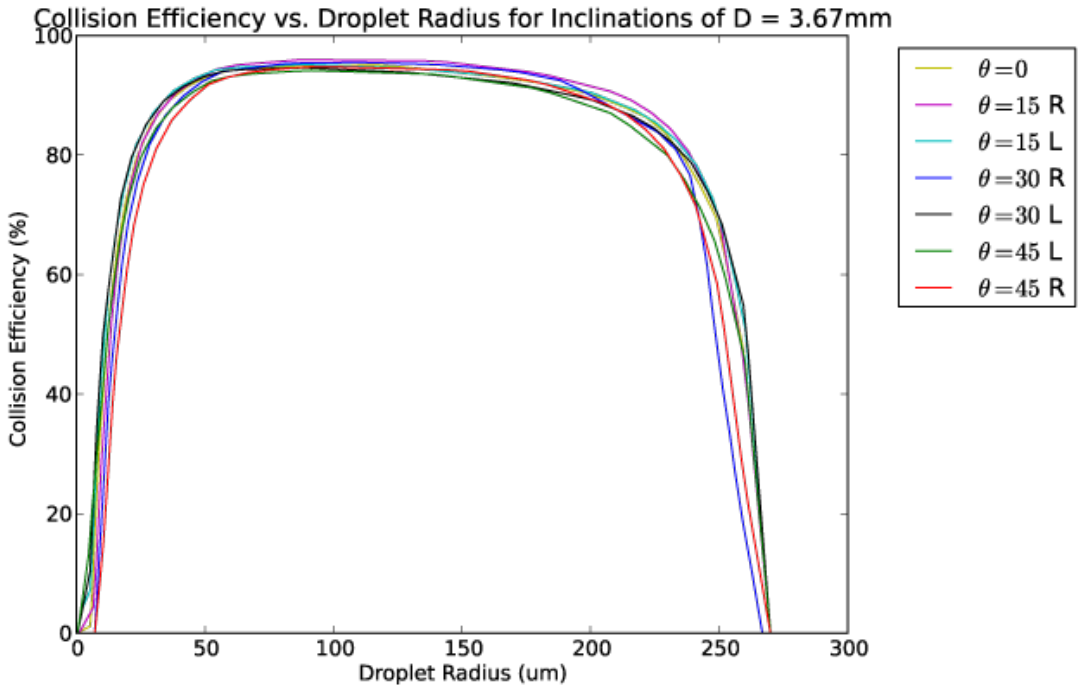


FIG. 49. Collision Efficiency with respect to drop size for change in inclination $\theta = 0$ to $\theta = 45$ with D = 3.67 mm and shape $\lambda = 1$. In the legend, L and R refer to droplets coming from the left or coming from the right, respectively.

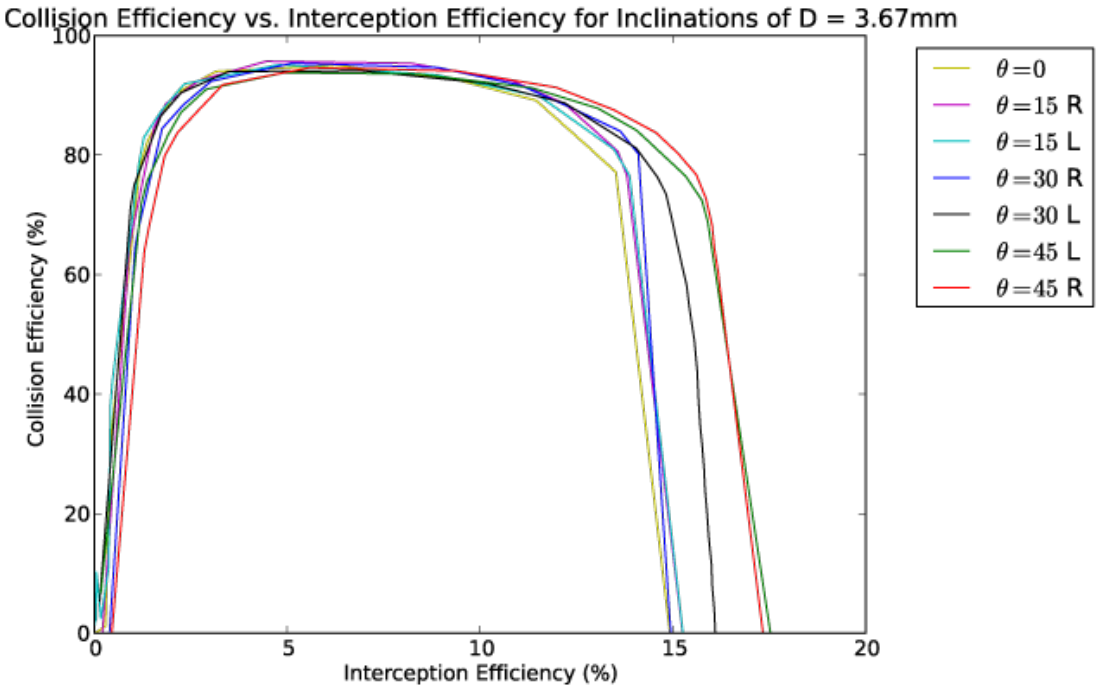


FIG. 50. Collision Efficiency with respect to Interception Efficiency (size ratio) for change in inclination $\theta = 0$ to $\theta = 45$ with D = 3.67 mm and shape $\lambda = 1$. In the legend, L and R refer to droplets coming from the left or coming from the right, respectively.

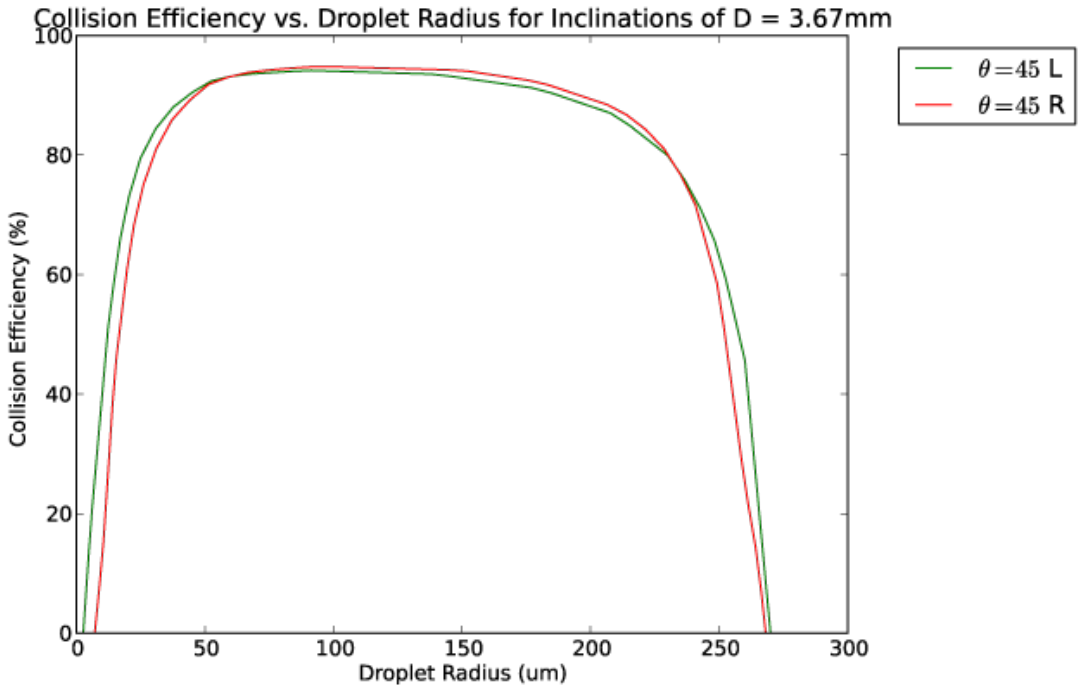


FIG. 51. Collision Efficiency with respect to drop size for inclination $\theta = 45$ with D = 3.67 mm and shape $\lambda = 1$. In the legend, L and R refer to droplets coming from the left or coming from the right, respectively.

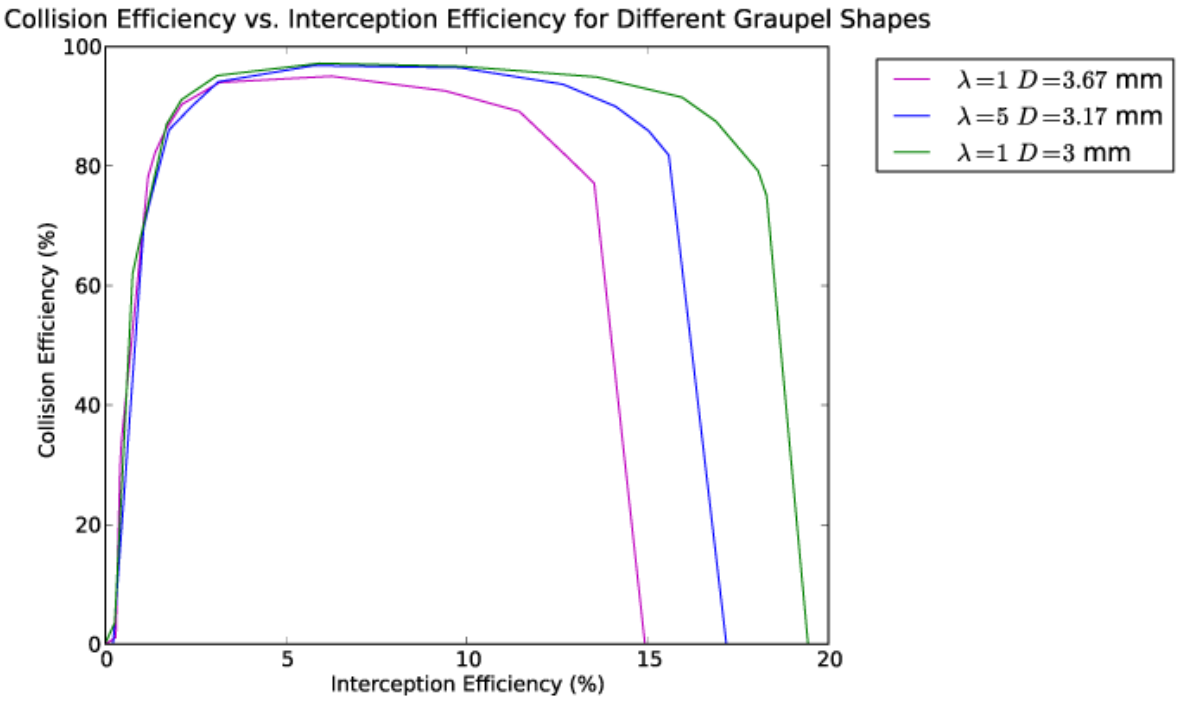


FIG. 52. Collision Efficiency with respect to Interception Efficiency (size ratio) for various $\lambda$ and diameter of the graupel.